ROUGHNESS-INDUCED INSTABILITY

IN A LAMINAR BOUNDARY LAYER AT MACH 6

10/26/2009

Includes minor correction to deposited copy

(Appendix D, run conditions, stagnation temperature is deg C, not K)

A Thesis

Submitted to the Faculty

of

Purdue University

by

Bradley M. Wheaton

In Partial Fulfillment of the

Requirements for the Degree

of

Master of Science in Aeronautics and Astronautics

December 2009

Purdue University

West Lafayette, Indiana

To my parents, whose hard work and many sacrifices
guided me to a world with endless opportunities

ACKNOWLEDGMENTS

This research was funded under NASA Cooperative Agreement 102361.

I would like to thank Prof. Steven P. Schneider for giving me the opportunity to work with the Boeing/AFOSR Mach-6 Quiet Tunnel and providing guidance and suggestions throughout this project. I would also like to thank the other members of my committee: Stephen Wilkinson from NASA Langley and Prof. Steven Collicott.

I am grateful to Madeline Chadwell, Jerry Hahn, Robin Snodgrass, Jim Younts, and Bill Buck of the Aerospace Sciences Laboratory machine shop for their help and craftsmanship. I would also like to thank John Philips, the AAE department electrician, for his assistance.

The members of Prof. Schneider's research group provided advice and suggestions: Erick Swanson, Matt Borg, Tom Juliano, Mikey Hannon, Rodrigo Segura, Katya Casper, Amanda Chou, Dennis Berridge, Peter Gilbert, Laura Steen, and Chris Ward. I would like to thank my coworkers along with Matt Conway, Adam Lavely, Ted Londner, Justin Rubal, Prashant Tatineni, Ross Winegar, and my other Purdue friends for providing valuable stress relief and fond memories.

Finally, I am indebted to my friends and family who have supported and encouraged me during my graduate work.

TABLE OF CONTENTS

Page

LIST OF TABLES

LIST OF FIGURES

SYMBOLS

A	disturbance amplitude
A_0	initial disturbance amplitude
D	roughness diameter, 0.235 in.
f	frequency, kHz
h	heat transfer coefficient, lbm/ft^2-s
I	intensity
k	roughness height
M	freestream Mach number
N	integrated amplification factor
p_0	tunnel freestream stagnation pressure
R	resistance, Ω
R_{gas}	specific gas constant, 287 J/kg-K for air
Re	Reynolds number
St	Strouhal number
t	time, or tunnel run time, s
T	temperature, K
U	streamwise velocity, m/s
V	voltage
x	streamwise coordinate
y	vertical probe height above wall
z	tunnel axial coordinate ($z = 0$ at throat)

Greek

α	wave number, or temperature coefficient of resistance, 1/°C
$-\alpha_i$	spatial amplification rate, 1/m
β	wave frequency
Δf	spectrum frequency resolution
δ	boundary-layer height
γ	ratio of specific heats
μ	dynamic viscosity, kg/m-s
Ω	ohms
ρ	density
ρu	mass flux, kg/s-m^2

Subscripts

∞	freestream conditions
0	stagnation conditions in freestream
$19-23$kHz	frequency band of 19–23 kHz
e	boundary-layer edge conditions
i	initial conditions
k	roughness height conditions
ref	reference conditions
T	transition location
vac	vacuum

ABBREVIATIONS

AC	Alternating Current
ASL	Aerospace Sciences Laboratory
BAM6QT	Boeing/AFOSR Mach-6 Quiet Tunnel
CCD	Charge-Coupled Device
CTA	Constant-Temperature Anemometer
DC	Direct Current
DCF	DC Fluctuation
LST	Linear Stability Theory
PLIF	Planar Laser-Induced Fluorescence
PSE	Parabolized Stability Equations
RMS	Root Mean Square
TPS	Thermal Protection System
TSP	Temperature-Sensitive Paint

ABSTRACT

Wheaton, Bradley M. M.S.A.A., Purdue University, December 2009. Roughness-Induced Instability in a Laminar Boundary Layer at Mach 6. Major Professor: Steven P. Schneider.

Roughness can cause a boundary layer to become turbulent, increasing aeroheating from the laminar rate. Empirical correlations are currently used to predict the onset of roughness-induced transition but do not take into account the flow physics that cause it. More accurate physics-based prediction methods must be developed, based on the growth of instabilities within the wake of the roughness. An isolated roughness element was used to introduce instabilities into a laminar nozzle-wall boundary layer in the Boeing/AFOSR Mach-6 Quiet Tunnel. Qualitative temperature-sensitive paint measurements show several hot streaks within the wake of the roughness. Pitot and hot-wire probes were used to measure an instability in the wake of the roughness. These are believed to be the first such measurements at hypersonic speeds. The instability was observed to grow downstream of the roughness and was strongest off the wake centerline, at a height near the roughness height. Mean-flow pitot pressures in the wake of the roughness were recorded for comparison to future computations of the wake. Further characterization of this instability can assist development and validation of a physics-based transition prediction method for roughness-induced transition.

1. INTRODUCTION

1.1 Hypersonic Boundary-Layer Transition

Boundary-layer transition is an important factor in the design of hypersonic vehicles but is difficult to predict. A boundary layer is the viscous region near the surface of a vehicle through which the fluid velocity decelerates from its freestream value due to friction [1]. For continuum flow, the velocity of the fluid must match that of the surface of a vehicle. A boundary layer generally exists in one of two states: laminar (or smooth) or turbulent, separated by a transition region. When a boundary layer is laminar, the streamlines within the boundary layer are smooth, parallel, and roughly aligned with the surface of the body. A turbulent boundary layer is characterized by irregular mixing of fluid particles [2, 3].

The location of boundary-layer transition affects aeroheating as well as vehicle drag and moments [4]. At high Mach numbers, the surface of a vehicle experiences extreme temperatures as the high kinetic energy of the flow is transformed into thermal energy during deceleration [5]. The surface temperatures are generally much higher when the boundary layer is turbulent. A turbulent boundary layer has higher mixing at the wall, increasing heat transfer to the surface. In addition, a turbulent boundary layer increases the skin friction coefficient. Asymmetric transition on a slender vehicle causes friction-induced moments which can adversely affect flight stability on a reentry vehicle [4]. Accurate prediction of boundary-layer transition is desired to predict heating, friction, and stability of a hypersonic flight vehicle.

Boundary-layer transition is caused by the growth of disturbances which originate in the freestream or on the body, and interact with instabilities in the boundary layer [6]. The breakdown of instabilities eventually causes the appearance of turbulent spots, which grow downstream and cause transition [7]. The transition location is in-

fluenced by many factors and thus is difficult to simulate and predict. These factors include freestream Reynolds number, Mach number, wall temperature, mass addition, freestream disturbances, and roughness [8]. In addition, many different physical mechanisms within the boundary layer can cause transition [9], but these mechanisms are poorly understood. Because of the complexities involved in the transition process, empirical correlations are often used to predict the location of transition for hypersonic flight vehicles [6].

1.2 Quiet Tunnels

Transition in hypersonic wind tunnels can occur much earlier than in flight due to high freestream noise levels [10]. Conventional hypersonic wind tunnels have turbulent nozzle-wall boundary layers. The turbulent eddies within the boundary layer radiate acoustic noise into the freestream, causing noise levels an order of magnitude greater than in flight [11]. This acoustic noise interacts with laminar boundary layers on models via a receptivity process and can cause early transition. Figure 1.1 shows a shadowgraph image of a cone at Mach 4.3 in a ballistics range, traveling from left to right [12]. The upper half of the cone has a laminar boundary layer with a several turbulent spots. The lower half of the cone has a turbulent boundary layer and some turbulent eddies are visible. The image shows acoustic noise radiating from both the turbulent boundary layer and the turbulent spots. The laminar boundary radiates much less noise (if any).

The photograph illustrates that in hypersonic wind tunnels, maintaining a laminar boundary layer on the nozzle wall will reduce acoustic noise levels that can interfere with transition experiments. These tunnels are referred to as quiet tunnels, because of their low noise levels (usually taken as the root-mean-square pitot pressure divided by the mean pitot pressure). The Boeing/AFOSR Mach-6 Quiet Tunnel at Purdue University (Chapter 2) is currently the only operational hypersonic quiet tunnel in

the world. During quiet-flow operation, the Mach-6 Quiet Tunnel has noise levels less than 0.05% [13].

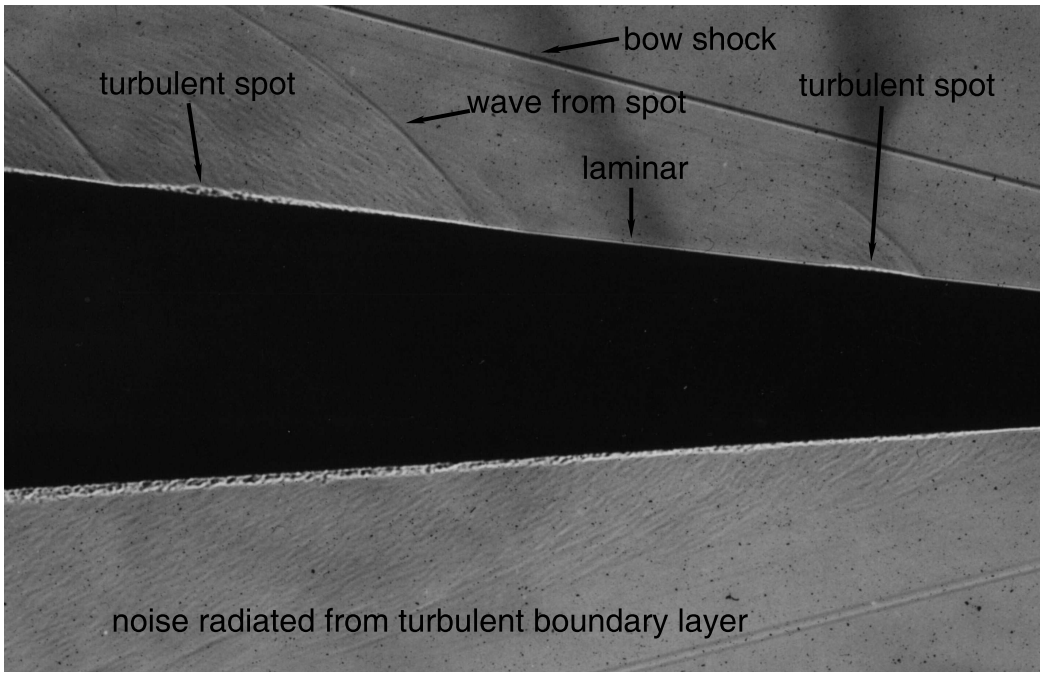

Figure 1.1. Shadowgraph photograph of acoustic noise radiating from a turbulent boundary layer. Experiment described in Reference 12. Photograph from Reference 11.

1.3 Stability Theory and e^N Method

Stability theory is used for computing growth rates of instabilities within a laminar boundary layer. These instabilities eventually break down and lead to turbulence. In the 1940's, Schubauer and Skramstad showed experimental results for the amplification and breakdown of instability waves leading to transition within a flat plate boundary layer at low speeds [14]. They were also able to alter the position of transition by introducing sinusoidal disturbances of various frequencies and amplitudes into the laminar boundary layer.

Using the linearized boundary-layer stability equations, a method to estimate the growth of these sinusoidal disturbances was developed, referred to as Linear Stability Theory (LST). LST uses small disturbance theory and a parallel flow assumption to reduce the governing equations to a linear form that can be easily solved. LST assumes that perturbations within a boundary-layer are composed of waves that propagate. For a two-dimensional perturbation, disturbance waves can be classified by a stream function solution:

$$\psi\left(x,y,t\right)=f\left(y\right)e^{i(\alpha x-\beta t)} \tag{1.1}$$

where x is a streamwise coordinate, y is a wall-normal coordinate, t is time, and α and β can be either real or complex, depending on whether the spatial or temporal solution is desired. The imaginary part of α then determines if the wave grows or decays in space. Mack found that for a compressible boundary layer, there were multiple solutions (or modes) to the linear stability equations [15]. The first-mode instability tended to dominate at lower speeds while the second-mode instability dominated at higher edge Mach numbers. The second-mode instability is the most unstable at hypersonic Mach numbers for slender, smooth, and axisymmetric geometries [16]. Modern computational codes use the Parabolized Stability Equations (PSE) to compute instability growth rates [17], which are considered more accurate than LST.

The computed growth rates can be used in correlations of transition location. The e^N method is a semi-empirical method for transition prediction based on the integrated growth rates of disturbances within the laminar boundary layer [18, 19]. The N factor is the integrated growth of the amplification rate $-\alpha_i$:

$$N=ln\left(\frac{A}{A_0}\right)=\int_{x_0}^{x}\left(-\alpha_i\right)dx \tag{1.2}$$

where x_0 is the location where the disturbance first becomes unstable. A is the disturbance amplitude at location x and A_0 is the disturbance amplitude at location x_0. Together with experimental observations of transition location, the e^N method can be used to correlate transition to a location with a particular N factor (usually 8-11 for quiet flow [20, 21]).

1.4 Roughness Effects on Hypersonic Transition

Research is needed to determine if a naturally-occurring roughness will cause transition during reentry, or to determine the largest roughness that will begin to affect the natural transition location [22]. Discrete roughness elements can also be used to trip an existing laminar boundary layer [23], for instance to prevent scramjet engines from unstarting [24]. Though significant progress has been made in understanding the physical mechanisms that cause transition behind a roughness element, they are not fully understood [25]. Much previous research was concerned only with transition locations and flow conditions, to collect data for engineering correlations [22]. Correlations are used with some success for many flight vehicles and are based on parameters such as Re_k, the Reynolds number based on roughness height [26]. Correlations, however, do not take into account the flow physics behind the roughness. If correlations are not used carefully they can lead to large uncertainties in transition location. Physics-based prediction methods that are based on the computed growth of instabilities in the wake of a roughness element are desired in order to reduce the uncertainty in predicting roughness-induced transition.

Roughness can be classified in two categories: distributed roughness and isolated roughness [25]. A distributed roughness can be an array of small roughness elements or natural imperfections in a surface material. Most reentry vehicles have distributed roughness inherent to the thermal protection system (TPS) [25]. The TPS on the Space Shuttle includes arrays of tiles which can act as a distributed roughness. The ablation of a heat shield during reentry can have a similar effect. An isolated roughness is typically much larger in scale. Examples of isolated roughness elements include protrusions such as space shuttle gap fillers or capsule tie rods, steps, gaps, and surface flaws or imperfections [22]. Though transition induced by distributed roughness is important, this project focuses only on isolated roughness elements. Figure 1.2 shows an example of an isolated roughness element: a protruding gap filler on the Space Shuttle. It was unknown exactly how this gap filler would affect transition

during re-entry. Due to this uncertainty, the gap filler was removed in orbit by an astronaut, prior to re-entry (Figure 1.3). If roughness-induced transition was better understood, perhaps this spacewalk could have been avoided.

A roughness element (if it is large enough) generally causes transition to occur earlier than it would in the smooth-wall case, with the transition location moving closer to the roughness as the height of the roughness is increased. A roughness can be small enough to have no effect on the transition location, in which case the roughness height is below its critical height. At heights larger than the critical height, the transition location moves closer to the roughness element. As the roughness height is increased further, the transition location will move to its closest location behind the roughness. This height is the effective height, beyond which the transition location does not move [22]. Both the critical and effective roughness heights can be influenced by other factors such as roughness shape or freestream noise conditions [29]. Figure 1.4 illustrates these concepts, showing data from a 5° half-angle cone in the Jet Propulsion Laboratory 12-in. supersonic wind tunnel [30]. An array of roughness elements was placed at $x = 5.0$ in. (where x is the distance along the surface from the apex) and the edge Mach number was 1.9. As the boundary-layer-edge Reynolds number (Re_e) is increased the transition location x_T moves closer to the roughness. For increasing Reynolds numbers, the boundary layer becomes thinner and the roughness appears larger. The critical height for each trip size is the roughness height where the transition location begins to depart from the smooth-wall value. At the highest Reynolds number, all three trips are effective and the transition location is as close to the roughness as possible, roughly 0.5 in. downstream. It should be noted that at hypersonic speeds a roughness must be on the order of the boundary layer thickness or higher in order to cause transition [8]. The size of the roughness element required to trip the boundary layer to turbulence increases with Mach number in hypersonic flows, due to the lower density near the wall at high Mach numbers.

The surface heating rate behind a roughness element is also important. Figure 1.5 shows heating data from a 5° half-angle cone in the NASA 20-in. Mach 6 Wind Tunnel

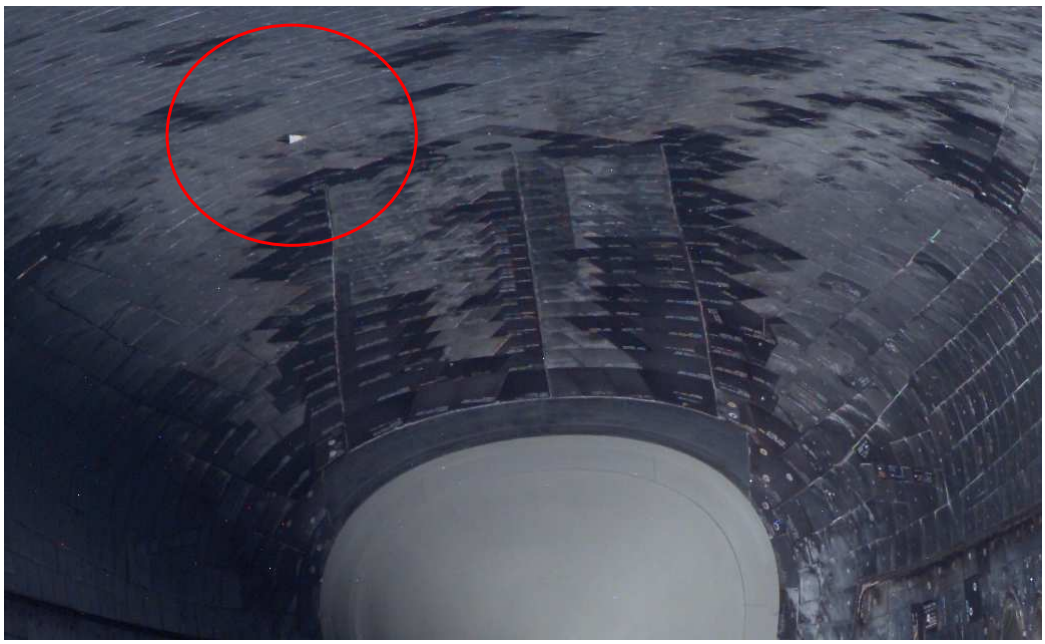

Figure 1.2. Example of an isolated roughness: protruding gap filler on Space Shuttle Mission STS-114, removed by astronaut in orbit [27].

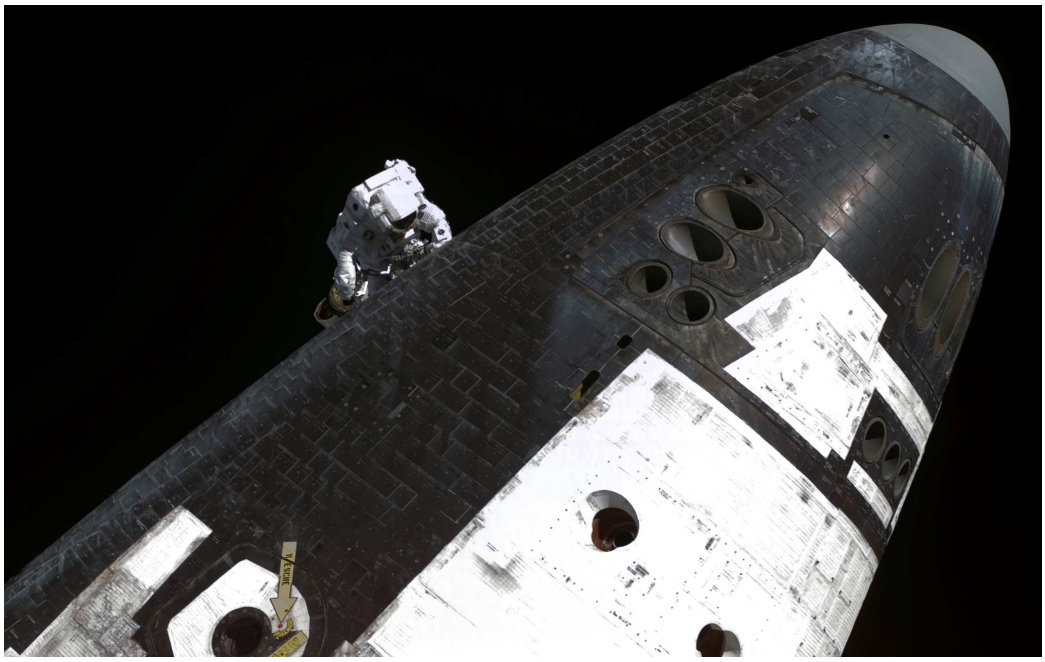

Figure 1.3. Spacewalk to remove protruding gap filler during Space Shuttle Mission STS-114 [28].

with a single diamond-shaped roughness element [25]. The cone axial location x is plotted on the horizontal axis, while the heat transfer coefficient ratio h/h_{ref} is plotted on the vertical axis. The reference heat transfer coefficient h_{ref} is the theoretical value at the stagnation point of a sphere. Several roughness heights were tested, and the larger roughnesses were more effective at moving transition closer to the trip at $x = 2.0$ in. Heating rates for both laminar flow and turbulent flow were predicted. Turbulent flow behind the roughness was indicated by an increase in h/h_{ref} to a value over twice the laminar rate. Both the measured laminar and turbulent heating rates agreed to within 5% of the computations [25], though an overshoot of the heating rate at the onset of transition was seen. This overshoot is commonly seen in the transition region. Figure 1.5 illustrates that heating rates can be predicted with reasonable accuracy, provided the boundary layer condition is known [31]. However, uncertainty in the roughness-induced transition location remains.

In order to develop computational models for predicting roughness-induced transition, the physical mechanisms leading to transition must be characterized. The physical structure within the wake of an isolated roughness element at hypersonic speeds may contain large disturbances such as streamwise vortices, similar to those seen at low speeds [32]. Oil-flow visualization by Whitehead in the late 1960's showed several large streamwise vortices within the wake of roughness elements on a rectangular wedge model in Mach 6.8 flow [33]. Figure 1.6, a photograph from Whitehead's report, shows oil flow patterns around tripping elements of various shapes. The local edge Mach number was 5.5 and the roughness height k was twice the boundary-layer thickness δ. The vortices are seen wrapping around the roughness and are oriented in the streamwise direction farther downstream. In addition, separated regions upstream and downstream of the roughness element are visible. The separation regions were observed to cause a shock (Figure 1.7), though additional shocks may also be produced by the roughness itself.

Recent flow visualization by Danehy et al. showed streamwise vortices within the wake of a roughness element, breaking down into turbulence as they convected

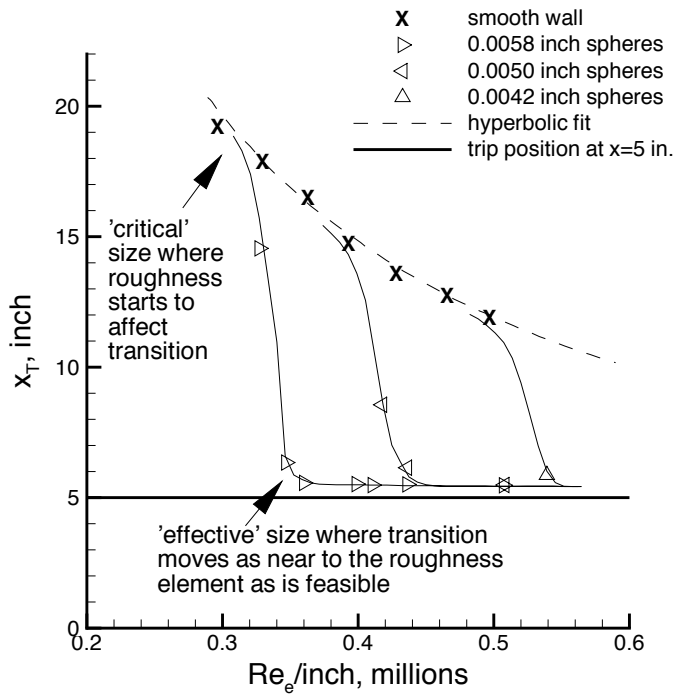

Figure 1.4. Critical and effective roughness (data from Reference 30 and figure from Reference 22).

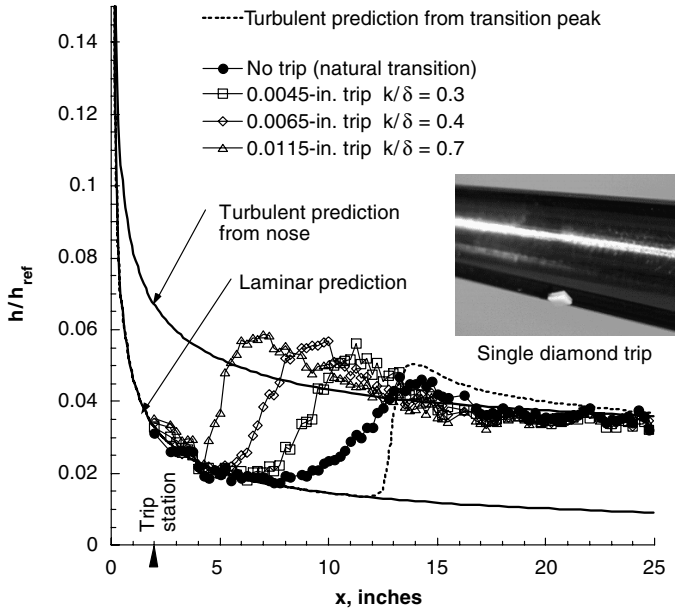

Figure 1.5. Heating in the wake of roughness elements of varying height (from Reference 25).

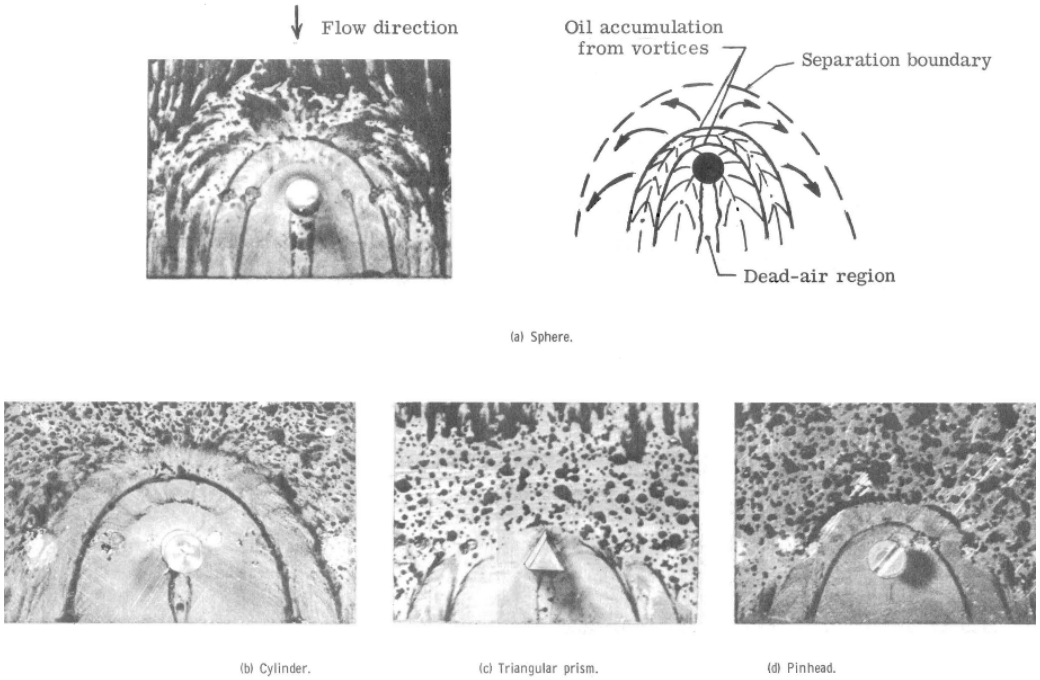

Figure 1.6. Oil-flow patterns of roughness elements, showing presence of streamwise vortices as well as separation regions (images from Reference 33). The local edge Mach number was 5.5 and $k/\delta = 2$.

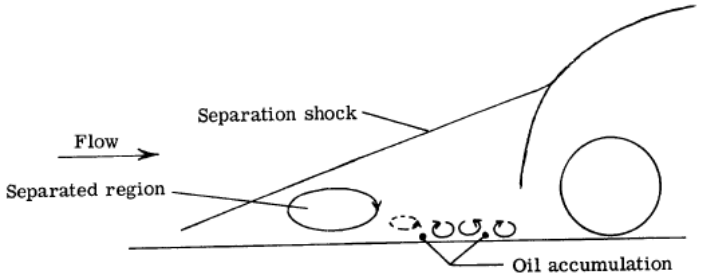

Figure 1.7. Diagram showing separation shock and vortices upstream of a roughness element (from Reference 33).

downstream [34]. Nitric oxide planar laser-induced fluorescence (PLIF) was used to visualize the flow in a plane parallel to the surface behind a 2-mm-radius hemispherical roughness. Figure 1.8 shows two images from these tests, which were conducted in the NASA Langley 31-in. Mach 10 Air Tunnel. In the images, flow is from left to right. A shadow is produced on one side of the roughness, caused by the blockage of the laser sheet. The vortex pattern can be seen in both images and the vortices appear more unstable in the higher Reynolds number test. These large-scale disturbances likely play an important role in roughness-induced transition, though smaller-scale instabilities from the unstable shear layer may also be important [22,35]. The compressibility of high-Mach-number boundary layers tends to have a stabilizing effect on large scale vortical disturbances [36], suggesting that roughness-induced transition "...results from a race between unsteady fluctuation growth (in the unstable wake) and the rapid relaxation of the basic state toward a spanwise-uniform Blasius flow" [37]. Computations by Chang and Choudhari showed that these convective instabilities may exist even in the absence of large vortical disturbances [38]. Recent work by Choudhari et al. showed that the modal shape and growth rates of shear layer instabilities in a hypersonic roughness wake can be computed [36]. Experiments are needed to assist in the development of these computational methods.

1.5 Experimental Objectives

Recent progress has been made using computations to characterize the wake of hypersonic roughness elements and compute the growth rate of roughness-induced instabilities. Semi-empirical transition prediction methods such as the e^N method can be used to reduce uncertainty in the roughness-induced transition location for hypersonic vehicles. Experiments will be needed to develop and verify the computations. Detailed measurements of the growth of instabilities within the wake are desired. Ergin and White reported detailed hot-wire measurements of instabilities in the wake of cylindrical roughness elements at low speed [37]. At high speed, how-

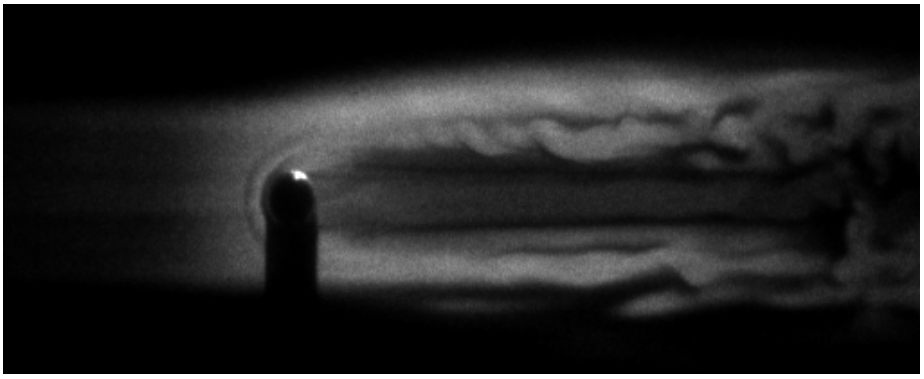

(a) Lower Re_∞ case.

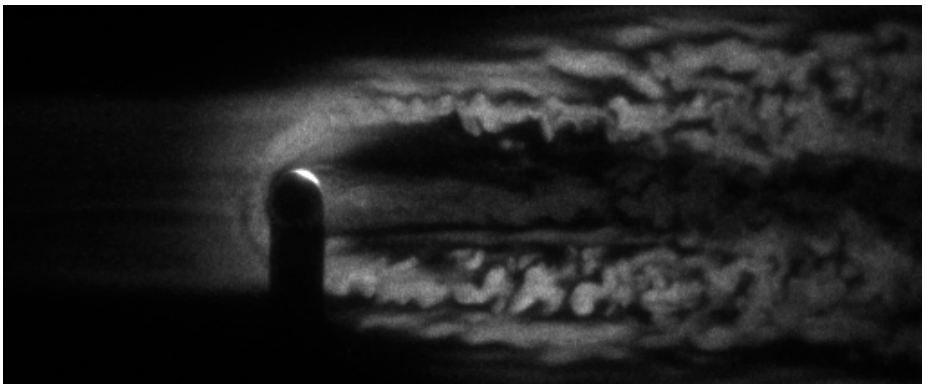

(b) Higher Re_∞ case.

Figure 1.8. Streamwise vortices in the wake of a 2-mm-radius hemispherical roughness using nitric oxide planar laser-induced fluorescence. Plan view with flow from left to right. Images from Reference 34.

ever, it is difficult to make detailed wake measurements. A laminar boundary layer for testing roughness elements is desired, but boundary-layer heights on models in hypersonic test facilities are often small (on the order of 1 mm or less). A thicker boundary layer would reduce probe interference effects, increase spatial resolution for making detailed measurements, and reduce the frequencies of instabilities. The nozzle wall of the Boeing/AFOSR Mach-6 Quiet Tunnel (BAM6QT) at Purdue University can be used to provide the thicker boundary layer desired for these experiments. The BAM6QT can be operated with a laminar boundary layer up to 20-mm thick and

a variable-height cylindrical roughness element can be used to introduce instabilities into the nozzle-wall boundary layer. The objectives of this project were to:

- Develop hardware for measuring within the the wake of an isolated roughness on the nozzle wall of the Boeing/AFOSR Mach-6 Quiet Tunnel
- Use temperature-sensitive paint to determine temperatures on the insulated nozzle wall, downstream of the roughness, to identify the wake region
- Explore the feasibility of wake instability measurements using hot-wire anemometry and pressure transducers
- Search for evidence of roughness-induced wake instabilities in a laminar boundary layer at Mach 6

2. BOEING/AFOSR MACH-6 QUIET TUNNEL

The design of the BAM6QT began in 1996 with the goal of creating a hypersonic test facility with noise levels comparable to flight [13]. After a long shakedown period, the tunnel became capable of quiet flow near its designed stagnation pressure of 150 psia in September 2006 [39]. The maximum stagnation pressure for quiet flow operation is currently above 160 psia [40].

The BAM6QT is a blowdown facility using a Ludwieg tube design, a long tube with a converging-diverging nozzle (Figure 2.1). During operation, the upstream portion of the tunnel is filled with high-pressure air while the region downstream of the diffuser is evacuated. The two regions are separated by a double-burst-diaphragm assembly. The diaphragms are then broken to initiate the flow. A shock wave travels into the vacuum tank and an expansion wave travels upstream, accelerating the flow to Mach 6. The expansion wave enters the driver tube, where it reflects back and forth every 0.2 s between the end of the driver tube and the contraction. After each reflection of the expansion wave, the pressure in the driver tube drops quasi-statically and the Reynolds number decreases. During a typical quiet run, the stagnation pressure in the driver tube decreases by 15–20% and the freestream Reynolds number decreases by 5–10%. The hypersonic flow portion of the run typically lasts 3–5 seconds depending on test conditions, model type, and diffuser efficiency. As the run progresses, the pressure in the vacuum tank rises. When the upstream-to-downstream pressure ratio is no longer sufficient to sustain hypersonic flow, the tunnel "unstarts" and the flow becomes subsonic.

The Boeing/AFOSR Mach-6 Quiet Tunnel was designed for low-cost operation. The single-shot Ludwieg tube design is less costly than traditional blowdown hypersonic facilities because less power is required for the air-supply system, however the tunnel cannot attain sustained flow for periods of more than a few seconds. The

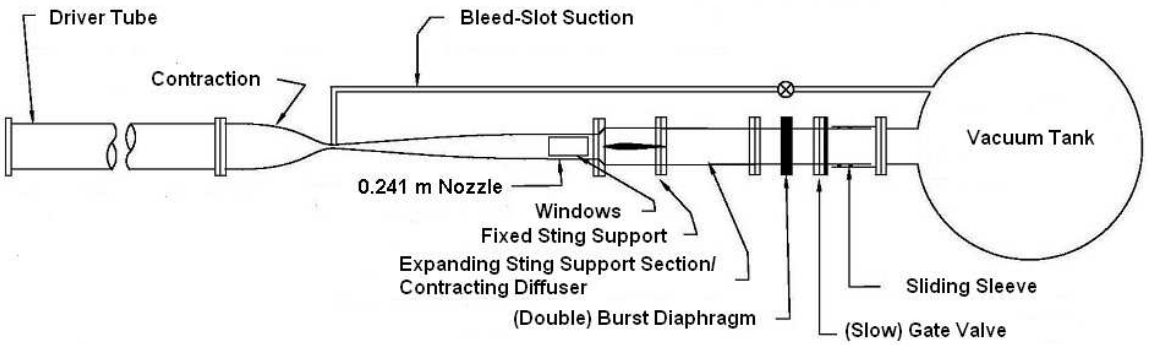

Figure 2.1. Schematic of the Boeing/AFOSR Mach-6 Quiet Tunnel.

pressurization of the tunnel requires only one 50-hp compressor, with a boost pump for attaining pressures higher than 140 psia (965 kPa). Though the run time of the BAM6QT is only a few seconds, the high sampling rate of modern instrumentation is more than sufficient for instability and transition measurements [13]. For instance, the oscilloscopes used to record data during tunnel operations can sample up to 5.0 MHz over a 10-s signal length. Instability frequencies are usually on the order of hundreds of kilohertz or less. The tunnel can be operated by one graduate student and does not require a full-time technician or support staff.

The tunnel is filled with high-pressure air from a Quincy QGB-50 compressor. The compressor maintains the building air supply at 140 psia (965 kPa). The tunnel is normally filled using the building air supply. A Corken D-291 boost pump is used for higher pressures up to 300 psig (2,170 kPa) [41]. The building air is dried by a Van Air HL-350 dryer system to prevent condensation and is filtered to remove large particles. Air enters the upstream end of the 37.3-m-long driver tube (Figure 2.2) through additional filters. The air entering the driver tube is controlled using a 0–10 V Proportion-Air QB1TFEE/RQ008 pressure regulator. The regulator voltage is adjusted manually by the student operator to fill the driver tube. As the air enters the driver tube, it is heated to 433 K with a 30 kW circulation air heater and

controller [42]. When the flow accelerates to Mach 6 the static temperature drops, so the air in the driver tube must be heated to prevent condensation. The driver tube is covered with insulation and four power supplies are used to heat the stainless-steel driver tube to 433 K. The power supplies are each capable of a 750-amp maximum current at up to 10 volts. The current flows directly through the driver tube, heating it. A surface-mounted thermocouple and an Omega CN9000A controller are used to hold the driver tube temperature constant.

Figure 2.2. View of driver tube from the main building bay.

Quiet flow is achieved through several design features that delay transition in the nozzle-wall boundary layer, though at high Reynolds numbers the boundary layer is still turbulent [13]. Upstream of the throat, a bleed slot is used to remove the existing boundary layer from the driver tube. The boundary layer is removed through a bleed air line that runs into the vacuum tank, and the line is opened by a fast-acting valve that activates automatically when the run begins [43]. After the boundary layer is removed, a new laminar boundary layer begins at the throat of the nozzle. The tunnel can also be operated at conventional noise levels with a turbulent boundary layer on

the nozzle wall by disabling the fast-acting valve and preventing suction through the bleed slot. The cross-section of the nozzle is circular to avoid instabilities caused by a non-axisymmetric geometry or sharp corners. To limit concavity and the resulting Görtler instability, the 2.6-m-long nozzle (Figure 2.3) is longer than conventional nozzles [44].

The first 0.76 m of the nozzle features a polished electroform nickel finish to remove as much roughness and waviness as possible. The surface of the beginning of the nozzle is most critical in achieving quiet flow because the boundary layer here is thin and more susceptible to the effects of small surface imperfections. Great care is taken to ensure that dust or other small particles do not infiltrate this section of the nozzle, as even a small particle could decrease quiet flow performance. As the stagnation pressure and thus the unit Reynolds number of the tunnel is increased, the boundary layer here becomes smaller and more susceptible to roughness effects. The maximum stagnation pressure at which the tunnel is capable of quiet flow is a measure of tunnel performance.

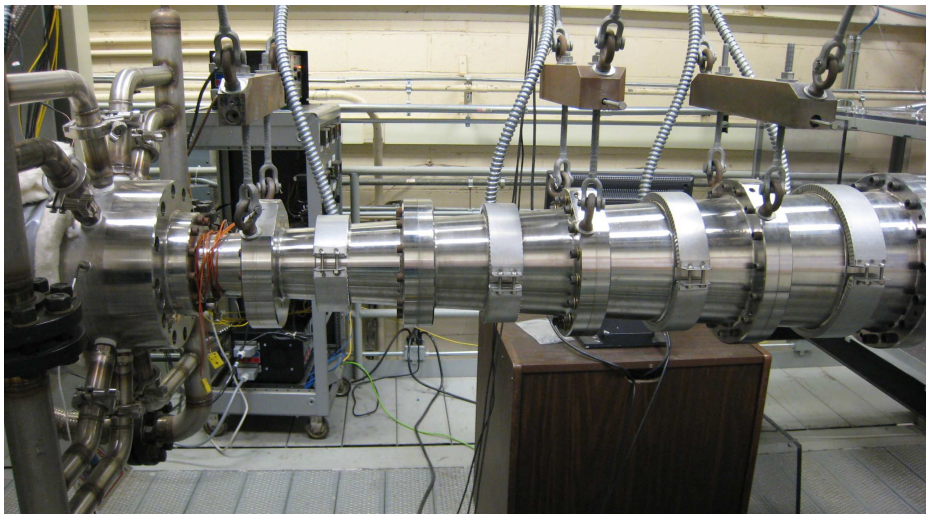

Figure 2.3. Exterior of the throat and nozzle. The bleed system piping can be seen in the left portion of the photograph.

The last 0.77 m (30.25 in.) of the nozzle serves as the test section of the BAM6QT. The end of the nozzle (Figure 2.4) has a nearly-constant 0.24-m (9.5-in.) diameter and eight window inserts, at 90° azimuthal locations. The inserts are used for instrumentation as well as optical access. The original stainless-steel inserts were machined along with the nozzle and are referred to as the "window blanks". The four upstream windows are referred to as the "small" windows and are 10×3.1 in. The nozzle-wall hot-film array is located on one of the small window blanks, which has been modified to pass the wires out to the hot-film anemometer. Because all four small windows are interchangeable, multiple configurations can be used for different experiment setups. Of the four downstream windows, the "medium" windows on the top and bottom of the nozzle are 14.125×4.1 in. while the "large" side windows are 14.125×7.4 in. A slotted medium insert is used to mount various probes that are controlled by the traverse system. Two large window inserts with optical access have been in regular use. A large rectangular acrylic window is used at tunnel pressures lower than 153 psia. A window insert with two 4-in.-diameter porthole windows is capable of withstanding tunnel pressures higher than 153 psia. A medium rectangular plexiglas window has recently been built and will be used primarily for oil-flow visualization.

A traverse system is mounted on the last section of the nozzle and is used for holding probes of various types (Figure 2.5). Both hot-wire and pitot probes are commonly used to measure in the freestream, or the boundary layer of a model or the tunnel wall. The probes are suspended in the nozzle using double-wedge probe supports. The probe support enters the nozzle through a 12.5-in.-long slot that has been machined into a medium window insert on the top of the tunnel. The slot is located on the tunnel centerline and allows the streamwise position of the probes to be changed (but only between runs). A brass traverse bar is clamped on top of the slot in order to compress an o-ring and seal the tunnel. Each probe support features three 0.375-in.-diameter rods, which are clamped to a Parker rail positioner. Ball bearings in the brass traverse bar allow vertical movement of the rods. The center rod is hollow in order to pass probe wires, and is sealed with a Conax pressure fitting.

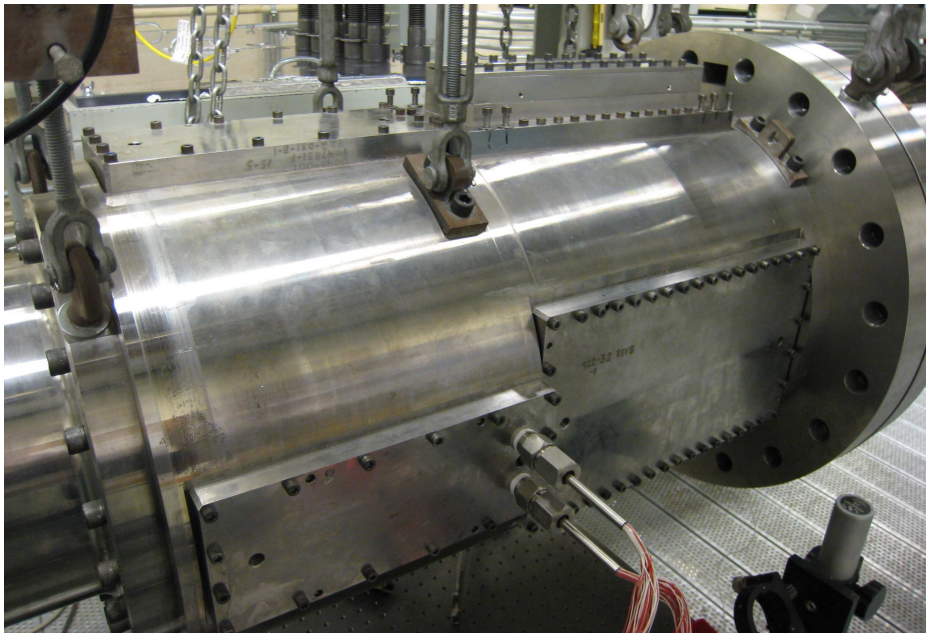

Figure 2.4. End of the nozzle, which serves as the test section. The nozzle window inserts are visible.

A Parker rotary step motor is used to turn a ball screw that raises and lowers the linear positioner and probe support. A GT6-L5 drive controller and Motion Planner software are used to design movement profiles during a run. Additional details of the traverse system operation are reported by Swanson [45]. Installation of a new traverse system with lower electronic noise levels is currently planned.

New sting-support and diffuser sections located downstream of the nozzle were installed in December 2007 in order to be able to start larger blunt models (Figure 2.6). A adapter flange creates a 45° expansion from the 0.24-m-diameter nozzle to the 0.36-m-(14.125-in.-)diameter sting-support section. The expansion was designed to prevent shock-induced boundary-layer separation from propagating upstream. Issues relating to starting blunt models with the new diffuser are documented in References 43 and 46.

Two sting-support section inserts were built in order to improve the performance of the new diffuser. A nylon ramp insert (Figure 2.7(a)) was designed to decrease the 45° expansion angle to a 9° expansion angle. When installed, the upstream portion of

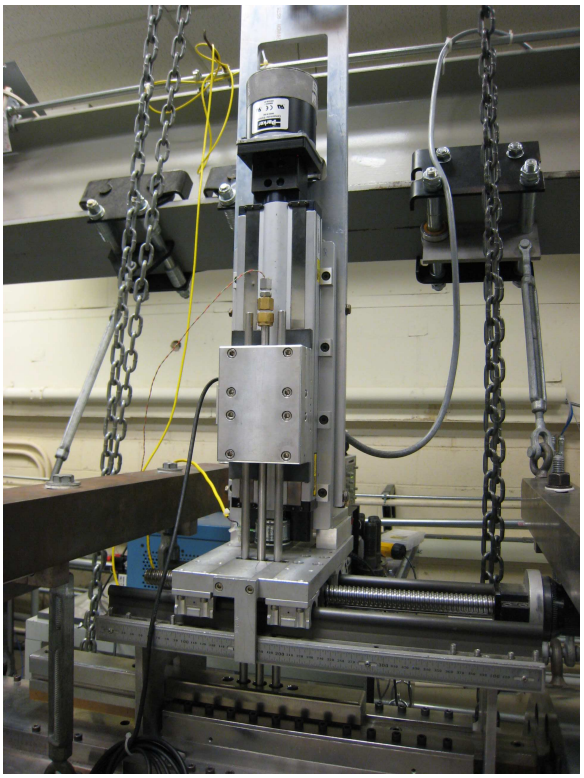

Figure 2.5. Traverse system.

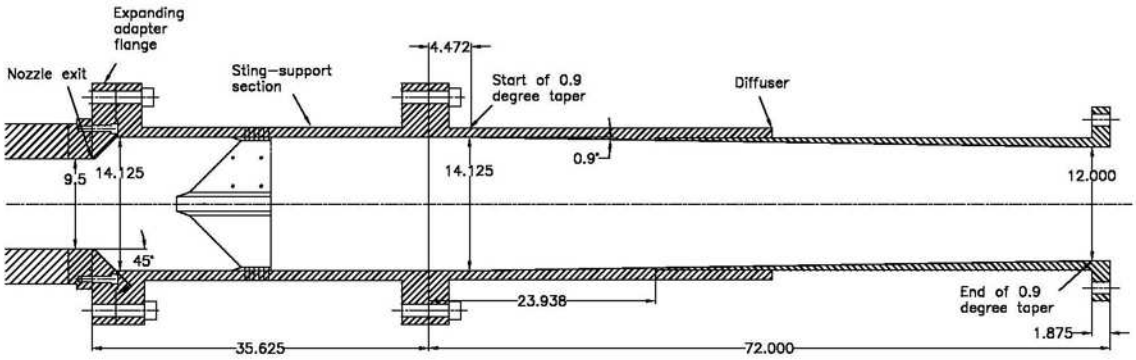

Figure 2.6. Sting-support section and diffuser section schematic. Dimensions in inches.

the nylon ramp insert is flush with the interior edge of the nozzle. A 0.24-m-diameter pipe insert (Figure 2.7(b)) can be mounted to the sting support section with four brackets and is used to create a variable-width slot. The slot was designed to create a suction effect and decrease the likelihood of boundary-layer separation. The slot width can be changed from 0 to 1.5 in. A new pipe insert extension that extends farther down the diffuser section has been completed, and testing of the new insert is underway [40].

A 1.83 m (72 in.) tapered diffuser section leads to the double-burst-diaphragm section. Two 13.6-in.-diameter aluminum or acetate diaphragms are used in every run and are held apart by a set of burst diaphragm rings, creating a gap. Prior to each run, the diaphragms are installed and the upstream portion of the tunnel is pressurized to the desired stagnation pressure. The downstream portion of the tunnel is evacuated to vacuum and the gap between the diaphragms is maintained at half of the upstream pressure. Diaphragms of various materials and thicknesses have been selected to cover most of the operating pressure range of the tunnel. The run is started by evacuating the air in the diaphragm gap, causing the diaphragms to break in rapid succession. The remnants of the diaphragms go into the vacuum tank. After the run, a slow gate valve is closed to isolate the vacuum tank from the tunnel. The building air supply is used to bring the tunnel to atmospheric pressure. A hydraulically-actuated sliding sleeve allows the tunnel to be opened and closed to change the diaphragm assembly or models. Downstream of the sliding-sleeve section, piping leads to the 113-cubic-meter (4,000-cubic-foot) vacuum tank. A Leybold SV630 vacuum pump is capable of bringing the tank from atmospheric pressure to 1–2 torr in 60 minutes [47], though after each run the vacuum tank pressure only rises to 200–300 torr.

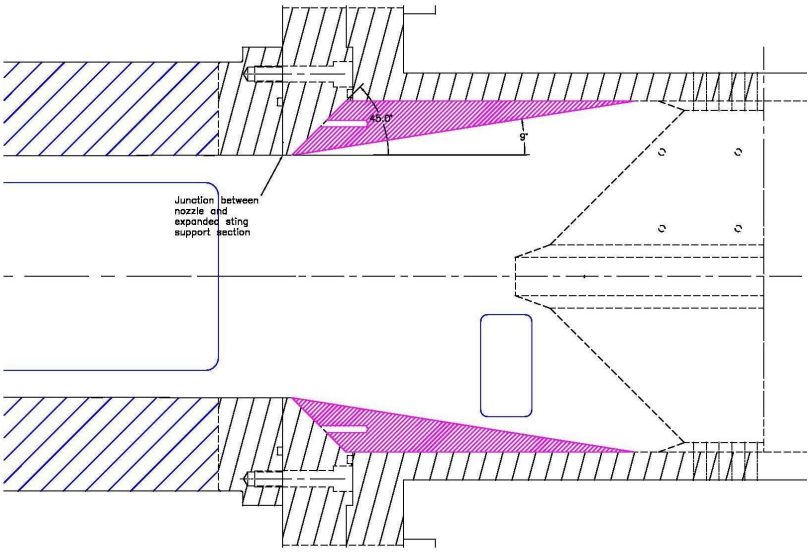

(a) 9° ramp insert.

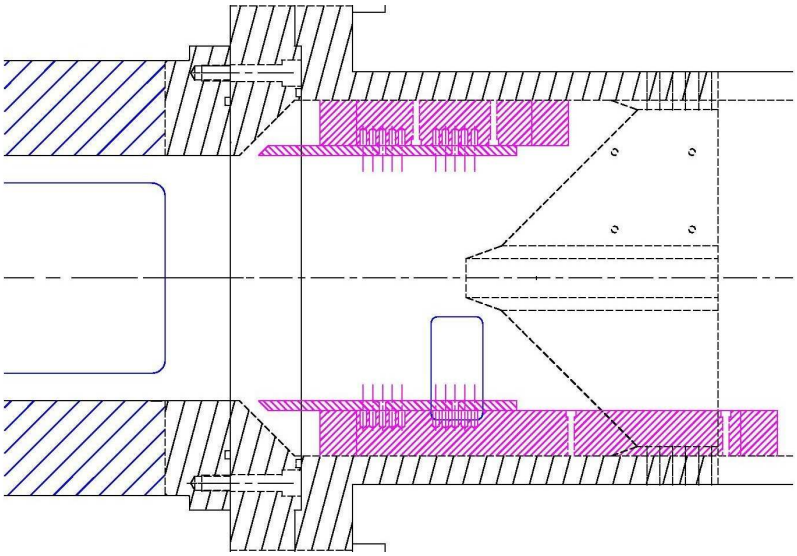

(b) Pipe insert.

Figure 2.7. Sting-support section inserts.

3. TEST ARTICLE AND INSTRUMENTATION

3.1 Roughness Element

A Starrett model 263L–38TN micrometer head was used as a cylindrical roughness element (Figure 3.1(a)). The height k of the 5.97-mm-(0.235-in.-)diameter roughness element can be changed from 0.00–24.31 mm and is accurate to ± 0.05 mm. The roughness height was adjusted prior to each test using the micrometer readout on the outside of the tunnel. The roughness element was located in the nozzle of the BAM6QT at tunnel coordinate $z = 1.924$ m (75.749 in.), mounted in a specially designed circular insert in the upstream window blank (Figure 3.1(b)). The four upstream window sections of the BAM6QT nozzle are interchangeable, allowing the roughness element to be placed on either the lower wall or side wall. The lower-wall configuration was used for hot-wire and pitot-probe measurements while the side-wall configuration was used for temperature-sensitive paint measurements. Three locations in the circular insert allow the spanwise position of the roughness element to be changed, so that measurements can be taken off the center of the wake. The circular insert has a location in the center as well as ± 2 diameters off-center. In the future, more inserts can be manufactured to allow measurements in different spanwise planes of the roughness wake. Measurements taken with the roughness in the off-center position are not in a plane parallel to the roughness, due to the curvature of the tunnel wall. This effect would have to be considered in precise computational simulations.

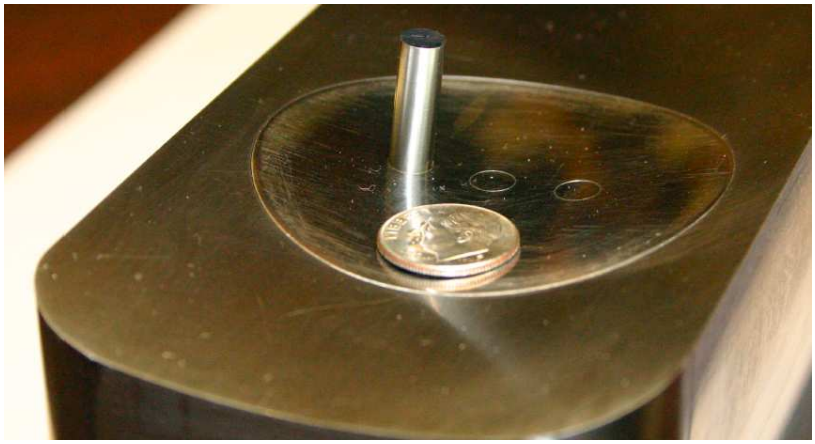

(a) Close view.

(b) Installed in window blank.

Figure 3.1. Cylindrical roughness element with 0.235-in.-diameter.

3.2 Temperature-Sensitive Paint

Temperature-sensitive paint (TSP) is a global measurement technique capable of obtaining surface temperatures on a model without significant interference with the flow [48]. TSP can be used to detect hypersonic boundary-layer transition because heat transfer is higher on the surface of a model when the boundary layer is turbulent. While thermocouples, hot films, and heat-flux sensors can also detect transition, these single-point sensors lack the ability to map the entire surface of a model. In addition, sensors applied to the surface of a model can interfere with the boundary-layer transition process and affect results. Temperature-sensitive paint can be applied to the entire surface of a model and provides excellent spatial resolution.

In the temperature-sensitive paint method a luminophore molecule is dissolved with a solvent, mixed into a clear paint, and applied to the surface of a model. An insulator is often applied before painting to reduce heat transfer to the surface and increase the surface temperatures. When the paint is excited with a specific-wavelength light the luminescent molecules become excited and fluoresce. The excited molecules emit light of a longer wavelength as they return to their unexcited state [48–50]. When the temperature of the luminescent molecules is higher, the molecules are more likely to lose their excited energy through other means (such as vibration) and the intensity of the emitted light decreases. This process is known as thermal quenching, and is the major mechanism in TSP [48]. Due to thermal quenching, the intensity I of the emitted light can be related to the temperature T.

A charge-coupled device (CCD) camera is typically used to capture images of the temperature-sensitive paint intensity. Cooled scientific-grade CCD cameras help reduce noise in the image and offer high resolution [50]. Two images are taken: one before the experiment when the paint is at a known temperature and one during the experiment (known as the "flow off" and "flow on" images, respectively). A "dark image" can be taken and used to subtract ambient light and camera noise from the images [48]. In post-processing, the two images are aligned and a ratio of the flow

on and flow off images is obtained. The image alignment accounts for movement of the model during the experiment and taking the ratio minimizes the effect of local variations in the TSP thickness. A calibration is then applied to convert the intensity ratios to temperature ratios, such that

$$\frac{T}{T_{\text{ref}}} = f\left(\frac{I}{I_{\text{ref}}}\right) \tag{3.1}$$

where I is the paint intensity at an unknown temperature T and I_{ref} is the intensity at a known reference temperature T_{ref}.

While the TSP method can provide quantitative temperatures from a calibration, it currently provides only qualitative heat-transfer results. Efforts are underway at Purdue University to improve the accuracy of heat-transfer measurements when using TSP [51]. Measurements in this project will be reported as temperatures because they are intended for qualitative purposes only (to identify heating in the wake of the roughness element).

Temperature-sensitive paint was used to visualize the temperatures in the wake behind the isolated roughness element. The TSP measurements were intended to identify preliminary flow features within the wake of a laminar boundary layer at various freestream Reynolds numbers. A diagram of the location of the roughness element and the region examined using TSP appears in Figure 3.2.

The inside of the large window blank, downstream of the roughness, was covered with a 0.0045-in.-thick adhesive-backed PVC insulator. The insulator layer was applied carefully to limit the occurrence of air bubbles, though the varying radius of curvature of the window blank made this difficult. Small bubbles remaining after application were removed by puncturing a small hole in the insulator to evacuate the trapped air. Some air bubbles developed during testing as a result of the rapid depressurization during the start of each run. These air bubbles are visible in the TSP photos and temperature data as regions of low temperatures.

The insulator was airbrushed with Ru(Bpy) dissolved in ethanol, mixed with Dupont/Nason 496-00 clear urethane automotive paint and activator. After the paint was allowed to dry, registration marks were applied onto the paint using a milling

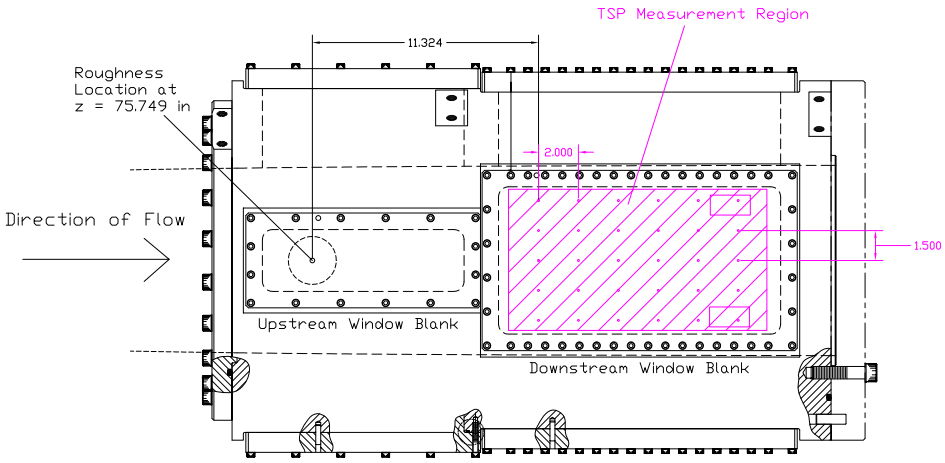

Figure 3.2. Diagram of roughness location and TSP measurement region in the BAM6QT nozzle. All dimensions in inches.

machine. A Sharpie fine-point permanent marker was used to mark the desired location of each reference mark and larger rub-on dots were applied later. Registration marks were applied at a 2-in. axial spacing and 1.5-in. vertical spacing, beginning at $z = 87.1$ in. (about 11.3 in. downstream of the roughness element). These marks were used for image alignment and flow feature location.

The painted window blank was installed in the tunnel on the side opposite the large plexiglas window. A Cooke Corporation PCO.1600 camera and blue LED were set up on the optical bench to image through the plexiglas window and view the TSP region. A wide-angle 24-mm lens was used to view the entire painted window blank. After pressurizing the tunnel and prior to each run, a background image was acquired with both the blue LED and room lights off. The background noise levels from this image were subtracted from all images during that run. Immediately before each run, a "flow off" image was acquired with the blue LED on to provide the intensities at the assumed reference temperature of 300 K. During each run, a signal generator was used to trigger the camera and acquire images at a rate of two images per second. This speed was limited by the exposure time and the time it takes to trigger the camera. These "flow-on" images were aligned with the "flow-off" image using software from

Innovative Science Solutions, Inc and a ratio of intensities between the two images was obtained.

A TSP calibration rig at the Aerospace Sciences Laboratory was used to calibrate the paint intensity to temperature. A 1×1 in. aluminum calibration coupon was covered with PVC insulator and painted along with the large window blank. The small coupon was attached to a metal bar in the calibration rig using thermal paste and the bar was heated with heat-transfer fluid to temperatures of 295–320 K. A controller was used to change the fluid temperature and 20 minutes were allowed for the fluid and bar to reach steady-state temperature. A temperature sweep up to 320 K and then back down to room temperature was performed, such that certain temperatures were measured twice. The temperatures were read from a thermocouple attached to the metal bar. The PCO.1600 camera and blue LED array were used to measure how the intensity of the paint varied with temperature. All calibrations were performed at one atmosphere. The TSP was not expected to be pressure-dependent, at least at low pressures, due to the impermeability of the clear-coat paint. However, the pressure dependency of the TSP was not tested.

A reference temperature of 300 K was selected because the temperature of the tunnel wall in the "flow off" images is assumed to be close to room temperature. The thick stainless-steel tunnel wall is assumed to act as a heat sink at room temperature. At this temperature, the paint was excited with the LED array and an image was taken. A dark image (with the LED array off) was taken and the background noise from this image was subtracted from the calibration image. The average intensity of a 100×100 pixel area in the center of the coupon was recorded.

The data were fit to a second-order polynomial to convert intensity ratios to temperature ratios. The reference temperature was always assumed to be 300 K (Figure 3.3). The red vertical bars show the actual intensity ratios measured on the tunnel wall, which varied between 0.95–1.0. Some points at temperatures much lower than 300 K were removed from the calibration in order to increase agreement in the desired measurement range of 300–305 K. There exists a large amount of scatter

in the calibration data for unknown reasons. However, the calibration was deemed acceptable because the results are intended for qualitative use only and temperatures are not being used to calculate quantitative heat transfer values.

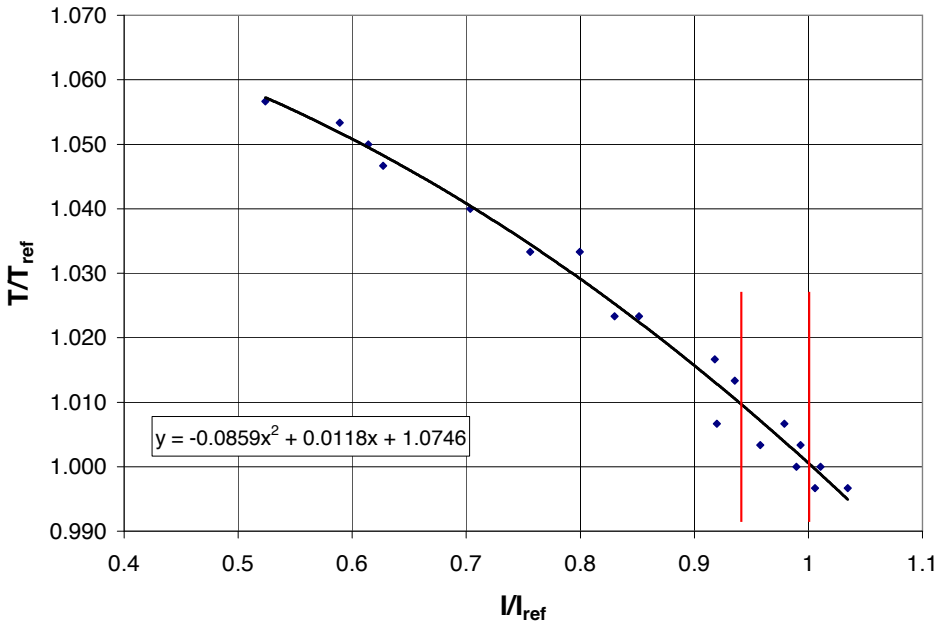

Figure 3.3. TSP calibration. The red vertical bars show the typical measured intensity range on the nozzle wall.

3.3 Hot-Wire Anemometry

Instabilities in hypersonic flow are ideally measured using hot-wire anemometry because hot wires provide the high frequency response needed to measure second-mode waves [52]. Hot-wire anemometry works on the principle that the resistance R of a metal varies directly with temperature T. Near room temperature, the variation for most metals is approximately linear, such that

$$\frac{R - R_{\text{ref}}}{R_{\text{ref}}} = \alpha(T - T_{\text{ref}}) \tag{3.2}$$

where R_{ref} is the resistance at a reference temperature T_{ref}, and α is the temperature coefficient of resistance (per unit temperature) [53]. As the temperature of a metal decreases, its resistance must also decrease.

A hot wire is a thin metal wire that is heated with an electrical current and inserted into the flow. Usually, an anemometer is used to hold the wire at a constant temperature (constant resistance) using controller circuitry. Other hot-wire anemometry controllers hold the wire at either a constant temperature or a constant voltage. A example of a constant-temperature anemometer (CTA) controller circuit appears in Figure 3.4 [53]. R_1 and R_2 are known resistances in the circuit. For a "bridge ratio" of 1:1, R_1 and R_2 are equal. An amplifier is used to maintain an equal voltage drop across the hot wire and R_3, by varying the current through the wire. In a steady state, the resistance of the hot wire will equal the resistance of the resistor R_3, known as the control resistor. Thus, the hot wire will be maintained at a constant temperature.

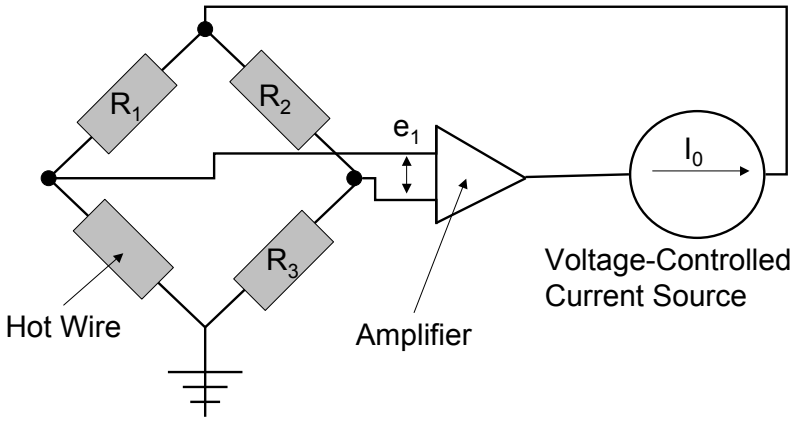

Figure 3.4. Example of a constant-temperature anemometer circuit, redrawn from Reference 53.

As air flows over the wire, convective heat transfer occurs and the resistance of the wire decreases with temperature. The control circuitry then applies a higher voltage to increase the current through the wire, and maintain its temperature. Due to the high gain of the amplifier and small diameter of the wire, this process occurs

very quickly and gives the hot wire excellent frequency response [53]. The voltage required to keep the wire at a constant temperature can then be recorded from the anemometer and correlated to the flow velocity (at low speeds). At supersonic Mach numbers, the voltage required to keep the wire at a constant temperature is calibrated to mass flux [54], since both the density and velocity of the flow are changing. Both uncalibrated and calibrated hot-wire results are reported in this project in the wake of the roughness element on the nozzle wall.

The stainless-steel hot-wire probes used in the roughness wake experiments were built by Jim Younts of the ASL machine shop. Four new hot-wire probes were built with a longer knife-edged strut in order to probe the thicker nozzle-wall boundary layer with minimal flow interference (Figure 3.5). Each probe is numbered 1–4. Earlier hot-wire probes used in the BAM6QT are detailed in References 55 and 56, but the shorter struts would have increased interference on the nozzle wall. The new probes have a 51-mm-(2-in.-) long strut as opposed to the 19.9-mm-long strut on the original design. Platinum–Rhodium wires with a 0.0002-in. diameter were used in this project. A TSI IFA-100 CTA was used to control the wire temperature and provide an output voltage. The 1:1 bridge was used. A control resistor was used to "set" the wire temperature, and the resistance ratio between the control resister and probe resistance was chosen to be 1.7–1.9, as recommended by Rufer [56]. To record data, the output voltage of the anemometer was connected via a BNC cable to an oscilloscope.

Hot-wire probe #1 was used for all of the calibrated measurements, though results from other uncalibrated hot wires are reported. The wire had a 0.0002-in. diameter and survived 13 runs, including three runs for calibration. The probe had a room-temperature resistance of 6.46 Ω and an 11.18-Ω control resistor was used in the anemometer. The estimated wire temperature was between 700–900 K, though the actual temperature coefficient of resistance of the particular wire was unknown. Measurements of the temperature coefficient of resistance of similar probes were used to estimate the wire temperature.

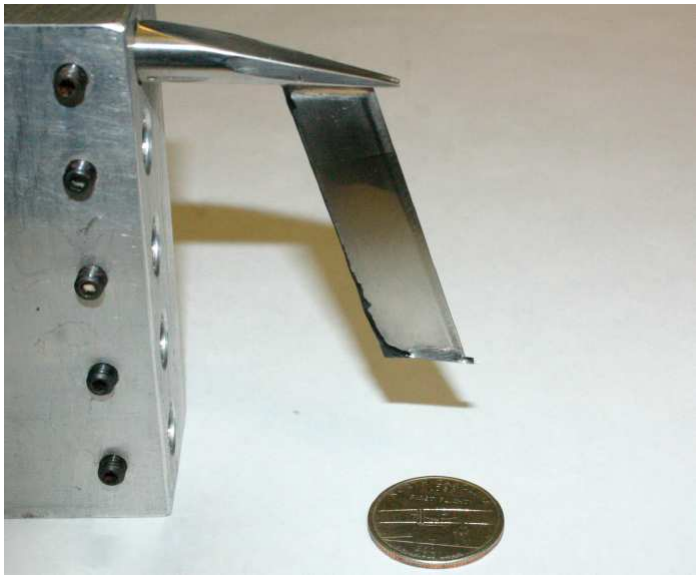

Figure 3.5. Hot-wire probe with 51-mm-(2-in.-)long strut.

The hot wire was tuned at atmospheric pressure while installed in the tunnel with no flow. A built-in square-wave generator on the TSI anemometer was used for tuning with the maximum-amplitude square wave. The square wave is used to provide a disturbance to the controller circuit and monitor the dynamic response. The gain and cable compensation were adjusted until a high frequency response was obtained with no oscillations (Figure 3.6). The frequency response of the hot wire was 83 kHz due to difficulties tuning this particular wire with a high gain. However, the hot-wire frequency response was sufficient to measure instabilities in the thick nozzle-wall boundary layer.

Several methods were used to reduce the risk of breaking the hot wire in the tunnel. The anemometer was switched from "run" mode to "standby" mode as soon as the hypersonic portion of the run ended, prior to closing the gate valve, to reduce the risk of breakage during the blowdown at the end of each run. The anemometer was kept in standby mode at all times except just prior to each run. In addition, the external control resistor and wire bundle were kept isolated so that they were not

bumped when the anemometer was in run mode. A sudden movement of the external resistor and wire bundle had been observed to cause a previous hot wire to break.

When it was determined that the hot wire was able to survive multiple runs in the tunnel, a mass-flux calibration was performed. The wire was placed in the freestream flow during three runs at different initial stagnation pressures. The wire was moved to a height of 40.2 mm above the wall at tunnel coordinate $z = 74.9$ in., 0.85 in. upstream of the roughness location. It was assumed that this height was larger than the boundary layer thickness at the lowest stagnation pressure. At $p_0 = 20$ psia the boundary-layer thickness is approximately 19 mm (0.75 in.) [57]. A plug was used in the roughness insert such that the tunnel wall was smooth. In this configuration, three quiet runs were performed at initial stagnation pressures of 90, 40, and 20 psia to cover a wide range of mass fluxes. The mass flux ρu was calculated using the equation

$$\rho u = p_0 M \sqrt{\frac{\gamma}{R_{\text{gas}} T_0} \left[1 + \frac{(\gamma - 1)}{2} M^2\right]^{\frac{-\gamma-1}{\gamma-1}}} \tag{3.3}$$

from Reference 56. The perfect gas law and isentropic relations were used to calculate mass flux as a a function of tunnel stagnation pressure and temperature. The stagnation temperature was assumed to decrease isentropically as the stagnation pressure drops during the run. The Mach number was assumed to be 6.0, though as the probe was upstream of the nozzle exit the Mach number was probably closer to 5.95. During each run, the average stagnation pressure and temperature from 0.05-s. intervals were calculated. The mass flux was then plotted with the square of the hot-wire voltage (Figure 3.7). A linear fit was used as a calibration and agreed well with the experimental values of mass flux. The calibration was appropriate for the mass-flux levels seen in the wake of the roughness, which were around 11 kg/s-m^2.

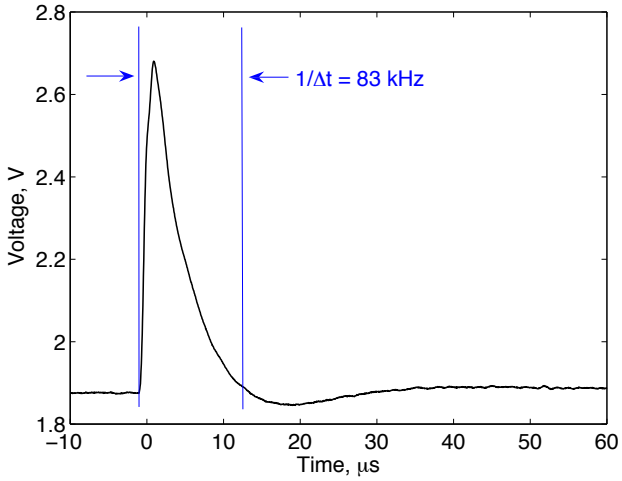

Figure 3.6. Time trace of hot wire response to square wave input. Hot wire was tuned to 83 kHz while installed in the tunnel with no flow.

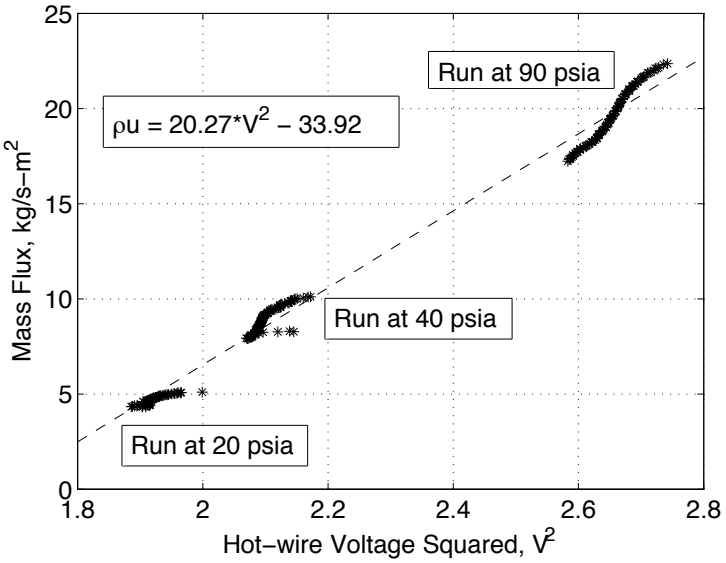

Figure 3.7. Hot wire calibration in the freestream of the BAM6QT. Three runs at different initial stagnation pressures. The stagnation temperature was assumed to drop isentropically with stagnation pressure during each run.

3.4 Kulite Pressure Transducers

Kulite pressure transducers are used to measure mean pressure as well as dynamic changes in pressure. The pressure transducer produces an electrical voltage output proportional to the amount of pressure applied to the sensor. The sensor consists of a small silicon diaphragm which is subjected to the measured pressure on one side and a reference pressure on the other side. A Wheatstone bridge of strain gauges are etched into the diaphragm and, based on the pressure being measured, the diaphragm deforms. The changing resistance of the strain gauges produces a voltage output that can be calibrated to pressure. Custom electronics are used to power and process the voltage output of the transducer. The custom Kulite electronics are made by John Philips, the department electronics technician. The DC voltage output is amplified with a gain of 100 using a Burr-Brown INA103 amplifier chip. An AC voltage output is provided by high-pass filtering the DC voltage at 840 Hz and amplifying again with a gain of 100. The Kulite electronic boxes are powered with Agilent E3620A dual-output power supplies.

In the BAM6QT, Kulite sensors are used in various places to record pressures. A flush-mounted Kulite model XTEL-190-200A is installed at the end of the driver tube, near the contraction. Because the Mach number in the driver tube is low, the pressure measured by the contraction Kulite is approximately equal to the stagnation pressure of the flow. Thus, the contraction Kulite provides a real-time measurement of the dropping stagnation pressure during a run. A second Kulite is installed in the diffuser section of the tunnel. As the burst diaphragms break and Mach-6 flow is established, the pressure measured by this Kulite drops by an order of magnitude. This rapid drop in signal is ideal for triggering tunnel electronics as the run begins. The diffuser Kulite signal is used to trigger the oscilloscopes, which then trigger the camera, traverse, and bleed-air valve.

A Kulite model XCQ-062-15A was used in a pitot probe to make dynamic measurements of disturbances in the thick nozzle-wall boundary layer. The sensor (serial

number 6217-2A-286) had a diameter of 1.68 mm (0.066 in.) and a range of approximately 0–15 psia. The sensor was designed with a mechanical stop at pressures greater than 15 psia. The mechanical stop protects the sensor from damage as the tunnel is filled to stagnation pressures prior to a run.

Though hot wire probes are the ideal instrument for making measurements of instability waves in a boundary layer, the use of a Kulite pitot probe offered several advantages. A Kulite is far less susceptible to breakage than a hot wire. A Kulite is also less sensitive to electronic noise than a hot wire, allowing the currently noisy stepper-motor traverse to be used without interference in the output signal. However, the Kulite cannot achieve as high a frequency response as a properly tuned hot wire. Because the nozzle-wall boundary layer is thicker than model boundary layers, the frequencies of instabilities should be smaller, and the frequency response of the Kulite may be sufficient.

In order to minimize the flow interference between the Kulite pitot sensor and the nozzle-wall boundary layer, a new probe was designed to hold the sensor. The pitot probe (Figure 3.8) utilizes a design similar to the hot-wire probes used in the BAM6QT. The probe consists of a body section with a 50.8-mm-(2-in.-)long knife-edged strut to hold the Kulite sensor. The 1.68-mm-diameter sensor is mounted in a 3.18-mm-(0.125-in.-)diameter tube. The upstream end of the tube was tapered to decrease interference. The Kulite was held in place using nail polish and the wire was taped to the back of the strut using high-temperature tape. Figure 3.9 shows a schematic of the pitot probe near the roughness and nozzle wall. Due to manufacturing difficulties, the sensor-mounting portion of the probe has an angle of 4.6° with respect to the expected flow direction. Figure 3.10 shows the probe near the tunnel wall, angled slightly away from the wall. The rounded leading edge of the probe is visible, as well as the Kulite sensor wire and high-temperature tape.

The Kulite pitot probe was calibrated at low pressures while installed in the tunnel. It was assumed that the pitot probe measures the stagnation pressure behind a normal shock. The stagnation pressure ratio behind a normal shock is 2.965% of

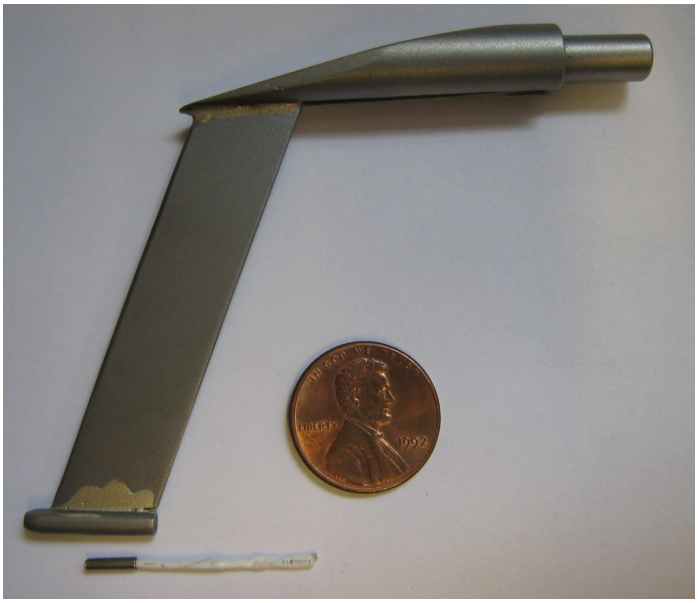

Figure 3.8. Kulite pitot probe with 2-in.-long strut, shown with sample Kulite pressure transducer.

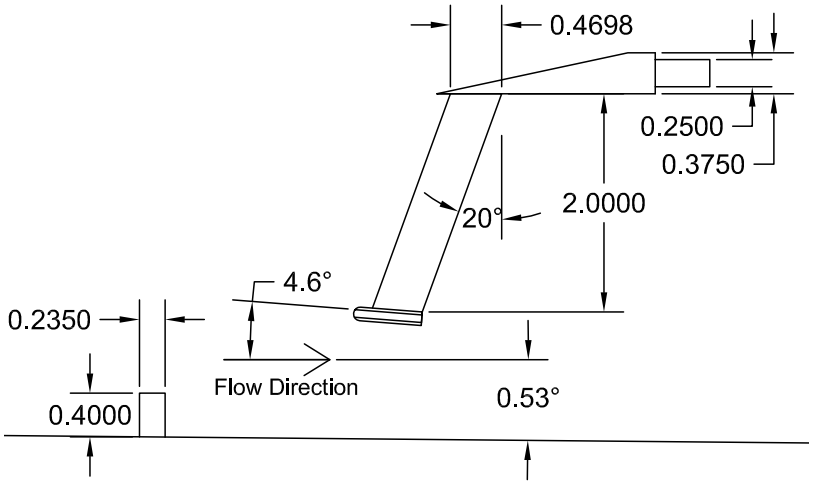

Figure 3.9. Drawing of Kulite pitot probe near the nozzle wall and roughness element (dimensions in inches, drawing to scale). The roughness element in the drawing is set to a height of 0.4 in. (10.2 mm) and the 0.53° nozzle-expansion angle at the roughness location is shown.

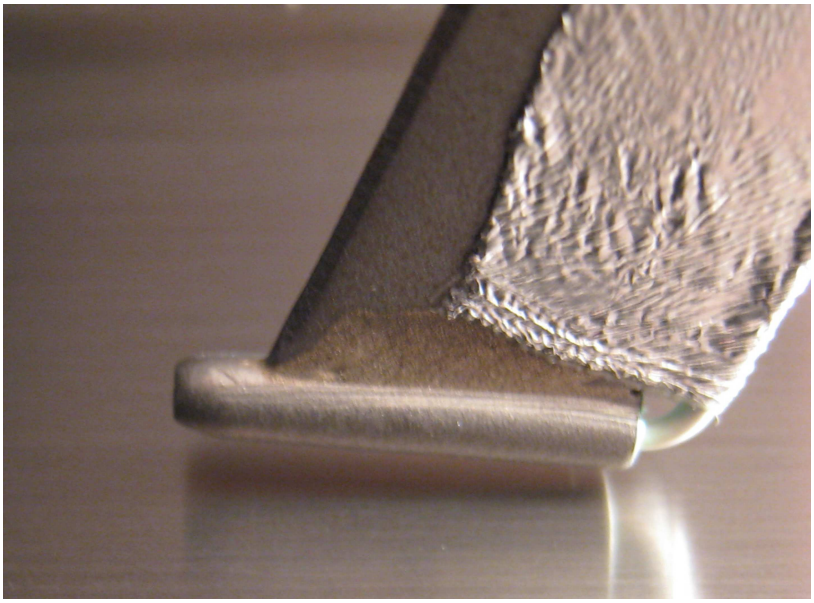

Figure 3.10. Close view of the Kulite probe near the tunnel wall.

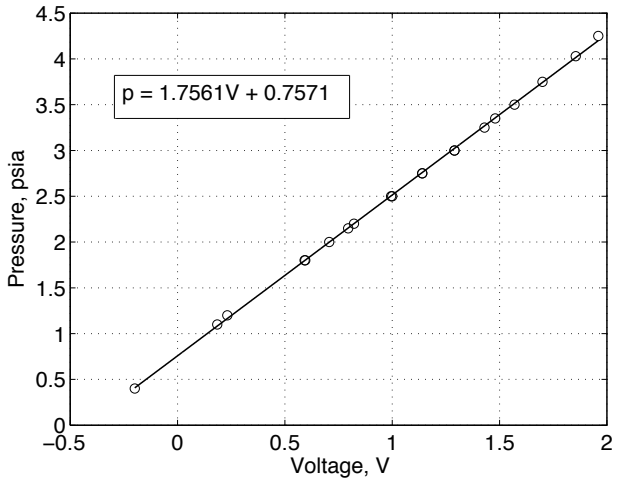

Figure 3.11. Calibration of pitot probe Kulite sensor.

the freestream stagnation pressure at Mach 6.0. The calibration was performed in the expected pitot-pressure measurement range of 0–4 psia. This range was expected at quiet-flow stagnation pressures less than 140 psia. After a run, air from the tunnel was allowed to leak slowly through the gate valve and into the vacuum tank. As the tunnel pressure decreased, the voltage outputs from the Kulite control box were recorded at various pressures using a digital multimeter. Pressures were taken from the Paroscientific Digiquartz 740-400A pressure display near the burst-diaphragm section. The Paroscientific transducer has a range of 0–400 psia with 0.01% accuracy. The data were fit to a linear curve and the resulting calibration (Figure 3.11) shows good agreement. The data points are represented by black circles and the curve-fit is represented by a solid black line.

3.5 Angled Probe Support

Both the hot-wire probes and the Kulite pitot probe attach to brass probe supports that hold the probe within the tunnel. The probe supports consist of a double-wedge strut with a 2×0.375 in. cross section. At the end of the strut, the probe is mounted in a 0.25-in.-diameter hole. Electrical connections to the hot-wire probe are made in a cylindrical nylon insert with two plugs and the wires are passed through a slot that has been machined into the side of the strut.

A new angled probe support (Figure 3.12) was designed and built to extend the measurement range of probes to upstream of the roughness element location. Previous probe supports used in the tunnel had a straight design when entering the nozzle. Because the traverse slot is located downstream of the roughness element, a probe attached to the straight probe support would only be able to measure approximately 0.2 m (8 in.) downstream of the roughness element. Figure 3.13 is a comparison of the measurement range of the straight probe support and the angled probe support, looking upstream through the nozzle. The roughness element is installed on the lower wall of the tunnel and the probe supports are positioned near their upstream

limits. The angled probe support is able to measure much farther upstream, up to approximately one inch upstream of the roughness element location. This range was desired to make measurements of instabilities within the incoming flow, ahead of the roughness. A drawing of the angled probe support appears in Appendix C.2.

3.6 Hot Films

A custom Senflex hot-film array from Tao of Systems, Inc. (Figure 3.14) is installed on the wall of the nozzle in one of the small window blanks. During each run, the outputs of selected hot films are monitored to determine if the boundary layer on the nozzle wall is laminar or turbulent. The array is 9×3 in. and contains sensors at 35 axial locations, numbered 1–35 and spaced at 0.25-in. intervals. Hot film #4, a commonly-used sensor, is located at tunnel coordinate $z = 74.25$ in. [58]. At three axial locations, there are two additional sensors ±2 in. off the centerline of the array. Paste-on hot films from Dantec Dynamics (model 55R47) can also be used on models or on the tunnel wall. The paste-on hot film is flush-mounted to a surface and oriented perpendicular to the flow direction. The 50-μm-thick sensor is 0.9×0.1 mm and is connected to gold-plated leads.

The hot films are controlled using Bruhn-5 constant temperature anemometers built at Purdue. A dial on the front of each CTA sets the balance resistance on the Wheatstone bridge circuit, although the dial actually indicates half the value of the balance resistance. The current through each hot film should be limited to about 100 mA corresponding to an overheat ratio of 1.3 [59]. Two outputs are available: DC-coupled and DC Fluctuation (DCF). The DCF output can be offset using a trimpot and is typically set to 0±100 mV prior to each run to ensure good resolution on the oscilloscopes. The output of the anemometers is not calibrated and is used for qualitative purposes to determine if the flow is noisy, quiet, or if the tunnel has not started. In addition, the time at which the run ends can be determined from the hot film traces.

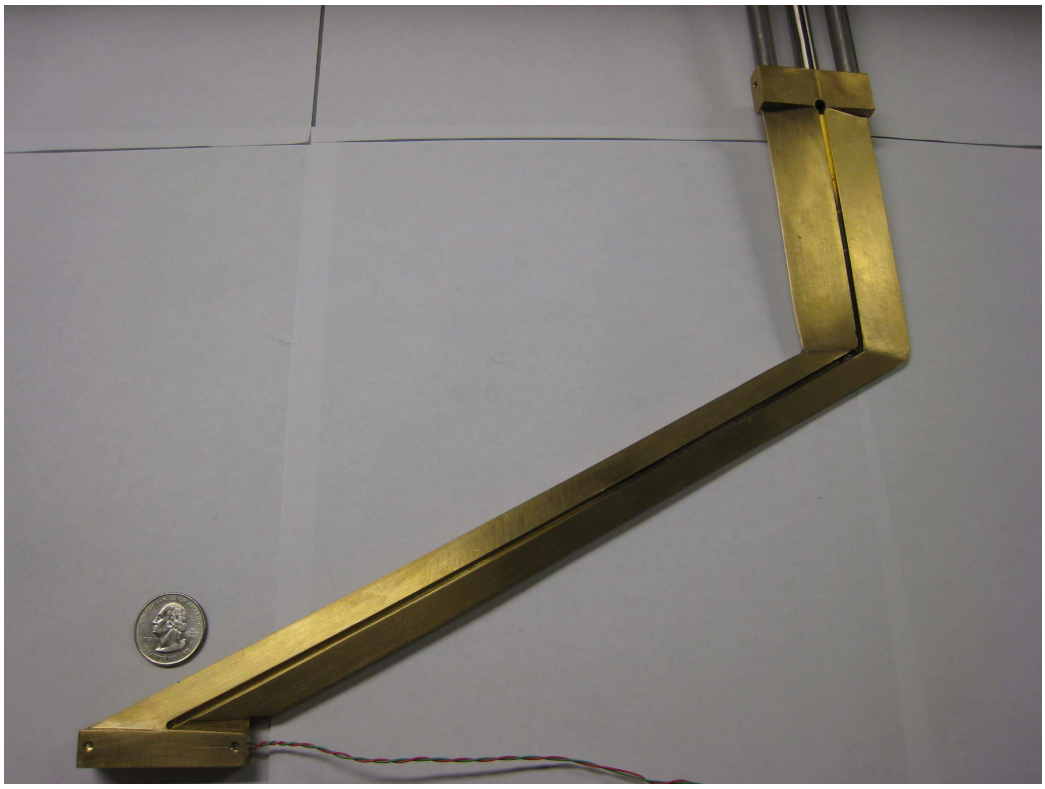

Figure 3.12. Angled probe support, for use with hot-wire probes or Kulite probe.

(a) Straight. (b) Angled.

Figure 3.13. Comparison of streamwise measurement range of straight and angled probe support.

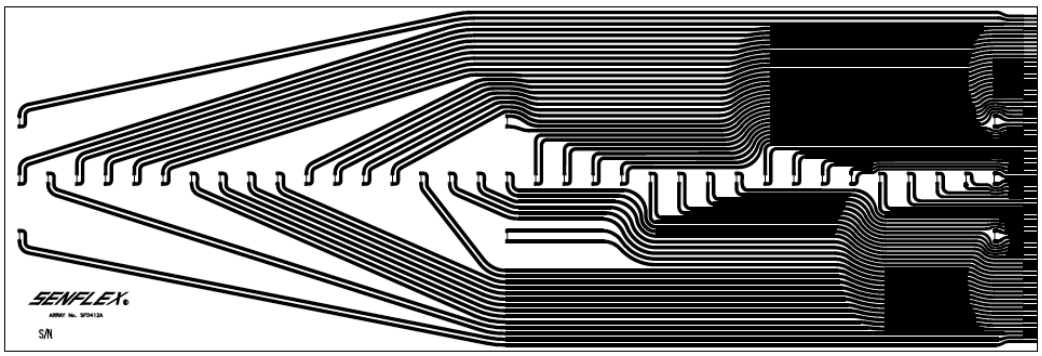

Figure 3.14. Senflex hot-film array.

3.7 Tektronix Oscilloscopes

Data acquisition in the BAM6QT is performed using Tektronix TDS7104 and DPO7054 Digital Phosphor Oscilloscopes. Both oscilloscopes feature four channels that can record AC and DC signals. The DPO7054 has a record length of 50 megabytes per channel compared to the 4 megabytes per channel of the TDS7104. Because the DPO7054 had a longer record length, the pitot and hot-wire probe signals were recorded on that oscilloscope at high sampling frequencies. The sampling frequency for probe data was 2.0 MHz. Additional details of the signal acquisition and processing methods for the probe data appears in Appendix A. Other traces such as the contraction pressure and wall hot-films were recorded on the TDS7104 oscilloscope at a lower sampling frequency of 200 kHz. Both oscilloscopes were operated in Hi-Res mode, which acquires data at the maximum sampling frequency and averages the points in real-time to the desired sampling frequency. This averaging results in decreased noise and greater vertical resolution, which are important for measurements of instabilities.

4. TEMPERATURE-SENSITIVE PAINT MEASUREMENTS

Temperature-sensitive paint images of the wake of the isolated roughness element were obtained to provide an understanding of the flow behind the roughness element. In the images, flow is from left to right. The images were taken at initial tunnel stagnation pressures $p_{0,i} = 90$ and 120 psia, and an initial stagnation temperature of 433 K, for various roughness heights k. Temperatures were calculated from the TSP calibration of the ratio of flow-on intensity to flow-off intensity. The freestream Reynolds number Re_∞ was calculated using the instantaneous stagnation pressure and assuming an isentropic decrease in stagnation temperature (Appendix B.5). A summary of the test conditions for each figure appears in Appendix D.

Air bubbles from underneath the PVC insulator appear in the images as dark blue marks. The bubble heights of approximately 0.25 mm (0.01 in.) were relatively small compared to the boundary layer thickness (roughly 3%). Because the density near the wall in a Mach-6 boundary layer is low, the bubbles should not have affected the flow. Two layers and three layers of plastic insulator were applied on rectangular patches at the downstream end of the window blank, off the centerline, as part of a separate TSP sensitivity experiment.

The boundary-layer thickness δ was calculated using computations at $p_0 = 130$ psia and scaled to the actual stagnation pressure using the square root of the freestream Reynolds number (see Equation 2 in Reference 60). The computations were obtained using the Harris boundary-layer code and the Sivells nozzle design code [44]. The boundary-layer thickness δ was found using the equation

$$\delta\sqrt{Re_\infty} = \delta_{130}\sqrt{Re_{\infty,130}} \tag{4.1}$$

where δ_{130} and $Re_{\infty,130}$ were the boundary-layer thickness and freestream Reynolds number at $p_0 = 130$ psia. In the computations, δ_{130} was the height above the wall at which the velocity is 99.95% of its freestream value. The boundary-layer height at 130 psia stagnation pressure (δ_{130}) was computed to be 7.29 mm (0.287 in.).

The temperature-sensitive paint results were obtained in February 2008 [29], during which time no inserts were installed in the sting-support section. The 45° expansion from the end of the nozzle to the sting-support section remained. During the experiments, a 100-Hz oscillation could be seen on the nozzle-wall hot films, including during the entire run at $p_{0,i} = 135$–140 psia. The oscillations appeared only during the first second of the runs beginning at $p_{0,i} = 120$ psia and only during the first 0.5 s of the runs at $p_{0,i} = 90$ psia. The oscillations were likely an unsteady disturbance from the 45° expansion, caused by the startup process, that propagated upstream into the nozzle (see section IV.A of Reference 46). The images shown are from time periods during the run when the hot films indicated normal quiet flow or normal noisy flow and the oscillations were not present.

4.1 Laminar vs. Turbulent Boundary Layer Images

The effect of a laminar and turbulent nozzle-wall boundary layer on the wake of the roughness element is shown in Figure 4.1. Two images are shown with a roughness height of 2.54 mm (0.10 in.) at similar stagnation pressure. In these images, $\frac{k}{\delta}$ was approximately 0.32 for the laminar boundary layer. In the first image, the nozzle wall boundary layer is turbulent, corresponding to noisy flow. In the second image, the nozzle wall boundary layer is laminar, corresponding to quiet flow. Both images were from runs with $p_{0,i} = 120$ psia.

The flow field behind the roughness element is quite different depending on the condition of the nozzle wall boundary layer. During noisy flow, the incoming boundary layer is turbulent and the wake is much wider than in quiet flow. In addition, the heating is higher overall within the wake. When the incoming boundary layer is

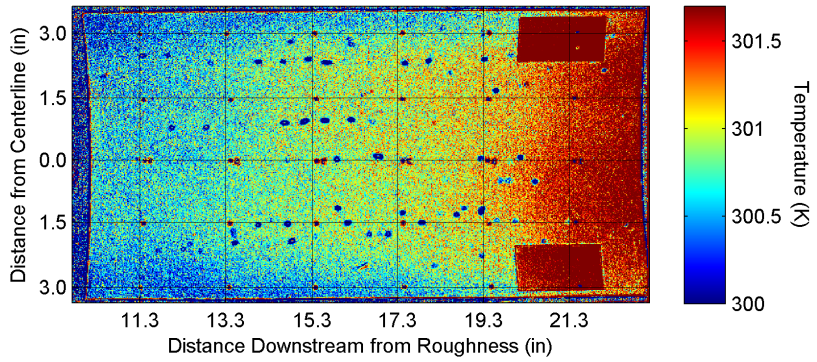

(a) Noisy flow, $p_0 = 109.9$ psia, $Re_\infty = 2.77 \times 10^6$/ft.

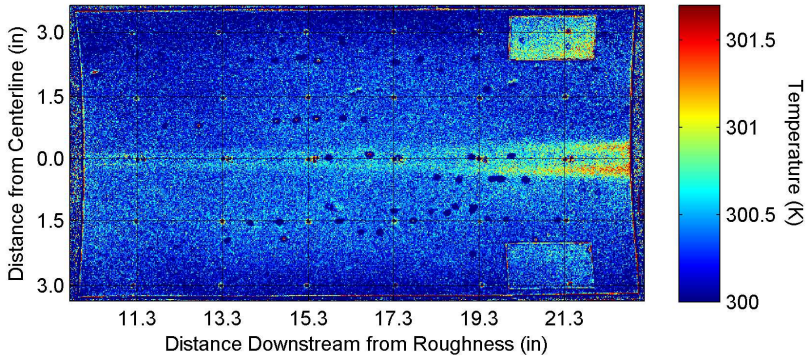

(b) Quiet flow, $p_0 = 107.9$ psia, $Re_\infty = 2.55 \times 10^6$/ft.

Figure 4.1. Roughness wake temperatures when $p_{0,i} = 120$ psia, $k = 2.5$ mm (0.10 in.), and $\frac{k}{\delta} \approx 0.32$. Noisy vs. quiet flow at $t = 1.5$ s.

laminar the wake of the roughness is visible as two thin streaks which spread as they progress downstream. The structured wake of the roughness within the laminar boundary layer (Figure 4.1(b)) is the primary focus of these experiments, and thus a laminar boundary layer on the nozzle wall is desired. Experiments in a laminar nozzle wall boundary layer cannot be carried out except under quiet conditions in the BAM6QT. Under noisy conditions, the nozzle wall boundary layer at the roughness location is always turbulent.

4.2 Roughness Height Effects on a Laminar Boundary Layer

The effect of increasing roughness height on wake temperatures in a laminar boundary layer was explored and results are shown in Figures 4.2 through 4.11. The first set of figures show four TSP images from the same run, in chronological order. The second set of figures show spanwise temperatures at four downstream locations within the wake. The spanwise temperature data were taken from the TSP images, and were from an average area of 3 spanwise pixels by 30 streamwise pixels (0.055×0.55 in.), to reduce noise. All images are from runs with an initial tunnel stagnation pressure of $p_{0,i} = 120$ psia. As the run progresses, the tunnel stagnation pressure decreases, the unit Reynolds number decreases, and the boundary layer thickness increases. As the boundary layer thickness increases, the roughness appears smaller to the flow and the wake behind the roughness may change. All runs were quiet with bleed suction on, and all four images in each figure were taken during the quiet portion of a single run.

Figures 4.2 and 4.3 show images and temperature data with a roughness height of 4.6 mm (0.18 in.), corresponding to $\frac{k}{\delta} \approx 0.59 - 0.58$. The images show a long, thin streak of a higher temperature wake region behind the roughness element. Farther downstream, the higher temperature region spreads, and individual peaks in temperature can be seen within the wake. As the run progresses, the temperature of the wake region decreases slightly. The decrease in temperature could be due to decreased heat transfer from the thickening boundary layer as the run progresses or could be an artifact of the falling stagnation temperature in the tunnel as the stagnation pressure falls.

Figures 4.4 and 4.5 show images and temperature data when k is increased to 6.6 mm (0.26 in.). In these images, $\frac{k}{\delta}$ decreases from 0.86 to 0.84 during the run. The high temperature wake region is more pronounced for the higher roughness. The wake is still centered behind the roughness element but is much wider. Two-to-six hot streaks are visible during the run. As the run progresses, the temperatures

in the wake change. The first photo shows many hot streaks and a larger spreading angle. Eventually, the number of hot streaks decreases to four and the outside streaks develop farther downstream than the inside streaks. The images in Figure 4.4 show the only run where the structure of the wake region changes dramatically between images, so perhaps these conditions are important to understanding the physics of the roughness wake.

In Figures 4.6 and 4.7, the roughness height was increased to 8.1 mm (0.32 in.), slightly larger than the boundary-layer height ($\frac{k}{\delta} \approx 1.05 - 1.03$). The photos show that the wake region is now wider and seems to remain wide throughout the run, though temperatures decrease during the run. Possible hot streaks are visible in the wake region, but the noise in these images is high. The overall temperatures in the wake are lower than in the $k = 6.6$ mm case.

Figures 4.8 and 4.9 show images and wake temperatures when $k = 10.2$ mm (0.40 in.) and $\frac{k}{\delta} \approx 1.31 - 1.28$. The roughness height now exceeds the boundary layer thickness by a significant margin. Possible hot streaks are still visible at this roughness height, but are difficult to see due to noise. During this run, the wake begins to encroach on the regions with double and triple layers of insulator. The thicker insulator layer decreases the heat transfer to the nozzle wall, resulting in higher temperatures.

Figures 4.10 and 4.11 show the case of a roughness height of 19.3 mm (0.76 in.) and $\frac{k}{\delta} \approx 2.49 - 2.43$, which is well outside of the boundary layer. Again, this run was quiet with a laminar boundary layer on the nozzle wall. A wide wake region is visible in the images, with thick hot streaks that decrease in temperature as the run progresses.

Figures 4.2 through 4.11 show consistent trends as the roughness height is increased and the boundary-layer height is not significantly changed. The high-temperature wake region widens as the roughness height is increased, even when the roughness height is significantly higher than the boundary-layer thickness. In addition, all images from roughness heights higher than 4.6 mm (0.18 in.) show several hot streaks

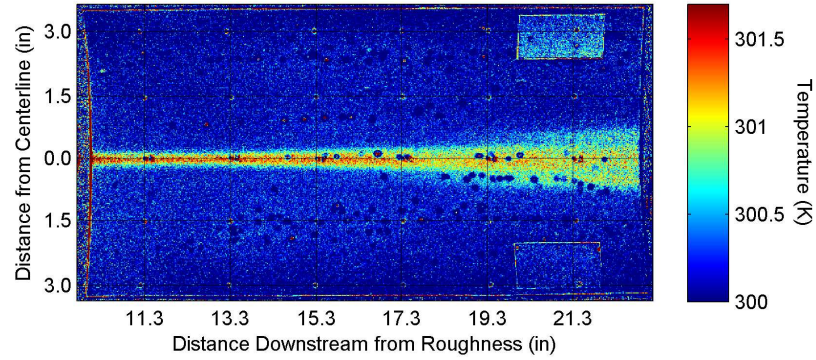

(a) $t = 1.52$ s, $p_0 = 108.3$ psia, $Re_\infty = 2.56 \times 10^6$/ft.

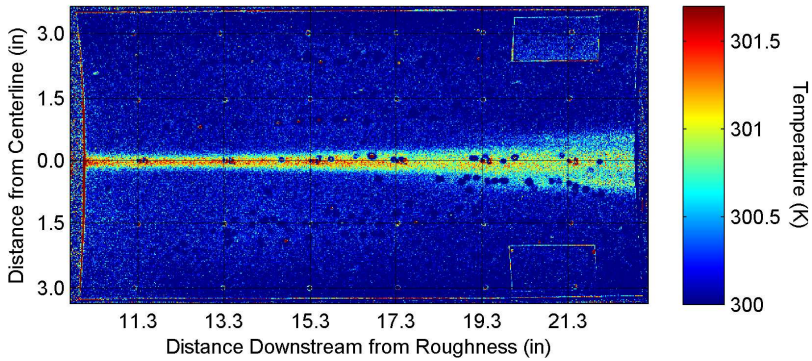

(b) $t = 1.98$ s, $p_0 = 105.6$ psia, $Re_\infty = 2.53 \times 10^6$/ft.

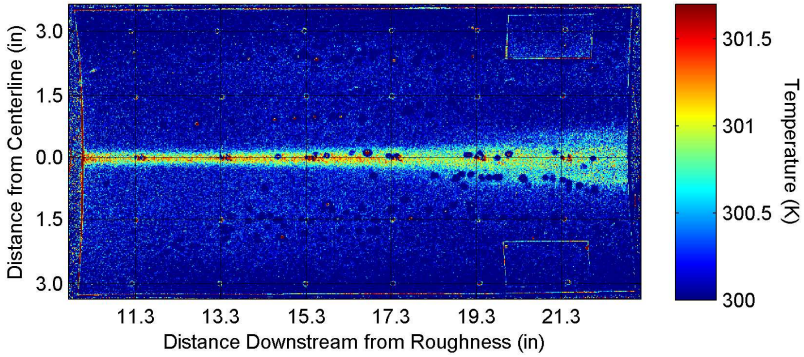

(c) $t = 2.44$ s, $p_0 = 101.7$ psia, $Re_\infty = 2.49 \times 10^6$/ft.

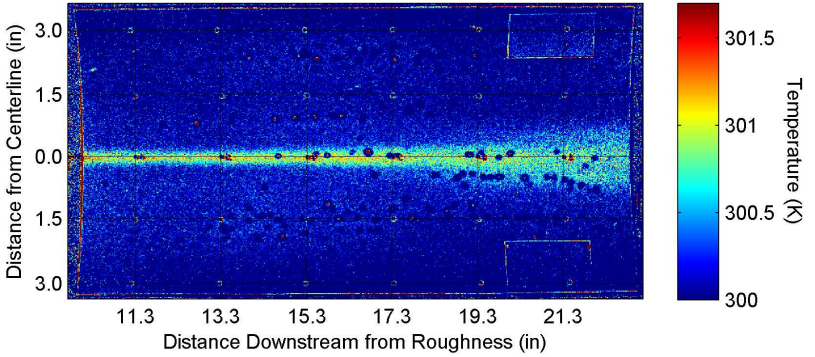

(d) $t = 2.90$ s, $p_0 = 99.3$ psia, $Re_\infty = 2.46 \times 10^6$/ft.

Figure 4.2. Roughness wake temperatures when $p_{0,i} = 120$ psia, $k = 4.6$ mm ($\frac{k}{\delta} \approx 0.59 - 0.58$). Quiet flow.

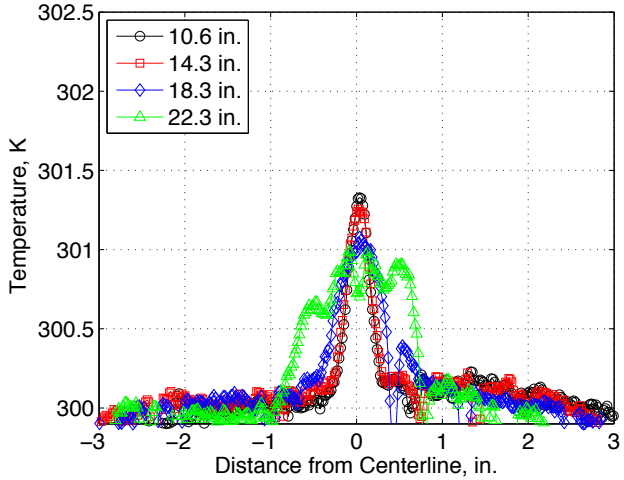

(a) $t = 1.52$ s, $p_0 = 108.3$ psia, $Re_\infty = 2.56 \times 10^6$/ft.

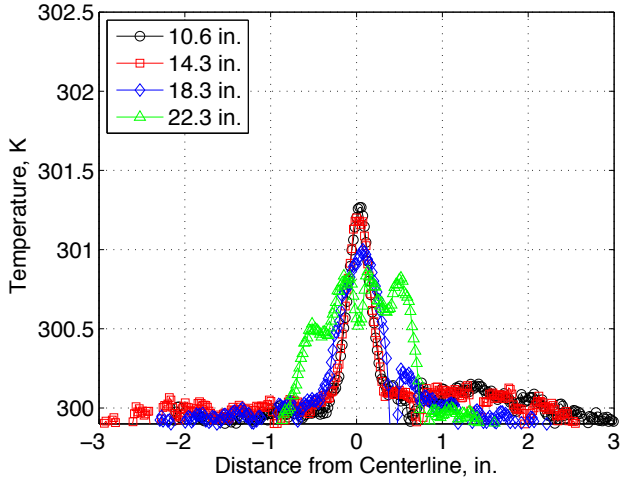

(b) $t = 1.98$ s, $p_0 = 105.6$ psia, $Re_\infty = 2.53 \times 10^6$/ft.

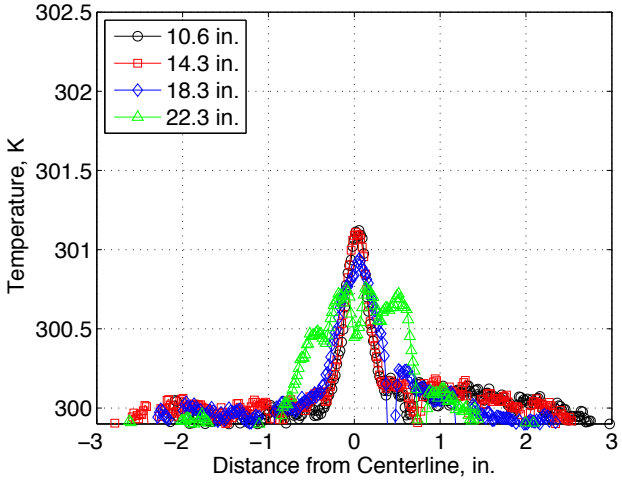

(c) $t = 2.44$ s, $p_0 = 101.7$ psia, $Re_\infty = 2.49 \times 10^6$/ft.

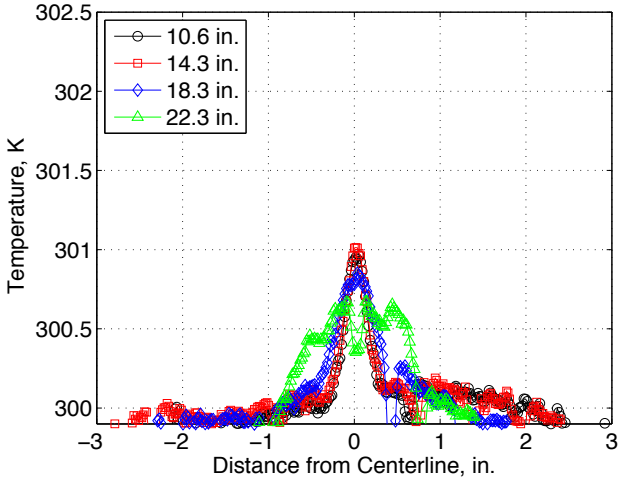

(d) $t = 2.90$ s, $p_0 = 99.3$ psia, $Re_\infty = 2.46 \times 10^6$/ft.

Figure 4.3. Spanwise wake temperatures from Figure 4.2, looking downstream. Legend indicates distance downstream from the roughness.

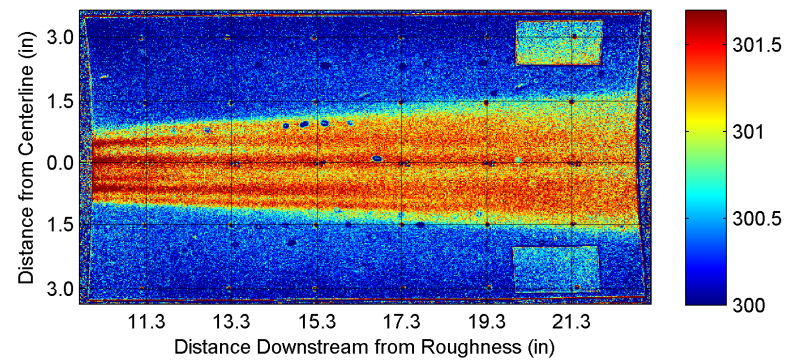

(a) $t = 1.07$ s, $p_0 = 115.6$ psia, $Re_\infty = 2.64 \times 10^6$/ft.

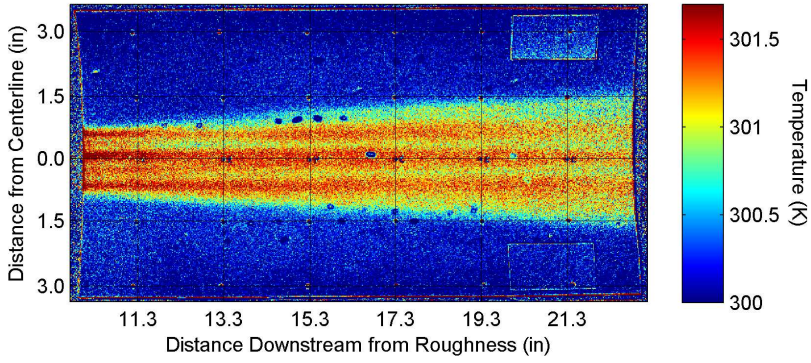

(b) $t = 1.53$ s, $p_0 = 111.1$ psia, $Re_\infty = 2.59 \times 10^6$/ft.

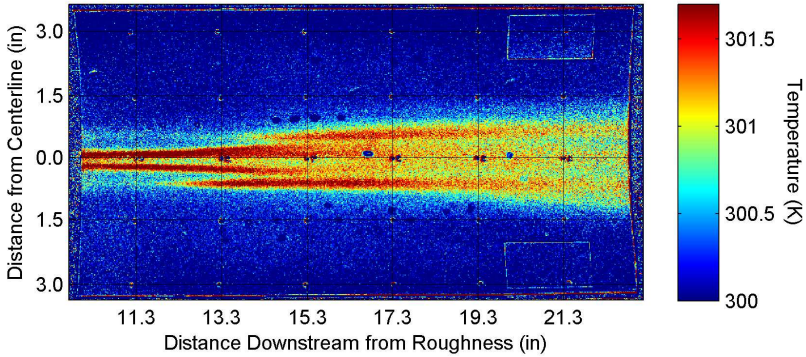

(c) $t = 2.00$ s, $p_0 = 108.5$ psia, $Re_\infty = 2.56 \times 10^6$/ft.

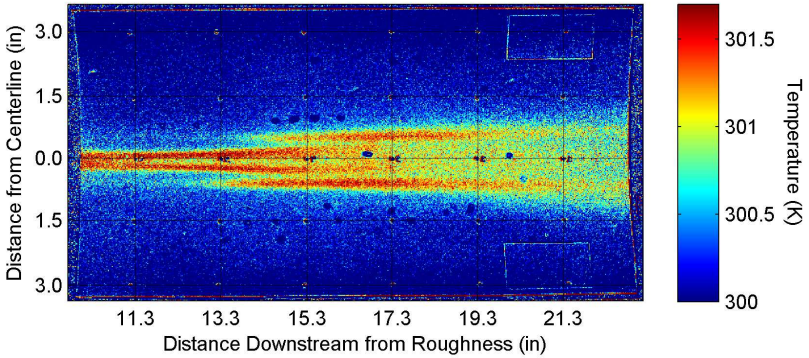

(d) $t = 2.46$ s, $p_0 = 104.4$ psia, $Re_\infty = 2.52 \times 10^6$/ft.

Figure 4.4. Roughness wake temperatures when $p_{0,i} = 120$ psia, $k = 6.6$ mm ($\frac{k}{\delta} \approx 0.86 - 0.84$). Quiet flow.

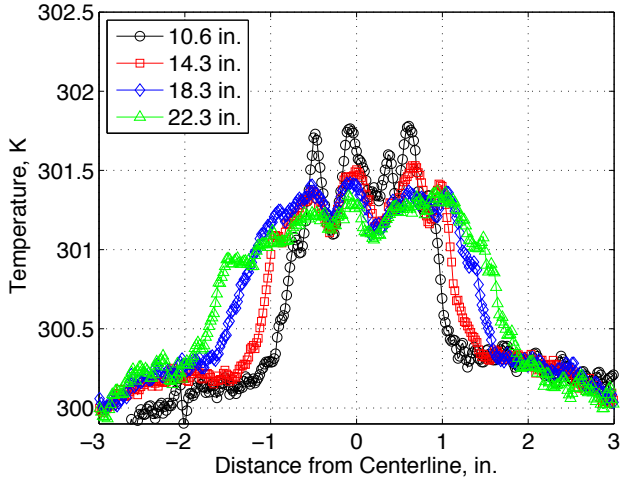

(a) $t = 1.07$ s, $p_0 = 115.6$ psia, $Re_\infty = 2.64 \times 10^6$/ft.

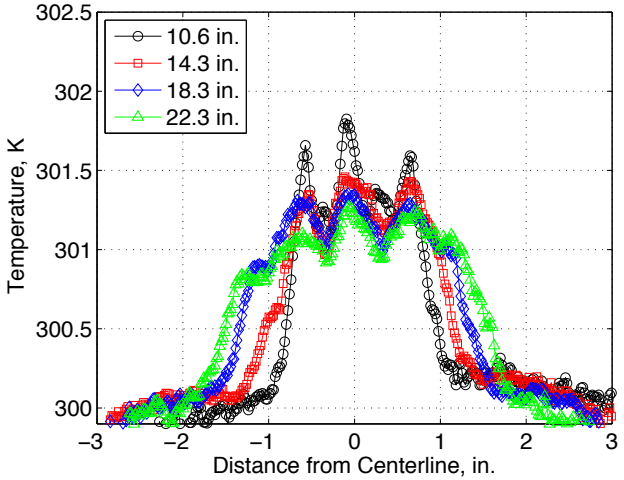

(b) $t = 1.53$ s, $p_0 = 111.1$ psia, $Re_\infty = 2.59 \times 10^6$/ft.

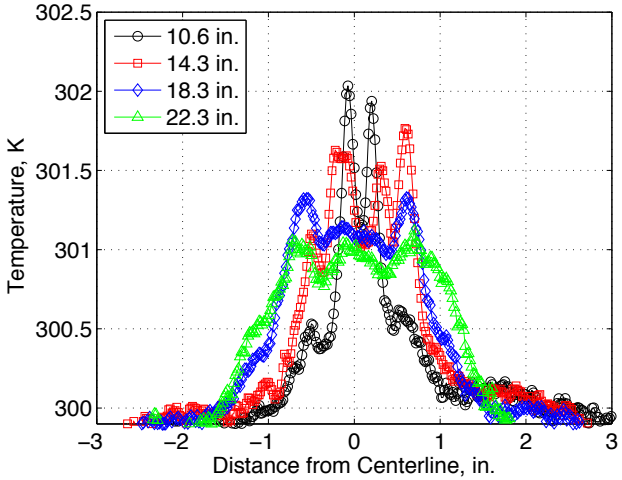

(c) $t = 2.00$ s, $p_0 = 108.5$ psia, $Re_\infty = 2.56 \times 10^6$/ft.

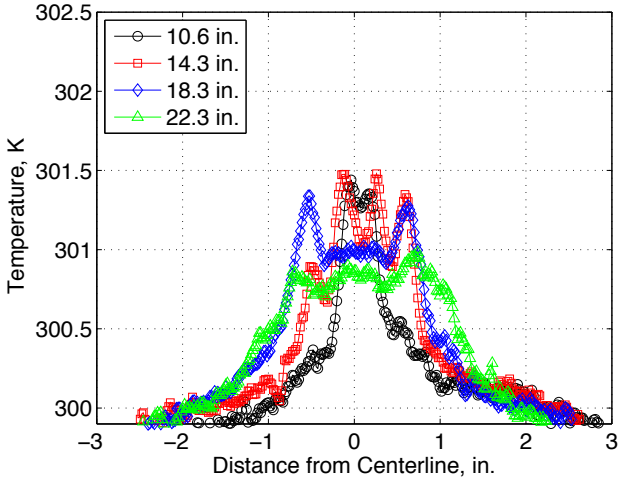

(d) $t = 2.46$ s, $p_0 = 104.4$ psia, $Re_\infty = 2.52 \times 10^6$/ft.

Figure 4.5. Spanwise wake temperatures from Figure 4.4, looking downstream. Legend indicates distance downstream from the roughness.

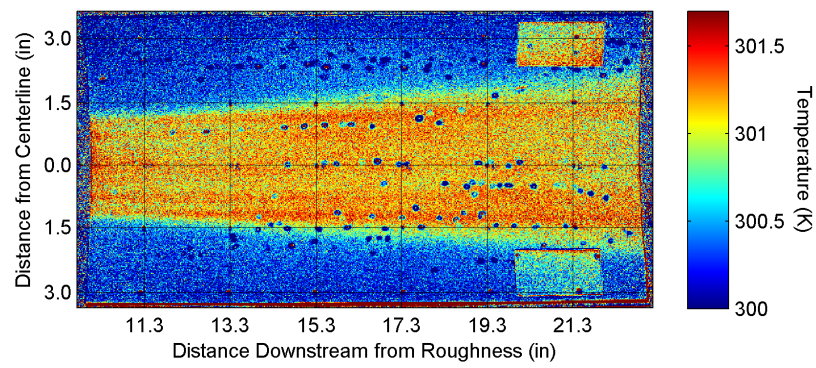

(a) $t = 1.05$ s, $p_0 = 112.3$ psia, $Re_\infty = 2.61 \times 10^6$/ft.

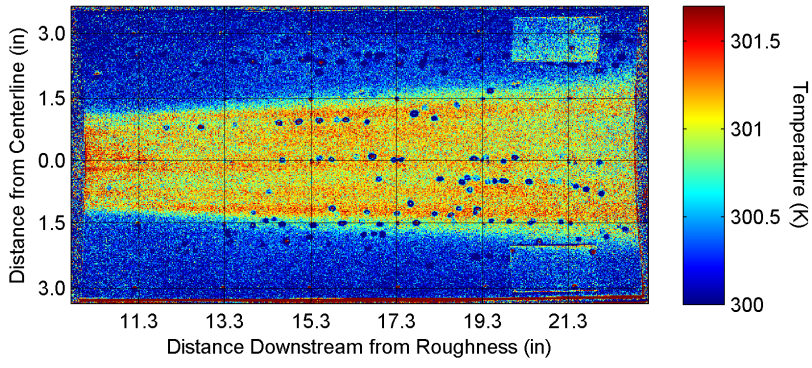

(b) $t = 1.50$ s, $p_0 = 108.0$ psia, $Re_\infty = 2.56 \times 10^6$/ft.

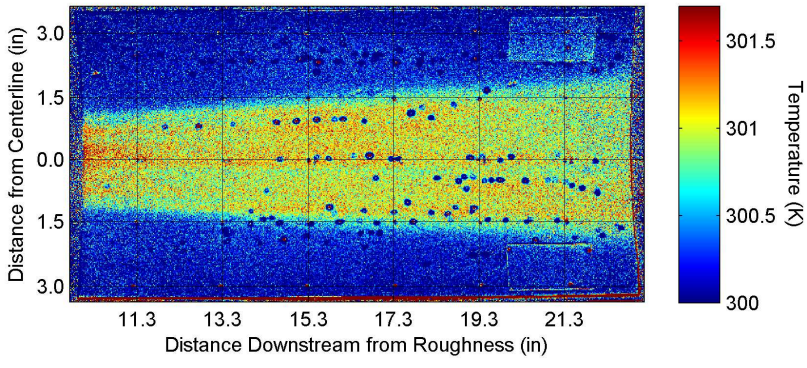

(c) $t = 1.96$ s, $p_0 = 105.3$ psia, $Re_\infty = 2.53 \times 10^6$/ft.

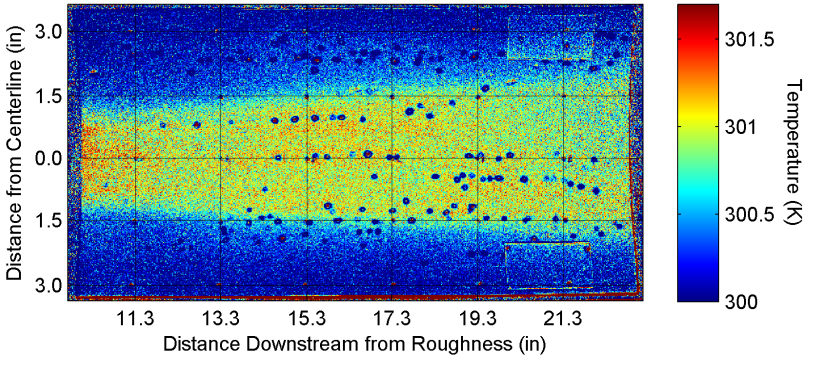

(d) $t = 2.41$ s, $p_0 = 101.4$ psia, $Re_\infty = 2.48 \times 10^6$/ft.

Figure 4.6. Roughness wake temperatures when $p_{0,i} = 120$ psia, $k = 8.1$ mm ($\frac{k}{\delta} \approx 1.05 - 1.03$). Quiet flow.

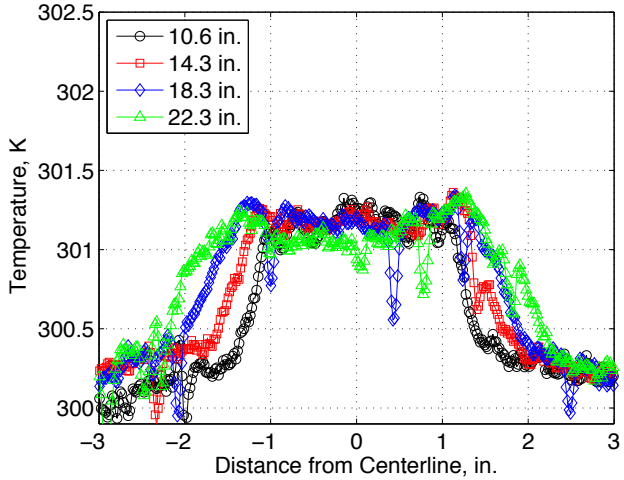

(a) $t = 1.05$ s, $p_0 = 112.3$ psia, $Re_\infty = 2.61 \times 10^6$/ft.

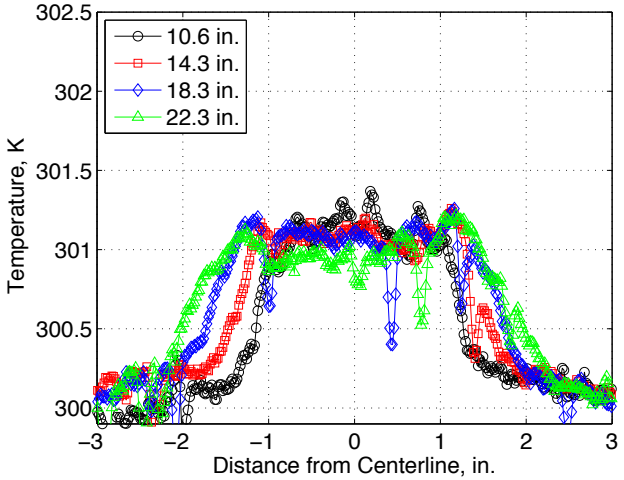

(b) $t = 1.50$ s, $p_0 = 108.0$ psia, $Re_\infty = 2.56 \times 10^6$/ft.

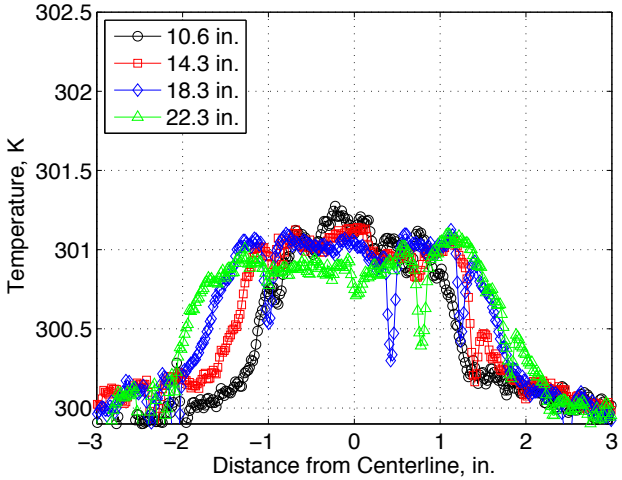

(c) $t = 1.96$ s, $p_0 = 105.3$ psia, $Re_\infty = 2.53 \times 10^6$/ft.

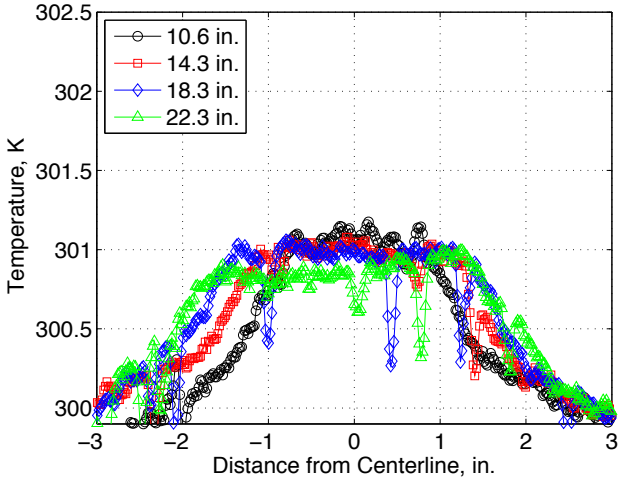

(d) $t = 2.41$ s, $p_0 = 101.4$ psia, $Re_\infty = 2.48 \times 10^6$/ft.

Figure 4.7. Spanwise wake temperatures from Figure 4.6, looking downstream. Legend indicates distance downstream from the roughness.

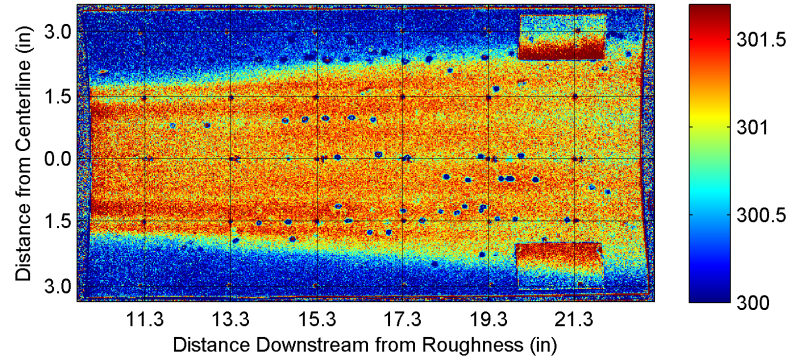

(a) $t = 1.51$ s, $p_0 = 108.4$ psia, $Re_\infty = 2.56 \times 10^6$/ft.

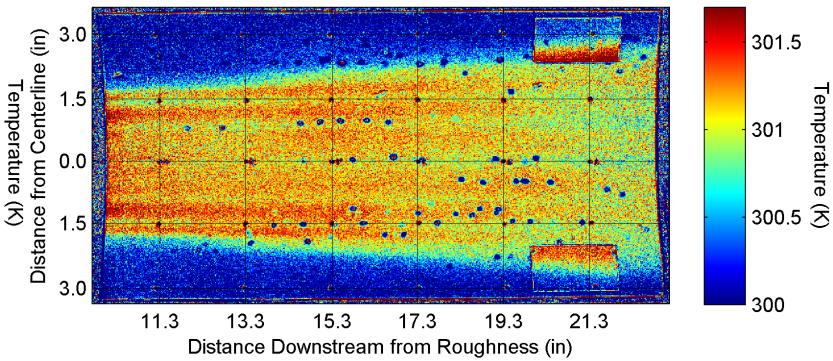

(b) $t = 1.97$ s, $p_0 = 105.8$ psia, $Re_\infty = 2.53 \times 10^6$/ft.

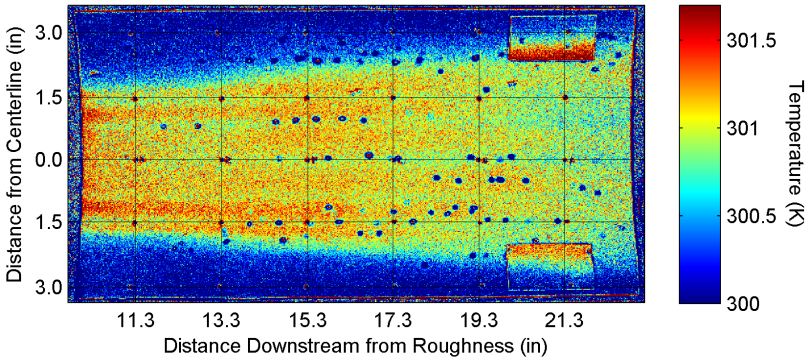

(c) $t = 2.43$ s, $p_0 = 101.8$ psia, $Re_\infty = 2.49 \times 10^6$/ft.

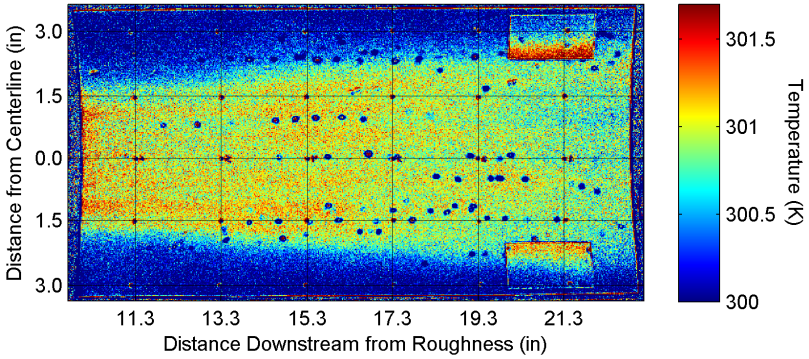

(d) $t = 2.88$ s, $p_0 = 99.4$ psia, $Re_\infty = 2.46 \times 10^6$/ft.

Figure 4.8. Roughness wake temperatures when $p_{0,i} = 120$ psia, $k = 10.2$ mm ($\frac{k}{\delta} \approx 1.31 - 1.28$). Quiet flow.

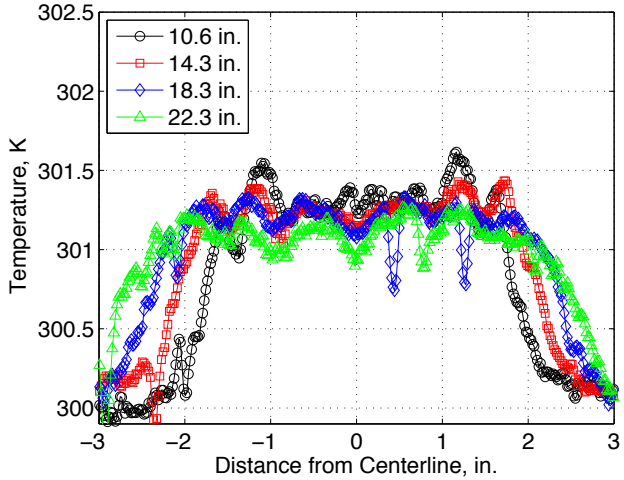

(a) $t = 1.51$ s, $p_0 = 108.4$ psia, $Re_\infty = 2.56 \times 10^6$/ft.

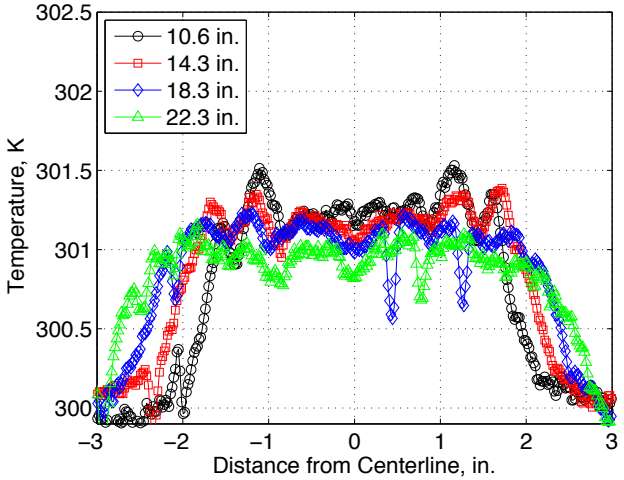

(b) $t = 1.97$ s, $p_0 = 105.8$ psia, $Re_\infty = 2.53 \times 10^6$/ft.

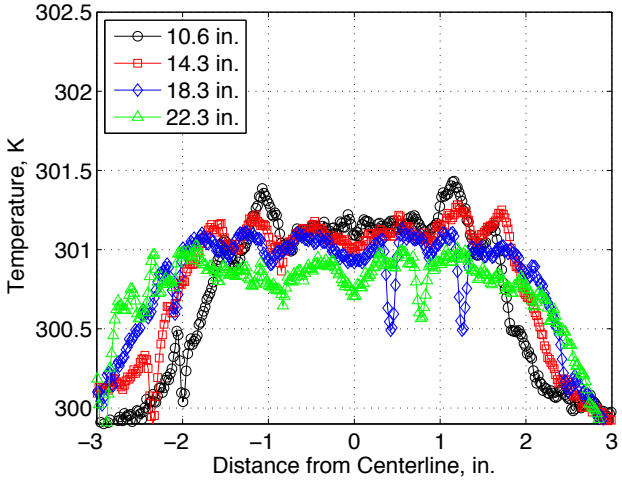

(c) $t = 2.43$ s, $p_0 = 101.8$ psia, $Re_\infty = 2.49 \times 10^6$/ft.

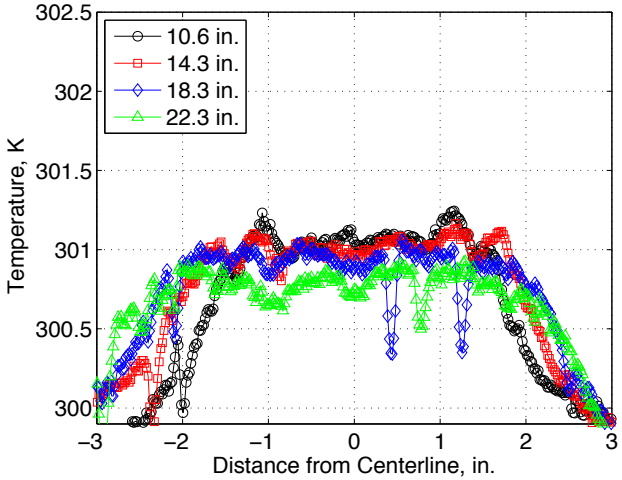

(d) $t = 2.88$ s, $p_0 = 99.4$ psia, $Re_\infty = 2.46 \times 10^6$/ft.

Figure 4.9. Spanwise wake temperatures from Figure 4.8, looking downstream. Legend indicates distance downstream from the roughness.

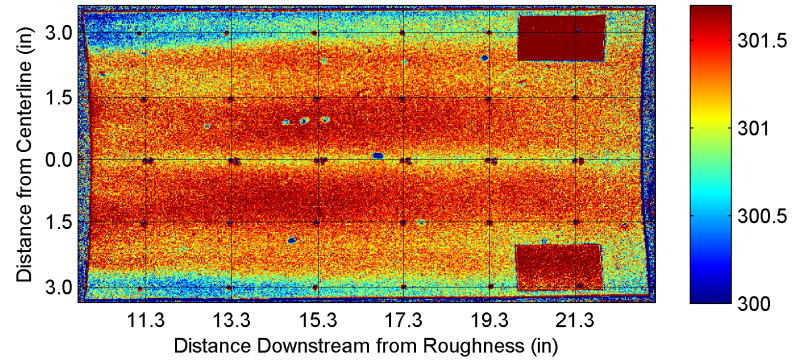

(a) $t = 1.52$ s, $p_0 = 108.7$ psia, $Re_\infty = 2.57 \times 10^6$/ft.

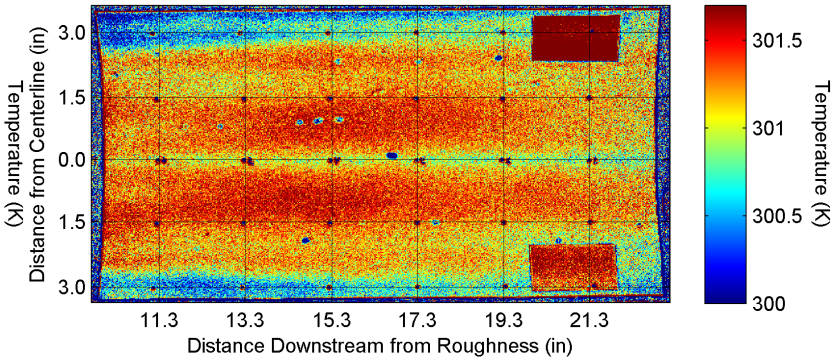

(b) $t = 1.98$ s, $p_0 = 105.9$ psia, $Re_\infty = 2.53 \times 10^6$/ft.

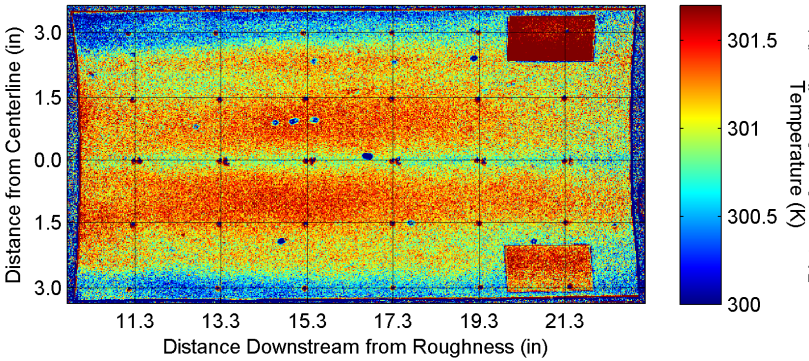

(c) $t = 2.45$ s, $p_0 = 102.0$ psia, $Re_\infty = 2.49 \times 10^6$/ft.

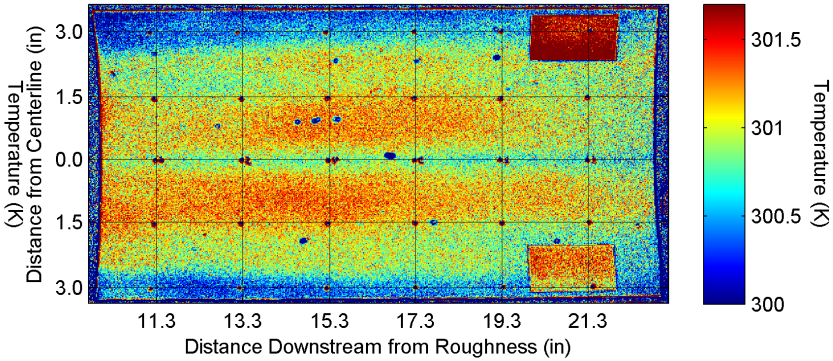

(d) $t = 2.91$ s, $p_0 = 99.3$ psia, $Re_\infty = 2.43 \times 10^6$/ft.

Figure 4.10. Roughness wake temperatures when $p_{0,i} = 120$ psia, $k = 19.3$ mm ($\frac{k}{\delta} \approx 2.49 - 2.43$). Quiet flow.

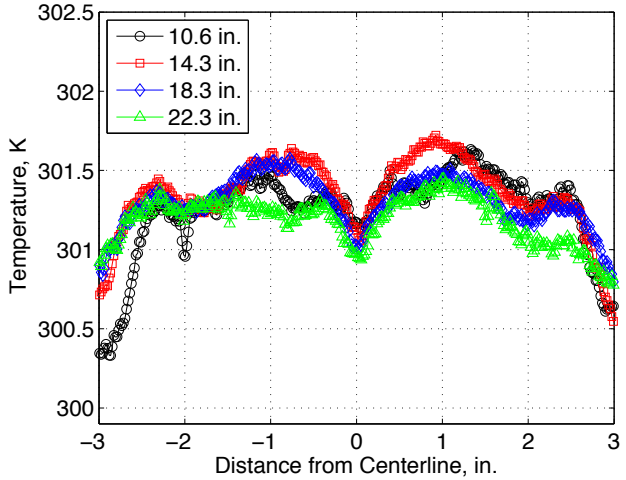

(a) $t = 1.52$ s, $p_0 = 108.7$ psia, $Re_\infty = 2.57 \times 10^6$/ft.

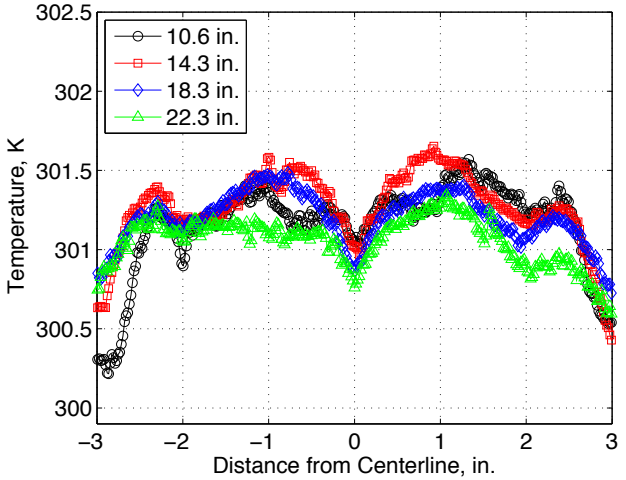

(b) $t = 1.98$ s, $p_0 = 105.9$ psia, $Re_\infty = 2.53 \times 10^6$/ft.

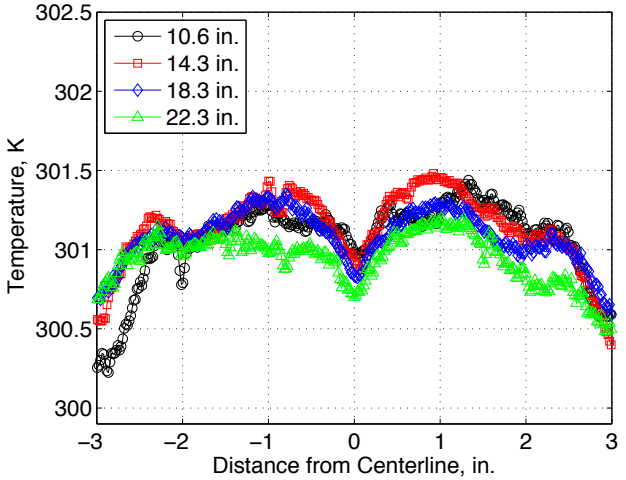

(c) $t = 2.45$ s, $p_0 = 102.0$ psia, $Re_\infty = 2.49 \times 10^6$/ft.

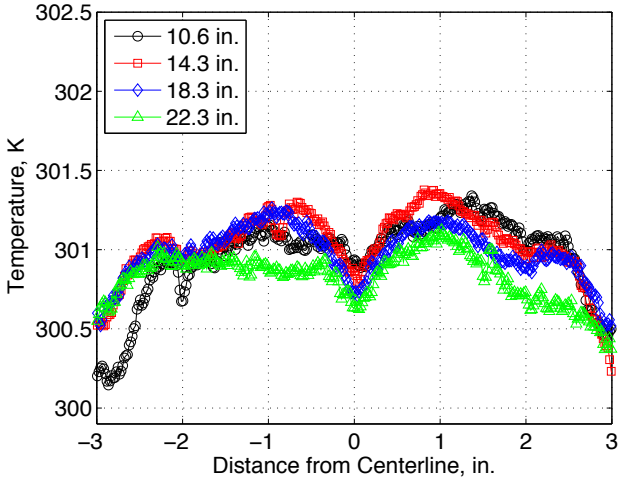

(d) $t = 2.91$ s, $p_0 = 99.3$ psia, $Re_\infty = 2.43 \times 10^6$/ft.

Figure 4.11. Spanwise wake temperatures from Figure 4.10, looking downstream. Legend indicates distance downstream from the roughness.

which may be the vortices seen in Whitehead [33], or maybe instabilities. These hot streaks may be present in Figure 4.2, but the wake region may be too thin for them to be visible in the TSP images.

4.3 Wake Similarity

Two similar wake regions were observed between two runs at different conditions. Figure 4.12(a) shows wake temperatures from a run with an initial stagnation pressure of 120 psia and a roughness height of 10.2 mm (0.40 in.). Figure 4.12(b) shows wake temperatures from a run with $p_{0,i} = 90$ psia and a roughness height of 12.7 mm (0.50 in.). Line plots of the wake temperatures at various downstream positions are shown in Figure 4.13. In the first image the roughness height was roughly 1.3 times the boundary layer height, while in the second image the roughness height was 1.4 times the boundary layer height. Though the two runs were at different stagnation pressures and different roughness heights, the wake regions are similar. Both images show four to six hot streaks with the hottest streaks near 1.4 in. off the centerline of the roughness. In addition, the regions of high temperatures within the two wakes are similarly sized with the wake in Figure 4.12(b) slightly larger. The two cases are dissimilar in that the lower stagnation-pressure case has decreasing temperatures in the downstream portion of the wake. It is possible that the wake of the roughness element on the nozzle wall could scale to $\frac{k}{\delta}$ or Re_k, but further experiments are needed to explore scaling properties.

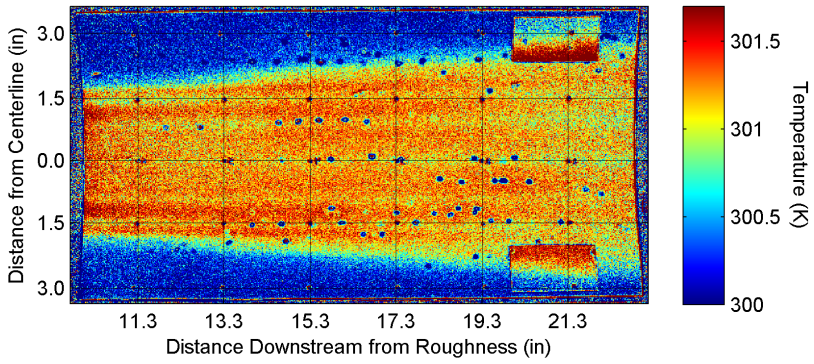

(a) $p_0 = 108.4$ psia, $k = 10.2$ mm, $\frac{k}{\delta} \approx 1.31$, $Re_\infty = 2.56 \times 10^6$/ft.

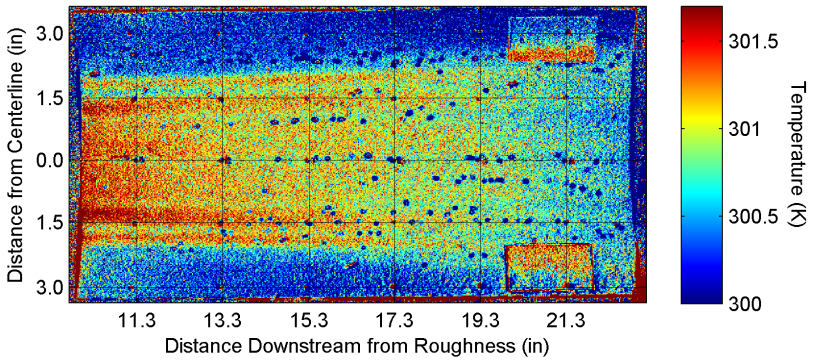

(b) $p_0 = 83.8$ psia, $k = 12.7$ mm, $\frac{k}{\delta} \approx 1.43$, $Re_\infty = 1.95 \times 10^6$/ft.

Figure 4.12. TSP images of similar wakes at different conditions.

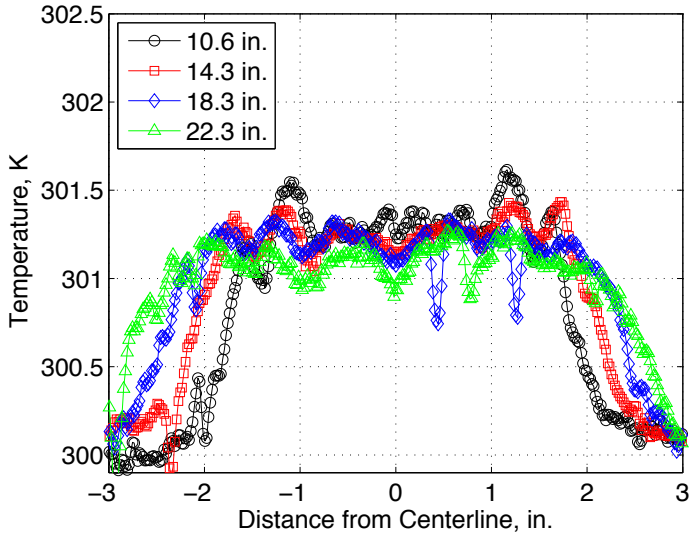

(a) $p_0 = 108.4$ psia, $k = 10.2$ mm, $\frac{k}{\delta} \approx 1.31$, $Re_\infty = 2.56 \times 10^6$/ft.

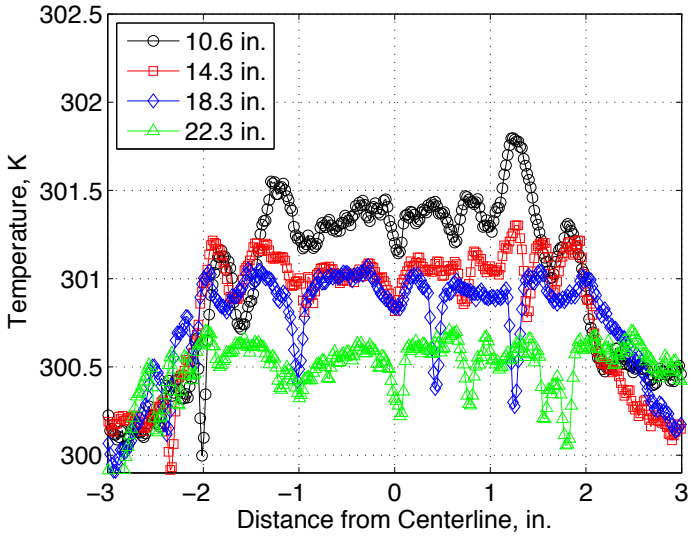

(b) $p_0 = 83.8$ psia, $k = 12.7$ mm, $\frac{k}{\delta} \approx 1.43$, $Re_\infty = 1.95 \times 10^6$/ft.

Figure 4.13. Spanwise wake temperatures from Figure 4.12, looking downstream. Legend indicates distance downstream from the roughness.

4.4 Summary of TSP Measurements

The images in this chapter show preliminary results from temperature-sensitive paint experiments on the nozzle wall. TSP may be used in future experiments to support local measurements of instabilities on the nozzle wall and locate regions of interest for study. The images offer a glimpse of the flow features found in the wake of the isolated roughness. As roughness height is increased in a laminar boundary layer, the wake region widens and several hot streaks become visible. The hot streaks may be vortices or other disturbances in the flow. It is difficult to tell from these images if the flow is laminar or turbulent. Though temperature-sensitive paint images are useful in identifying flow features such as these hot streaks, the flow features need to be studied using other instrumentation such as hot films or hot wires. The TSP images can only provide information on the heating at the wall and not the growth of instabilities within the boundary layer. Furthermore, these TSP images were only available well downstream of the roughness (about 50 diameters). If quantitative heat-transfer can later be obtained from the TSP then a quantitative comparison could be made.

5. PROBE WAKE-MEASUREMENT METHODS

The pitot and hot-wire probes were used in the wake of the roughness element to search for evidence of flow instabilities. A common apparatus was used for both pitot and hot-wire measurements, because the pitot probe and hot-wire probes were similarly shaped. All measurements were taken using the angled probe support to measure near the roughness element. This chapter will show the typical apparatus for measuring in the wake of the roughness and the difficulties related to making these measurements.

Figure 5.1 shows an example of the setup used for pitot-pressure measurements. The pitot probe was installed in the angled probe support and secured using two #4–40 set screws. High-temperature tape was used to secure the probe wires into a slot on the side of the probe support. The wires were then run out of the tunnel. The probe support was installed on the tunnel centerline using the traverse system and suspended from the top wall of the tunnel. Measurements were taken with the probe stationary as well as traversing in the wall-normal direction. The probe was placed at various streamwise locations prior to each run.

The roughness insert was installed on the bottom wall of the tunnel and the roughness height k was adjusted prior to each run. The micrometer reading was converted to roughness height using values shown in Appendix C.1. The roughness was moved between three spanwise locations in order to make both centerline and off-centerline measurements. Figure 5.2 shows a close-up view of the roughness insert, with the roughness positioned two diameters off-center (0.47 in. or 11.94 mm). In the image, flow is from left to right and the pitot probe is located approximately 0.3 in. (7.6 mm) downstream of the roughness. In this configuration, the measurements are taken in a plane two diameters off-center from the roughness. The roughness was also placed in the center hole of the insert to make measurements on the centerline

behind the roughness. Figure 5.3 shows the off-centerline measurement configuration from behind the probe, looking upstream. Due to curvature in the tunnel wall, the plane of the off-center measurements is not parallel to the roughness element. The plane is angled 5.7° with respect to the roughness element.

Figure 5.1 shows a photograph of the pitot probe and angled probe support, looking upstream in the nozzle. The angled probe support descends through the traverse slot on the upper wall of the nozzle. On the right side of the photograph, the rectangular window insert can be seen. The hot-film array was installed on the side wall of the tunnel in one of the small window blanks, offset 90° axially from the roughness location. The array is visible on the left side of Figure 5.1. The hot films were used to verify that the nozzle-wall boundary layer was laminar during the run. Because the hot-film array was offset 90° from the roughness, the wake of the roughness was not expected to interfere with the boundary layer there.

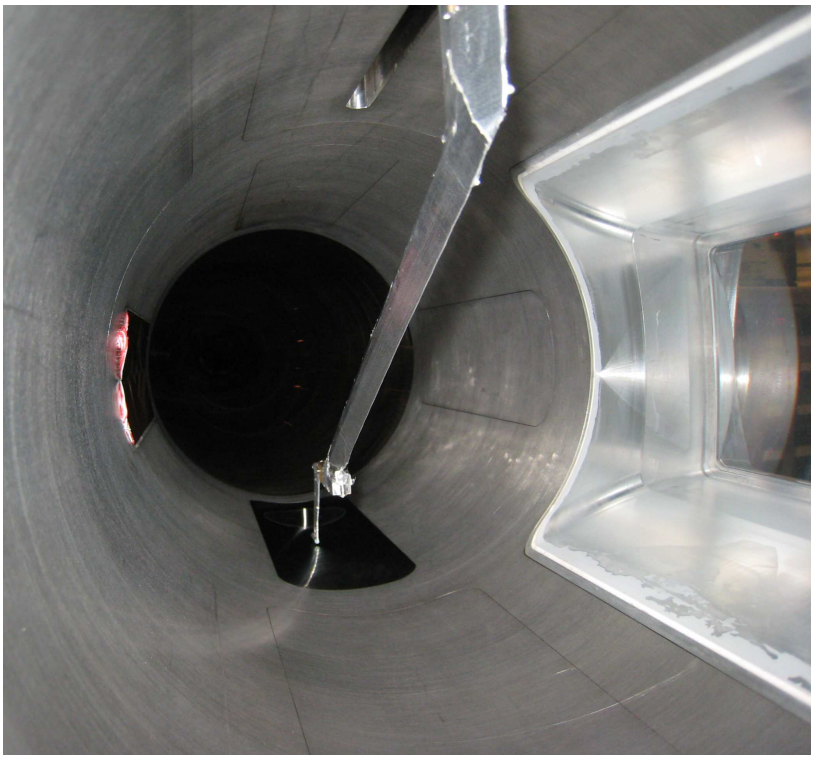

Figure 5.1. Configuration for pitot-probe measurements. A similar configuration was used for hot-wire measurements.

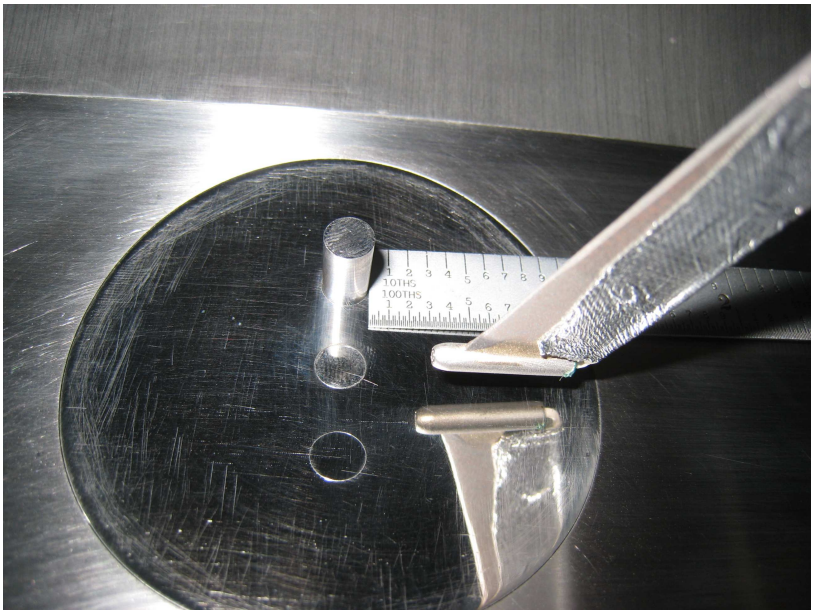

Figure 5.2. Example of measuring off of the roughness centerline. Flow is from left to right. A scale with tenths and hundredths of inches is shown.

Figure 5.3. View of pitot probe and roughness, looking upstream.

5.1 Probe Position

The height of the pitot and hot-wire probes above the tunnel wall were estimated using precision-machined gage blocks, the probe geometry, and the curvature of the tunnel wall at a given streamwise location. The estimated uncertainty using this method was ±0.2 mm, or roughly ±2% of the boundary-layer thickness at p_0 = 90 psia. Once a known probe height was calculated, a record was kept of each vertical movement of the probe in order to determine its instantaneous height. It should be noted that the height of the pitot probe was defined as the height of the center of the 0.066-in.-(1.68-mm-)diameter sensor. The pitot measurements actually report an average stagnation pressure along the entire diameter of the sensor.

The dimensions of the probe support, probe, and traverse system were used to calculate the streamwise position of the probe. A scale was used to verify this position and the error was estimated as ±1.3 mm or ±0.05 in. Two separate MATLAB codes were written to compute the streamwise location of the pitot and hot-wire probes, respectively, based on the reading of the ruler attached to the traverse-system linear positioner. The MATLAB codes also compute the height of the probe above the wall. These codes appear in Appendix B.2. The probes were inserted into the mounting hole in the probe support and tightened with a set screw, making it difficult to set their spanwise position. While tightening the set screw, a straight-edge ruler was used to ensure that the spanwise position of the probe was a close to the tunnel centerline as possible. The estimated uncertainty using this method was ±1.0 mm. In the future, a more accurate method of setting the spanwise position of the probe should be designed.

Traverse motion profiles were designed to move the probe during a run. The direction and distance of each move, number of motion segments, and pause time between moves can be easily adjusted using the traverse motion software. Various motion profiles were used in this experiment and the start of each profile was triggered using the oscilloscopes when the run began. After the run began, a 0.4-s delay prior to move-

ment was used to allow the tunnel to fully start. Using the Motion Planner software, the traverse motor velocity was set to 60 rev/s and the acceleration and deceleration were set to 60 rev/s^2. These values were the highest values allowed without exceeding the torque specifications of the motor. The acceleration and deceleration were used to stop the probe at various positions during the run to record data. When analyzing data, the parameters from each traverse profile were entered into a MATLAB code that calculated the instantaneous height of the probe above the wall during a run (see Appendix B.3).

5.2 Data Analysis

All data from probes in the roughness wake were sampled at 2.0 MHz in Hi-Res mode, which acquires data at the maximum sampling frequency of 500 MHz and averages the points in real-time to 2.0 MHz. This digital filtering increases the number of vertical bits of resolution and decreases the chance of signal aliasing. During runs where the probe was moving, the traverse was halted for 0.05 s between movements to collect data. The vertical scale setting of the oscilloscopes varied from 100 mV/div to 2.0 V/div to capture the entire signal without sacrificing vertical resolution. Appendix A contains additional details about the signal acquisition and processing methods for the probe data.

Mean-flow pitot pressures were collected using the Kulite pitot probe and are reported in Chapter 6. The power spectral density analysis was obtained at each data point using Welch's method (the MATLAB *pwelch* program). The data were sampled at 2.0 MHz for 0.05 s at each point. Windows with 5,000 points were used with 50% overlap. The RMS pitot pressure was calculated by numerically integrating under the power spectrum from 0–100 kHz to remove sensor-resonance effects (see Section 5.8). The RMS pitot pressure was then nondimensionalized by the mean pitot pressure and reported as a percentage.

Measurements of instabilities were collected with both the pitot probe and the uncalibrated and calibrated hot-wire probes (Chapter 7). Spectra were calculated at each height above the wall and were examined for evidence of peaks pertaining to possible disturbances. Each spectrum was computed as a root-mean-squared spectrum from the 0.05-s sample (see Appendix B.4 for the MATLAB code). Blackman windows with 5,000 points and 50% overlap were used, resulting in a total of 30 windows from the 100,000-point sample. All spectra were computed to achieve a frequency spacing Δf of 0.24 kHz. Because the mean pitot pressure was changing at each point, the spectra were normalized by the theoretical freestream pitot pressure. This value was the stagnation pressure behind a normal shock at Mach 6, or 2.965% of the freestream stagnation pressure. A pre-run Kulite spectra was not available due to the settings in the vertical resolution of the oscilloscope. A separate pre-run trace was not obtained. Uncalibrated hot-wire spectra were reported as raw voltage fluctuations while calibrated hot-wire spectra were nondimensionalized by the measured mean mass flux.

5.3 Reynolds-Number Variations

Measurements during a single run in the BAM6QT contain variations in freestream Reynolds number caused by the decreasing pressure in the driver tube. As described in Chapter 2, the tunnel stagnation pressure drops in a stair-step pattern during a run. The tunnel stagnation temperature decreases along with the stagnation pressure and is estimated using the isentropic relation

$$T_0 = T_{0,i} \left(\frac{p_0}{p_{0,i}} \right)^{\frac{\gamma-1}{\gamma}} \tag{5.1}$$

where p_0 and T_0 are the instantaneous stagnation pressure and temperature, and $p_{0,i}$ and $T_{0,i}$ are the initial values at the start of the run. A MATLAB function was used to compute Reynolds number and appears in Appendix B.5. The perfect gas law was used to calculate the freestream density ρ_∞ and Sutherland's law was used for the dynamic viscosity μ_∞.

As a result of the decreasing stagnation pressure, measurements taken during a single run contain variations in Reynolds number. For a quiet-flow run at $p_{0,i} =$ 90 psia, the Reynolds number decreases by roughly 10–15% in 3 s. This variation offers an advantage because frequency-shifting of instabilities can be observed as the freestream Reynolds number changes. However, an accurate profile of the nozzle-wall boundary layer at a given Reynolds number cannot be measured in one run. In the future, a scaling method such as $\sqrt{Re}$ could be used to compare mean-flow measurements to computations at a static Reynolds number.

5.4 Probe-Support Vibration

Vibration of the probe support could interfere with measurements of instabilities and cause the signal from the probes to oscillate. It was hoped that the vibrational frequency of the probe support would be much smaller than the instability frequencies and not interfere with measurements.

An experiment was performed on a test bench to determine the natural vibrational frequencies of the angled probe support. The probe support rods were clamped in a vise and the Kulite pitot probe was installed. The lower portion of the probe support was then tapped lightly with a hammer to induce vibration. The output signal of the Kulite sensor was recorded on an oscilloscope with a 2.5 MHz sampling rate. A signal was also recorded with an undisturbed probe support. Figure 5.4 shows root-mean-square spectra of the undisturbed probe support as well as the vibrating probe support. The spectrum from the vibrating probe support was from 0.05 s after the hammer impact. All fluctuations appeared to dissipate 0.09 s after the hammer impact. The spectra are from 0.015-s samples using 5,000-point Blackman windows with 50% overlap, resulting in a frequency spacing Δf of 0.3 kHz. The vibrating frequencies appeared to be lower than 5 kHz, implying that a longer sampling record is desired in order to resolve the lower frequencies in the spectrum. However, the hammer caused vibrations for less than 0.1 s.

During runs at certain conditions in the tunnel, a 20-Hz oscillation could be seen in the pitot-probe signal which was thought to be vibration of the probe support. Figure 5.5 shows the time trace of the pitot-probe signal when it was stationary at $y = 4.6$ mm above the wall and 11.5 diameters downstream of the roughness. The initial stagnation pressure was 90 psia, the roughness height was 6.6 mm, and the measurements were on the centerline behind the roughness. Immediately after the run began ($t = 0.3$ s) the pressure signal oscillated at 20 Hz and continued to oscillate until the run ended at $t = 2.4$ s. The oscillation amplitude also decreased throughout the run. Perhaps under these conditions a shock from the roughness impinged on the probe support and caused constant vibration during the run. Alternatively, the 20-Hz oscillation could be caused by separation from the sting-support section propagating upstream. Similar low-frequency oscillations have been seen before [46]. It should be noted that the 20-Hz oscillation was not often seen and the probe support never exhibited noticeable vibrations when viewed through the tunnel window. A 20-Hz vibrational frequency is reasonable for the long angled probe support and this low frequency should not interfere with measurements of instabilities that have frequencies that are orders of magnitudes larger (1-200 kHz).

5.5 Probe Interference

The hot-wire probes were not expected to interfere noticeably with the flow due to the small wire diameters. The pitot-probe Kulite sensor diameter was 0.066 in., or roughly 20% of the boundary-layer thickness at $p_{0,i} = 90$ psia. Because of its larger size, the pitot probe was expected to interfere with the flow to some degree, however the probe-interference effect was difficult to quantify.

An experiment was designed to test for probe interference using the tunnel wall hot-film array. The hot-film array was installed on the lower wall of the nozzle in the upstream window blank. The streamwise position of the pitot probe was adjusted so that the upstream edge of the Kulite sensor was aligned with one of the hot films

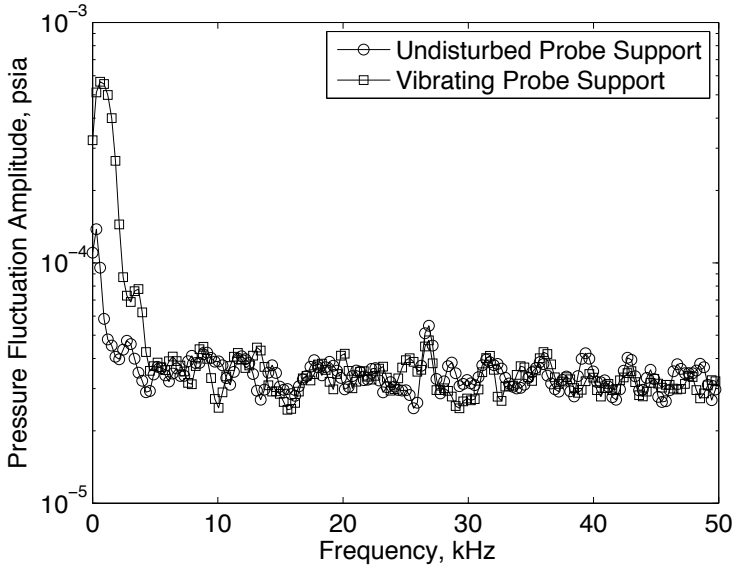

Figure 5.4. Vibration test of probe support on test bench. Mean-squared spectra showing pressure fluctuations of the undisturbed pitot probe as well as $t = 0.05$ s after hammer impact.

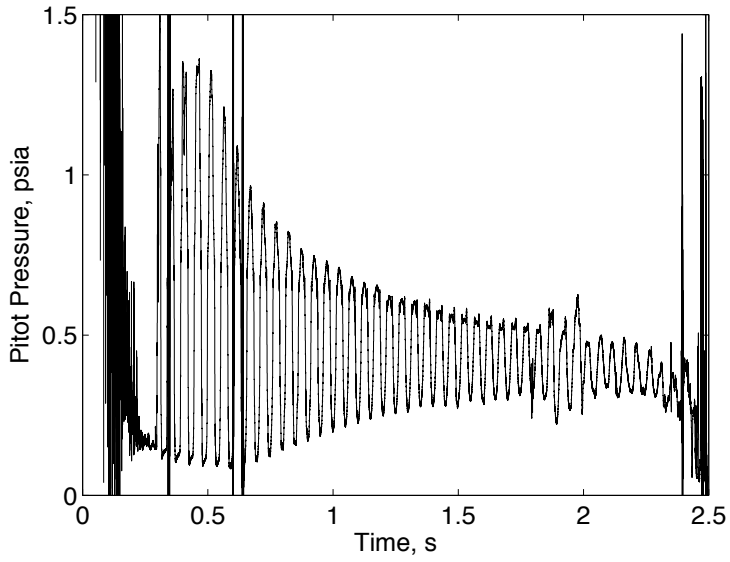

Figure 5.5. Pitot-pressure trace showing possible 20-Hz vibration of probe support. Run with $p_{0,i} = 90$ psia, $k = 6.6$ mm, and $y = 4.6$ mm. The probe was 11.5 diameters downstream of the roughness measuring on the centerline.

on the wall. The RMS voltage of the hot-film beneath the probe was compared to a normal hot-film RMS voltage from a quiet run at similar conditions.

Figure 5.6 shows hot-film data from two separate quiet runs at $p_{0,i} = 90$ psia. The blue trace shows data from hot-film #29 (at $z = 80.5$ in.) on the side wall of the tunnel, away from the pitot probe. The red trace shows data from hot-film #21 (at $z = 78.5$ in.) with the pitot probe positioned directly above it. The probe was 3.4 mm above the hot film at the start of the run and was traversing in the wall-normal direction away from the wall. Both traces show the run beginning near $t = 0.3$ s and ending near $t = 2.4$ s. The mean voltages from the two sensors are different, but the sensors are uncalibrated and this difference does not necessarily indicate a mean-flow effect. The RMS voltages from 0.05-s intervals were computed and were normalized by the pre-run values. The hot-film RMS voltages are similar to the pre-run values, indicating that the flow was laminar with some turbulent bursts visible. Hot-film RMS voltages are typically an order of magnitude larger than the pre-run values for noisy flow [46]. During the run, the hot-film beneath the pitot probe had RMS voltage levels similar to the side-wall hot film, suggesting that there was not a large probe interference effect. The exact probe-interference effect of the Kulite pitot probe, however, is unknown.

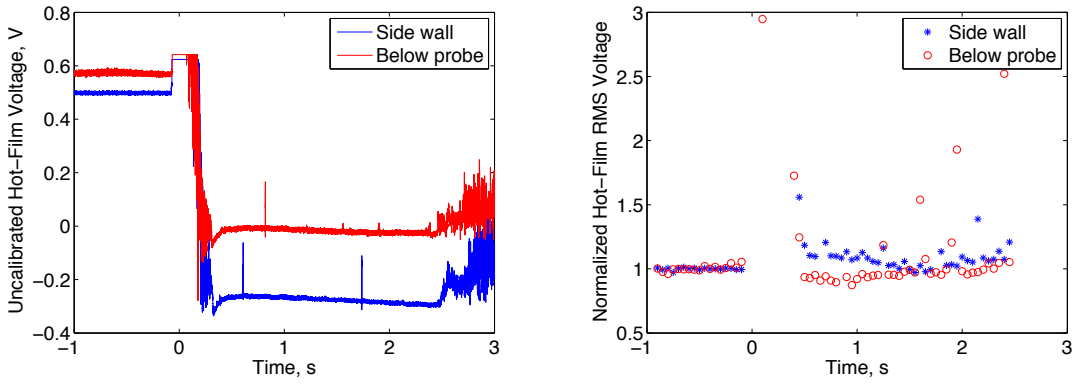

(a) Time traces.

(b) RMS normalized by pre-run values.

Figure 5.6. Comparison of hot-film on side wall of tunnel to hot-film below pitot probe. Two separate runs at $p_{0,i} = 90$ psia.

5.6 Boundary-Layer Separation and Tunnel Configuration

The performance of the new diffuser section and its various inserts is documented in Reference 46, including evidence of boundary-layer separation from the diffuser propagating upstream into the nozzle. This propagating boundary-layer separation could potentially affect the results of measurements in the roughness wake. The separation could be induced by the diffuser and its various inserts, the probe support, or a complicated interaction between the two.

Boundary-layer separation is typically detected by strange oscillations in the wall hot-film array signals or probe signals. Figure 5.7 shows possible boundary-layer separation from a run at $p_{0,i} = 90$ psia with no roughness present. Pressure from the pitot probe is plotted on the left axis and uncalibrated hot-film voltage from hot-film #29 is plotted on the right axis. The pitot probe was located 8.45 mm above the wall at $z = 78.5$ in. The hot film was located on the side wall at $z = 80.5$ in. The pitot-probe signal was oscillating at 20 Hz from $t = 0.5$–1.6 s, perhaps caused by vibration of the probe support (as in Figure 5.5). There are several larger oscillations visible on both sensors toward the end of the run ($t = 1.9$–2.4 s) which may be separation of the laminar boundary layer. An additional oscillation is visible near $t = 0.9$ s. Often, these oscillations were seen at the end of a run prior to the tunnel unstarting. When these oscillations were seen, the data were not used, except for some mean-flow data appearing in Figure 6.3.

A complete study of boundary-layer separation induced by the diffuser and probe support is beyond the scope of this project. However, several methods were found to reduce or eliminate the appearance of oscillations when using the angled probe support. Runs at higher pressure were more likely to keep the laminar boundary layer attached to the nozzle wall. Testing at $p_{0,i} = 40$ psia showed that oscillations in the pitot-probe signals were more prevalent than at $p_{0,i} = 90$ psia and above. The oscillations were less prevalent when measuring far upstream in the nozzle, near the roughness position. In addition, the probe signal was less likely to oscillate when a

roughness was present, perhaps indicating that the roughness wake kept the boundary layer attached. Eliminating the gap between the pipe insert and the nozzle exit was found to minimize oscillations and all reported measurements were taken with the gap closed. The pipe insert extension [40] was not yet installed, except for the data appearing in Figure 7.13. A 7° half-angle cone with a 4-in. base-diameter and 0.06-in.-radius nosetip was inserted into the sting support, to increase the run time. The nose of the model was at tunnel coordinate $z = 91.01$ in, as far downstream as possible. The model was well downstream of the roughness and was not expected to interfere with measurements there. The presence of a model in the sting not only decreased oscillations on the wall hot films but also increased run time by a factor of 50% in some cases.

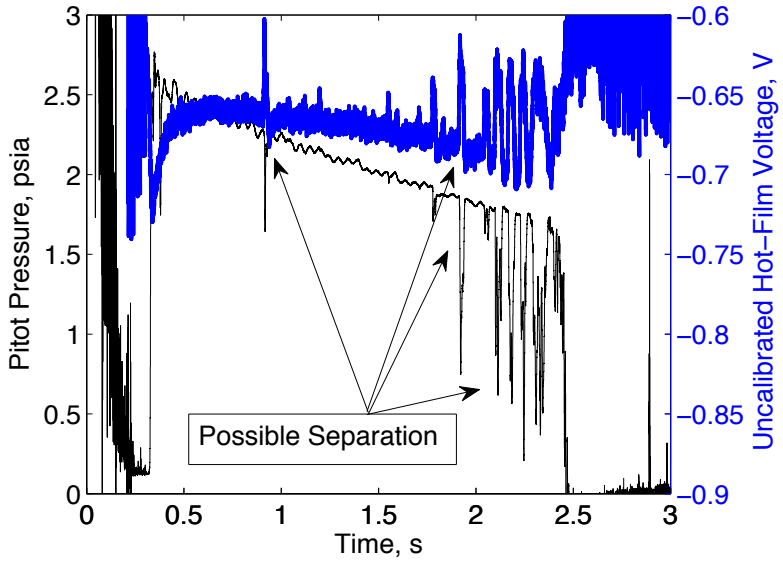

Figure 5.7. Possible boundary-layer separation at $t = 0.9$ s and $t = 1.9$–2.4 s, detected by large oscillations in both the pitot-probe signal and hot-film signal. Run at $p_{0,i} = 90$ psia with no roughness.

5.7 Traverse Electronic Noise

The Parker stepper motor for the traverse system, when powered, generates large amounts of electronic noise. This noise is picked up by hot wires and interferes with measurements of instability waves. To avoid this noise, the traverse must be disabled when using hot wires and the probe can only be in one position during a run [55]. The Kulite pressure transducers do not appear to be susceptible to electronic noise from the traverse and can be moved during a run without affecting measurements. A new Aerotech traverse system has been purchased in order to eliminate electronic noise. The new system consists of an Aerotech NDrive HL 10-80-A-IO controller and BMS280-AH-D25-E2500H brushless DC motor. Initial testing of the system in late 2007 revealed the presence of electronic noise at 132 kHz from a switching power supply in the controller circuitry. The switching power supply was removed by Aerotech in 2008 and was replaced with an external linear power supply. Further testing of noise levels is required before the new system can be installed in the BAM6QT. The ability to move hot-wire probes to multiple positions during a single run while measuring instabilities depends on the elimination of electronic noise from the traverse system.

5.8 Kulite Sensor Resonance

Under certain conditions resonance of the Kulite sensor in the pitot probe was observed. The resonance always occurred at a frequency near 330 kHz. Large-amplitude resonance fluctuations were observed while measuring within the wake of the roughness, when the roughness height was on the order of the boundary-layer thickness or higher. Figure 5.8 shows a sample root-mean-square spectrum of the resonating Kulite. The vertical axis shows RMS pressure fluctuations nondimensionalized by the theoretical freestream pitot pressure. The spectrum was computed during a run at $p_{0,i} = 90$ psia with $k = 10.2$ mm. The probe was measuring 9.5 mm above the wall, 11.5 diameters downstream of the roughness, and two diameters off the roughness

centerline. The frequencies of interest were below 50 kHz while a large spike in the spectrum from sensor resonance appears at 330 kHz. The amplitude of the 330 kHz peak was two orders of magnitude larger than the amplitudes of the frequencies of interest. It remains unclear whether the Kulite resonance affects the spectral pressure amplitudes below 50 kHz. In addition, the large resonance amplitude can cause the Kulite signal to go off the normal vertical scale of the oscilloscope. The data were not used in these instances. It was assumed that the oscilloscope Hi-Res mode, in addition to the high sampling frequency of 2.0 MHz, were sufficient to prevent signal aliasing. In the analysis of pitot-probe spectra, frequencies higher than 100 kHz were simply ignored (30% of the resonance frequency). In the future, perhaps a low-pass filter can be used on the Kulite signal, prior to the oscilloscope, to further reduce any effect of sensor resonance on the lower frequencies in the spectra.

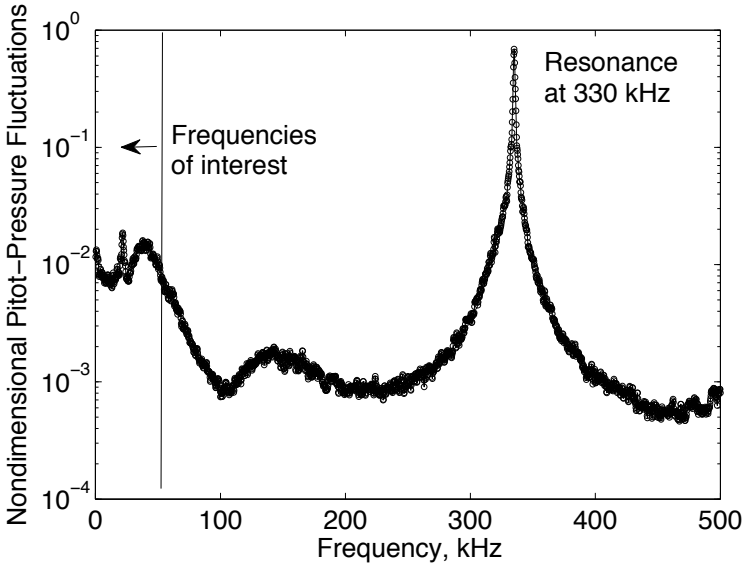

Figure 5.8. Example of Kulite resonance from pitot probe. Pitot-pressure fluctuations nondimensionalized by theoretical freestream pitot pressure.

6. BOUNDARY-LAYER MEAN-FLOW MEASUREMENTS

Mean-flow measurements in the nozzle-wall boundary layer can be used for comparison to computational solutions, both with and without the roughness element. The Kulite pitot probe was mounted on the angled probe support and was used to make measurements in the wake of the roughness element. All mean-flow results in this chapter were collected under quiet flow conditions. The 0.24-m-diameter pipe insert (without the pipe insert extension) was installed in the sting-support section with no gap present. Both the mean pitot pressure and the pressure fluctuations were recorded for various freestream Reynolds numbers, roughness heights, and locations within the wake. All mean pitot pressures were nondimensionalized by the freestream stagnation pressure.

6.1 Smooth-Wall Measurements

Measurements of the nozzle-wall boundary layer in the absence of the roughness element (or smooth-wall case) were performed at an initial stagnation pressure ($p_{0,i}$) of 90 psia. This stagnation pressure was chosen because it was high enough to avoid major problems with separation of the nozzle-wall boundary layer. The stagnation pressure was low enough to increase hot-wire survival, should hot-wires be used at similar conditions.

To collect data, the probe was moved in the wall-normal direction during a single run at $p_{0,i} = 90$ psia. Figure 6.1(a) shows the time trace of the pitot pressure as well as the calculated height of the probe above the wall y. The measurements were taken at $z = 76.1$ in. (1.93 m), near the location where the roughness element is placed. The probe began at a height of 3.37 mm and was moved away from the wall in 0.635-mm steps. A total of 15 data points were measured before the run ended at

$t = 2.4$ s. The pressure signal is roughly constant during times when the probe is stationary. A turbulent burst at 0.6 s occurred during a period when the probe was moving but did not affect the data.

Figure 6.1(b) shows the pitot pressure nondimensionalized by freestream stagnation pressure, and the RMS pitot pressure (from 0–100 kHz) nondimensionalized by the mean pitot pressure. The nondimensional pitot pressure increases away from the wall to a value slightly above 0.03 in the freestream. The theoretical Mach-6 pitot-pressure ratio is 0.02965, assuming a normal shock in front of the sensor. The pitot pressure appears to reach a constant level near $y = 9$–10 mm, suggesting that this is the boundary-layer edge. The RMS pressure fluctuations near the wall reach an amplitude of 6% of the mean and decrease away from the wall. It is unclear why the RMS near the wall is large. Figure 6.2 shows spectra at $y = 3.37$ and 7.81 mm. The pressure fluctuations in the spectra are nondimensionalized by the mean pitot pressure, for consistency with Figure 6.1(b). The largest pressure fluctuations occur at frequencies below 1 kHz. The large RMS could be caused by vibration of the probe support induced by the tunnel startup, or other tunnel starting effects. Runs were performed with the pitot probe moving towards the wall, so that the near-wall region would be measured at the end of the run. However, boundary-layer separation at the end of these runs precluded an accurate comparison of the RMS levels. A peak at 13 kHz in Figure 6.2 could be first-mode instability, as the frequency is similar to the first-mode frequency in computations at $p_0 = 150$ psia (Figure 31 of Reference 44). No higher-frequency peaks were seen in the smooth-wall experiments.

In order to measure a wider range of heights above the wall, several runs must be performed. The probe measurement range is limited by several factors, mainly the run time of the BAM6QT. The time at each data point, distance between points, and traverse acceleration and velocity can be adjusted as desired to maximize the number of data points measured before tunnel shutdown. Figure 6.3 shows mean pressure data from four smooth-wall runs at an initial stagnation pressure of 90 psia, measuring at $z = 78.6$ in. (2.00 m). For each run, the initial height above the

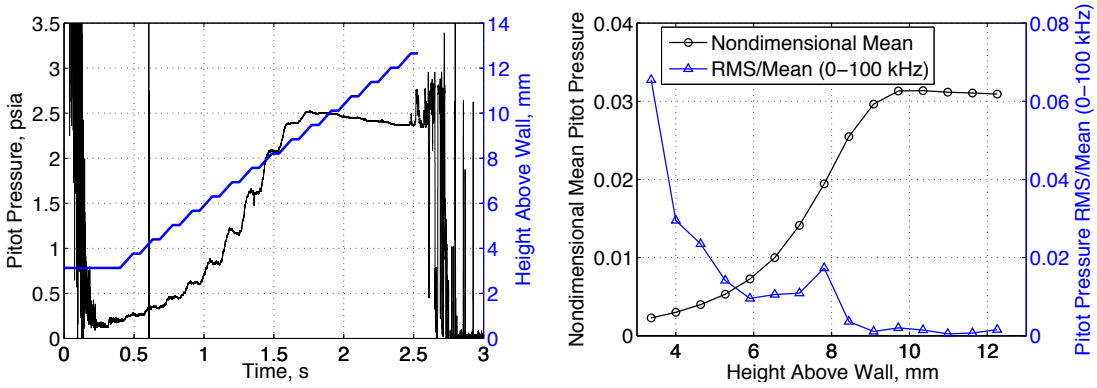

(a) Time trace and probe position.

(b) Mean and RMS pitot pressure.

Figure 6.1. Smooth-wall boundary layer at $z = 76.1$ in. (1.93 m) when $p_{0,i} = 90$ psia.

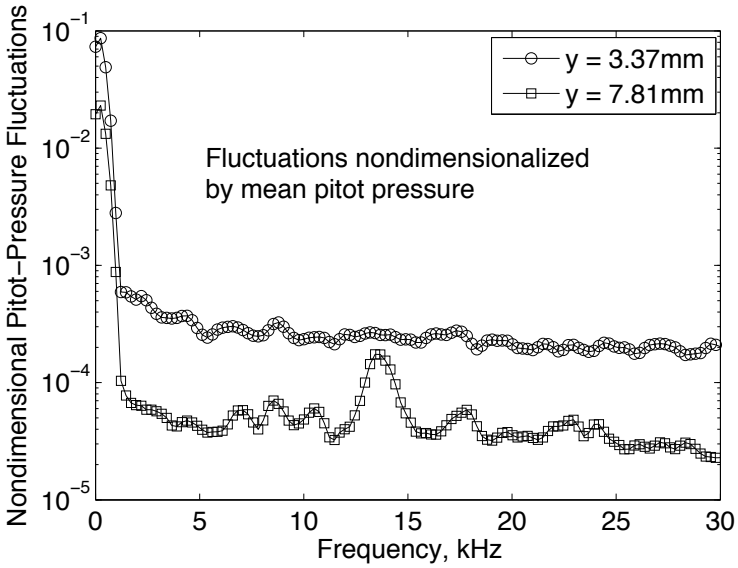

Figure 6.2. Smooth-wall boundary layer spectra at two heights. Same data from Figure 6.1.

wall y_i was varied as well as the movement direction of the probe. The distance between points was 0.635 mm for all four runs. Computations at a similar streamwise location were obtained using the Harris code [44]. The pressures from different runs show relatively good agreement, except near the wall. The disagreement near the wall may result from some boundary-layer separation that was present near the end of the run when moving towards the wall. The boundary-layer separation created oscillations which could have affected the calculation of mean pressure (similar to those in Figure 5.7). Again, the boundary-layer height was roughly 9–10 mm and the mean pitot pressure approached the theoretical freestream value away from the wall. The pitot pressure "overshoots" the theoretical value near the boundary-layer edge. This overshoot is possibly a result of probe interference, caused by the relatively large sensor diameter, as in References 61 and 62. However, the overshoot is not large and the majority of the pitot-pressure data appear to agree well. The freestream pitot pressure indicates a Mach number near 5.95, which is confirmed by the computations. In the BAM6QT, the freestream Mach number is only 6.0 near the nozzle exit, at $z = 101.975$ in, for a stagnation pressure of 150 psia. Upstream of the nozzle exit, the freestream Mach number will be slightly less than 6.0 due to the expanding nozzle area. Lower stagnation pressures will have a similar effect because the boundary layer will be thicker. At $y = 2.7$ mm the computed Mach number is 1.0. At $y = 5$ mm the computed Mach number is 2.0, which is the minimum required for calibrated hot-wire measurements [52].

6.2 Effect of Roughness Height on Mean Pitot Pressure

After characterizing the smooth-wall boundary layer, the effect of roughness height on mean pitot pressures within a laminar boundary layer was examined at an initial stagnation pressure of 90 psia. Each measurement was taken during a single run using the pitot probe. Data were taken at two streamwise locations, 1.2 and 11.5 diameters downstream from the roughness. At each streamwise location, measurements were

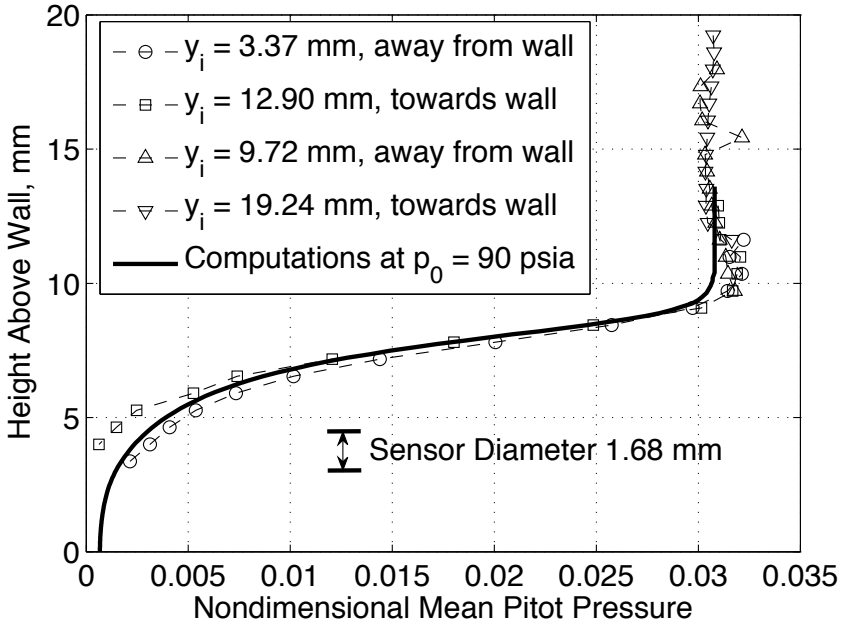

Figure 6.3. Smooth-wall boundary layer at $z = 78.6$ in. (2.00 m) when $p_{0,i} = 90$ psia. Data from four runs with various initial heights above the wall and movement directions. Pitot pressure nondimensionalized by freestream stagnation pressure.

taken with the probe both on and two diameters off the roughness centerline. To maintain consistency, the same motion profile was used for all the data in this section. The probe was moved in the wall-normal direction in 0.635-mm steps. During each run, the probe began near the wall and moved away from the wall. Roughness heights of 2.5, 4.6, 6.6, 7.6, 8.6, and 10.2 mm were tested, though not all roughness heights were tested when measuring off the roughness centerline.

6.2.1 Measurements on Roughness Centerline

Figure 6.4 shows the mean pitot pressures 1.2 diameters downstream from the roughness and on the centerline. The smooth-wall case is plotted for comparison. When $k = 2.5$ mm the mean pitot pressures are similar to the smooth-wall case. As the roughness height is increased further, the mean pitot pressures decrease near the

wall and increase farther from the wall. When k was 4.6 mm or greater, there was an overshoot in pressure above the theoretical Mach-6 value of 0.02965. At the highest roughness height $k = 10.2$ mm, the mean pitot pressures are significantly lower than the smooth-wall values. It is possible that at this roughness height a region of low-velocity separated flow exists immediately behind the roughness, as in Whitehead (see Figure 1.6) [33]. In future tests, it would be useful to gather data at heights higher than $y = 12$ mm.

Results from measuring on the roughness centerline and 11.5 diameters downstream appear in Figure 6.5. Farther downstream, the pressures are more similar to the smooth-wall case for larger roughness heights. Larger roughness heights cause higher pressures near the wall when compared to the smooth-wall case; the opposite trend was observed farther upstream in Figure 6.4. Away from the wall, the pitot pressures remain lower than the smooth-wall case. For roughness heights less than 10.2 mm, the mean pressures are more similar to the smooth-wall case at 11.5 diameters downstream than they are at 1.2 diameters downstream. It is possible that, for these roughness heights, the boundary layer behind the roughness could be relaxing towards a laminar state.

6.2.2 Measurements off Roughness Centerline

At 1.2 diameters downstream the roughness was moved into the off-center position. Measurements were taken with the probe two diameters off-center from the roughness (Figure 6.6). Roughness heights up to 10.2 mm are similar to the smooth-wall case. Only one intermediate height was tested due to the detection of an instability when $k = 10.2$ mm (see Chapter 7). Further testing of mean flow pitot pressures was not performed at this downstream location.

Figure 6.7 shows pitot pressures at 11.5 diameters downstream and two diameters off-center from the roughness. The mean pressures remain similar to the smooth-wall case for roughness heights up to 7.6 mm. As the roughness height is increased

further, pressures begin to decrease near the wall. The $k = 10.2$ mm case shows a sharp increase in pressure near $y = 9$ mm and then a gradual decrease in pressure away from the wall.

Figure 6.8 and 6.9 show comparisons of the centerline and off-centerline data at both streamwise positions. Only data from similar roughness heights are plotted. The blue lines show the centerline data while the red lines show the off-centerline data. At both streamwise locations, the off-centerline pitot pressures were more similar to the laminar smooth-wall case than the centerline pitot pressures.

6.3 Possible Shock Location in 10.2-mm Roughness Wake

Mean pitot pressures were recorded at a number of locations downstream of the $k = 10.2$ mm roughness element during measurements of the flow instability. The pitot probe was positioned two diameters off-center from the roughness element and runs were performed with an initial stagnation pressure of 90 psia. Measurements were taken during multiple runs at 2, 3, 5, and 10 diameters (D) downstream of the roughness. At each streamwise position, 2–3 runs were performed with different initial heights above the wall and different movement directions. Data were acquired at wall-normal intervals that varied between 0.3, 1.0, and 2.0 mm.

The results are plotted in Figure 6.10. During each run, the Reynolds number changed by roughly 10%, and differences in pitot pressures between two similar heights can be attributed to Reynolds number differences. Smooth-wall data at $z = 76.1$ in., near the location where the roughness is placed, are also plotted for comparison. The measurements in the wake of the roughness show an overshoot of the theoretical Mach-6 value of 0.2965, followed by a sudden decrease in pressure. This trend is more visible at 5 and 10 roughness diameters downstream where the pitot pressure decreases by 30–40% within a few millimeters. The rapid decrease in pressure was assumed to indicate the location of a shock; it corresponded to a peak in the RMS pressure. The assumed shock locations are denoted by boxes in Figure 6.10 and are summarized in

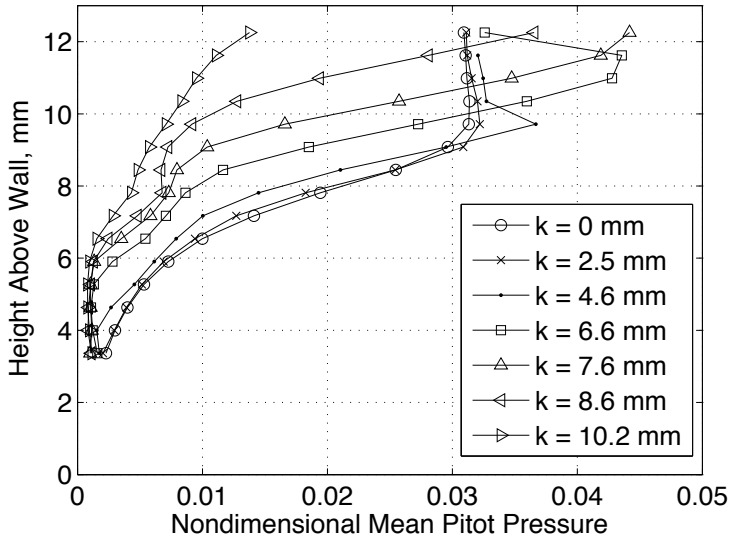

Figure 6.4. Mean pitot pressures on the centerline behind the roughness and 1.2 diameters downstream. Pitot pressure nondimensionalized by freestream stagnation pressure.

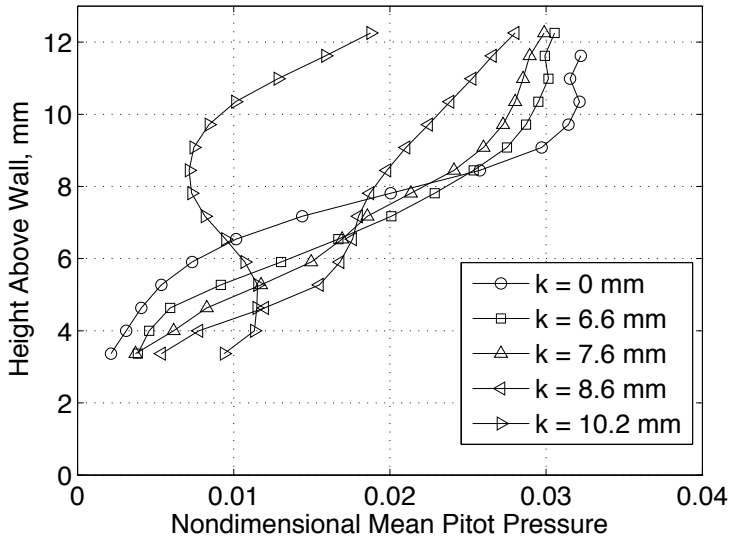

Figure 6.5. Mean pitot pressures on the centerline behind the roughness and 11.5 diameters downstream. Pitot pressure nondimensionalized by freestream stagnation pressure.

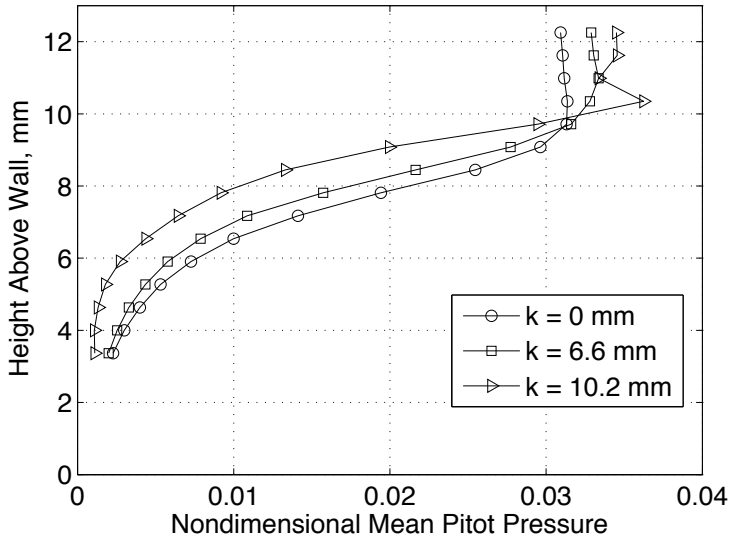

Figure 6.6. Mean pitot pressures two diameters off-center in the roughness wake and 1.2 diameters downstream. Pitot pressure nondimensionalized by freestream stagnation pressure.

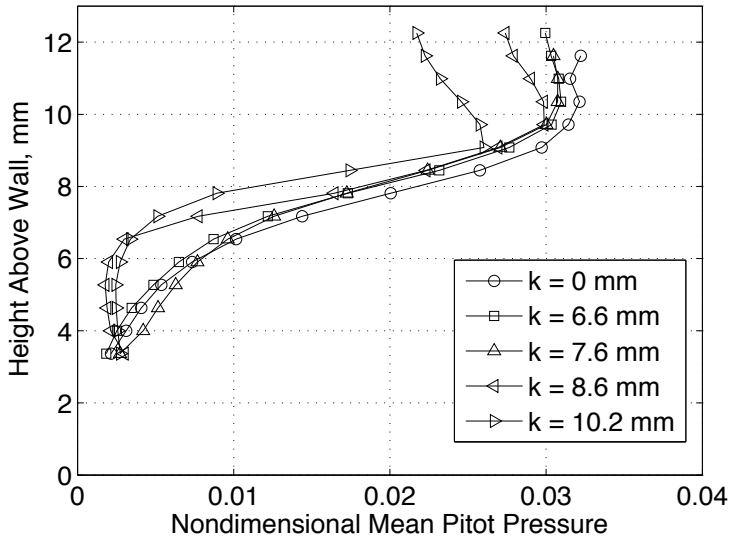

Figure 6.7. Mean pitot pressures two diameters off-center in the roughness wake and 11.5 diameters downstream. Pitot pressure nondimensionalized by freestream stagnation pressure.

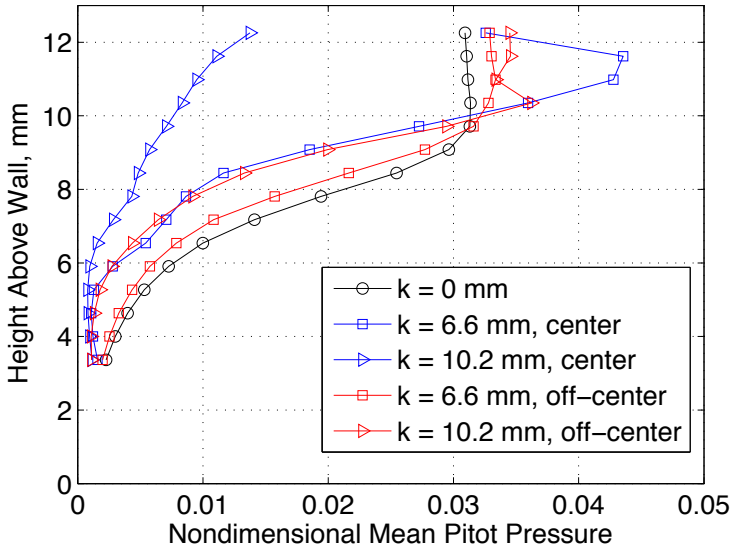

Figure 6.8. Comparison of mean pitot pressures 1.2 diameters downstream of the roughness, on the centerline and two diameters off the centerline. Pitot pressure nondimensionalized by freestream stagnation pressure.

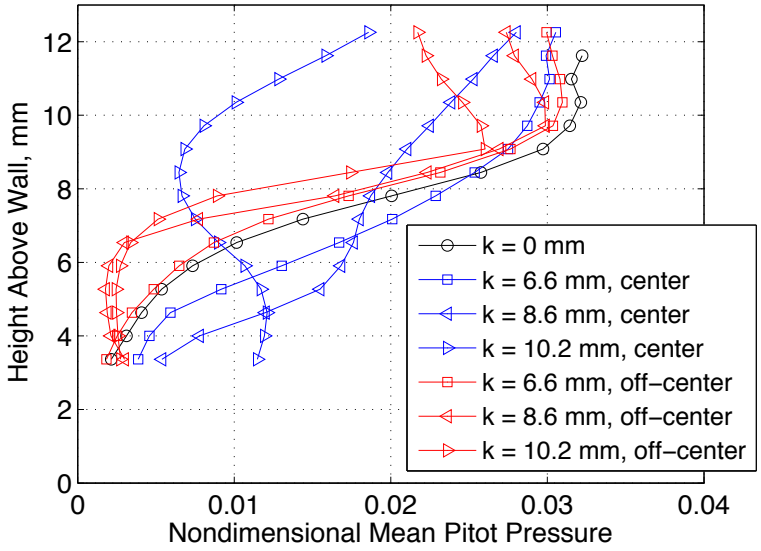

Figure 6.9. Comparison of mean pitot pressures 11.5 diameters downstream of the roughness, on the centerline and two diameters off the centerline. Pitot pressure nondimensionalized by freestream stagnation pressure.

Table 6.1. A plot of the assumed shock locations versus streamwise distance appears in Figure 6.11 and a linear fit to the four points shows the shock shape. The linear fit does not originate from the top of the roughness element, however; the measurements were taken in a plane two diameters off-center from the roughness. Computations are needed to determine if an actual shock location has been found.

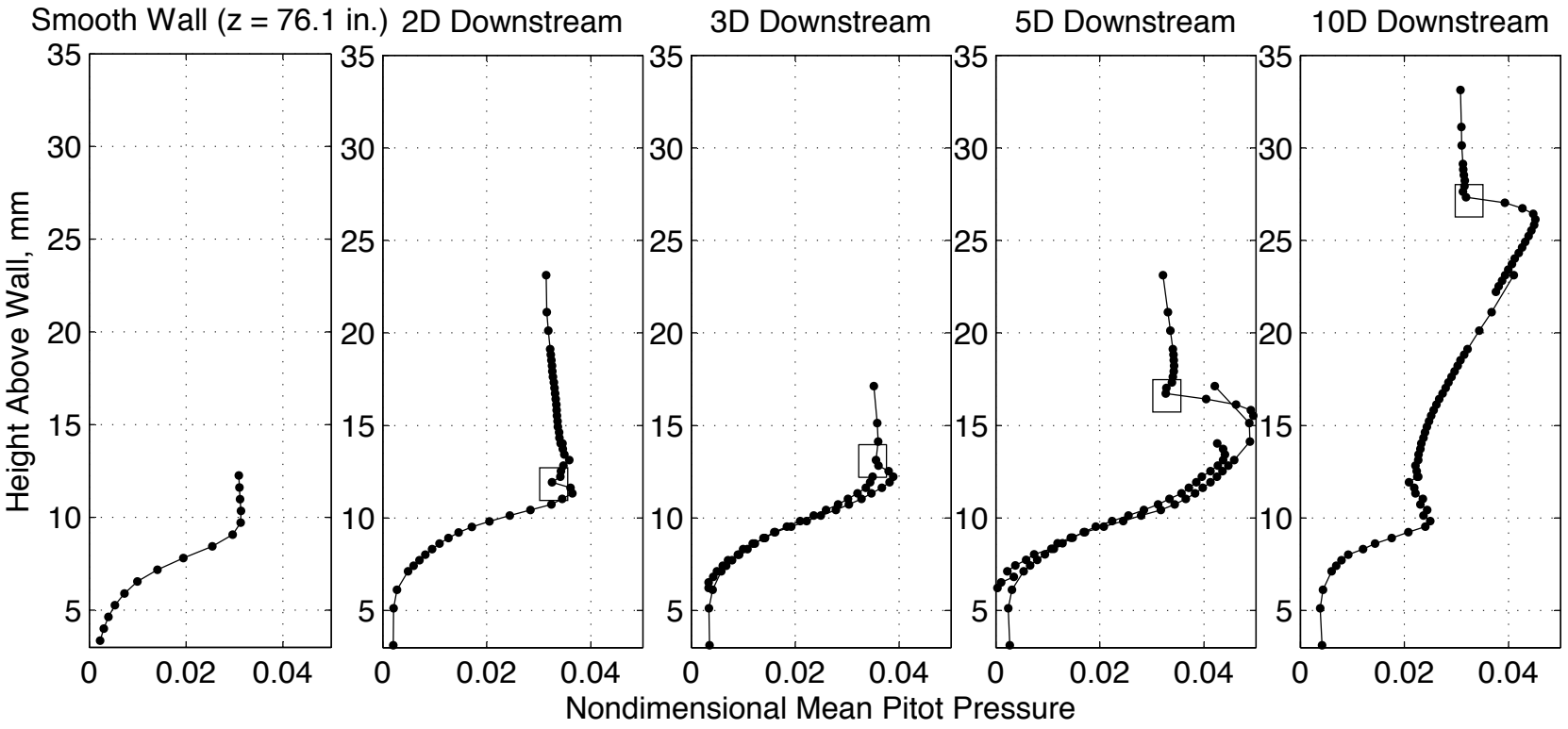

Figure 6.10. Mean pitot pressures at several streamwise distances behind the 10.2-mm roughness and two diameters off the centerline. Pitot pressure nondimensionalized by freestream stagnation pressure. Boxes denote assumed shock location. Multiple runs at $p_{0,i} = 90$ psia. Conditions typically varied from $p_0 = 87$ psia, $T_0 = 430$ K, and $Re_\infty = 2.00 \times 10^6$/ft to $p_0 = 70$ psia, $T_0 = 405$ K, and $Re_\infty = 1.75 \times 10^6$/ft.

Table 6.1 Assumed values of shock height above wall when $p_{0,i} = 90$ psia and $k = 10.2$ mm. Measuring two diameters off the roughness centerline.

Diameters Downstream	Distance Downstream (mm)	Shock Height (mm)
2.0	11.94	11.93
3.0	17.91	12.83
5.0	29.85	16.73
10.0	59.69	27.33

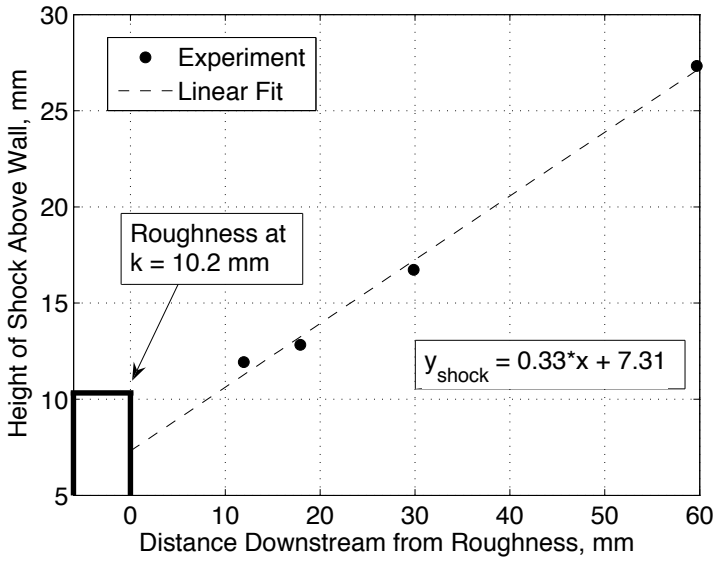

Figure 6.11. Plot of assumed shock shape behind the roughness in a plane two diameters off-center from the roughness.

7. LAMINAR INSTABILITY IN THE ROUGHNESS WAKE

Under certain conditions, a laminar instability was found in the wake of the roughness element. This is believed to be the first such measurement at hypersonic speeds. The instability was observed two diameters off-center from a 10.2-mm roughness during runs with initial stagnation pressures of 75, 80, and 90 psia. The instability was generally observed between stagnation pressures of 70–90 psia, corresponding to stagnation temperatures of 405–433 K and unit Reynolds numbers of 1.7–2.0 $\times$ 10^6/ft. All runs were quiet with a laminar boundary layer on the nozzle wall. The instability was seen in a streamwise position range of 1.2–26.8 diameters downstream of the roughness, and no measurements farther downstream were made. Several tests were performed in order to ensure that the instability is real. Stray effects such as vibration and shock/boundary-layer interactions, however, have yet to be fully ruled out. The largest concern remains an unsteady shock/boundary-layer interaction caused by the roughness, probe, or probe support. Non-intrusive measurements or stability computations are needed for these conditions. Should the computations and experiments agree, the existence of the laminar instability will be confirmed.

7.1 Method Used to Search for Instabilities

A series of experiments were performed to search for evidence of an instability within the wake of the roughness at an initial stagnation pressure of 90 psia. The Kulite pitot probe was used to avoid hot-wire breakage problems. The roughness height was varied and the pitot probe was traversed within the wake of the roughness during a single run. Roughness heights of 2.5, 4.6, 6.6, 7.6, 8.6, and 10.2 mm were

tested. The roughness heights that were surveyed are the same as those that appear in Figures 6.4–6.7 in Section 6.2.

Initial tests were performed on the centerline behind the roughness, 11.5 diameters downstream. For roughness heights of 4.6 mm and 6.6 mm, no apparent peaks in the spectra were visible. However, a 20-Hz oscillation was seen in the time trace. This 20-Hz oscillation was likely vibration of the probe support from an impinging shock or the tunnel startup process. When the roughness height was increased to 10.2 mm, the Kulite signal oscillated with large amplitude at a frequency of 330 kHz, attributed to sensor resonance.

Similar tests were performed with the roughness in the off-center position. Results from Danehy et al. showed large disturbances in a hypersonic roughness wake off-centerline behind the roughness (Figure 1.8) [34]. At first, the sensor was positioned 11.5 diameters downstream of the roughness and two diameters off-center from the roughness. As the roughness height was increased to 10.2 mm the Kulite again resonated with large amplitude at 330 kHz. The sensor was then moved to 1.2 diameters downstream (closer to the roughness). The roughness height was gradually increased to 10.2 mm, at which point oscillations at 21 kHz were seen in the time trace and spectra. The 21-kHz oscillations were visible in the spectra at 11.5 diameters downstream, but were not immediately apparent in the time trace due to the sensor resonance. The 21-kHz oscillations are thought to be a laminar instability within the roughness wake.

7.2 Laminar Instability at 21 kHz

At a roughness height of 10.2 mm, the 21-kHz instability was large enough to be seen clearly in the time trace of the pitot-probe pressure signal. Figure 7.1(b) shows the pitot-pressure trace from a run at $p_{0,i} = 90$ psia when $k = 10.2$ mm. The probe was placed 1.2 diameters downstream from the roughness, measuring two diameters off the centerline. In Figure 7.1(a), a smooth-wall pressure trace at the

same streamwise location is shown for comparison. The horizontal axis indicates the run time of the BAM6QT. Shutdown occurred at $t = 2.5$ s for both runs and was detected by large oscillations in the pitot pressure and wall hot films (not shown). During the run, the probe was moved away from the wall and through the boundary layer. The left axis and the black trace show the pitot pressure, and the right axis and blue trace show the probe height above the wall prior to the tunnel shutdown. Oscillations of increasing amplitude at 21 kHz were seen in the pressure trace when $k = 10.2$ mm. The oscillations had the highest amplitude near $y = 11$ mm. At heights higher than 11 mm, the oscillations began to decrease in amplitude.

The instability was again observed when the pitot probe was left stationary during a run at a height of $y = 8.5$ mm with $k = 10.2$ mm. During the entire 2.4-s run, the 21-kHz oscillation could be seen in the unfiltered time trace of the pressure signal. The run was repeated at the same conditions using an uncalibrated hot-wire probe instead of the pitot probe. The two signals are shown for comparison in Figure 7.2. The pitot-probe signal was reduced to pressure while the hot-wire signal is reported as uncalibrated voltage. The time traces of both signals show a 21-kHz oscillation. The mean pressure level was around 1 psia with a maximum fluctuation amplitude of ± 0.05 psia (or roughly 5% of the mean pressure, or 1.9% of the freestream pitot pressure). The uncalibrated voltage from the hot-wire was intended only for qualitative comparison to the pressure waveform. The 21-kHz peaks were seen when using both types of probes.

A spectral analysis was performed on the time traces of the signals from $t = 1.5$–1.6 s, as shown in Figure 7.3. The spectra were nondimensionalized by the theoretical freestream pitot pressure at Mach 6.0, and show a clear peak at 21 kHz. A narrow frequency band of roughly 3–4 kHz indicates a RMS pressure of 0.4% of the freestream pitot pressure. This value is lower than the 1.9% estimate from Figure 7.2 because it is a RMS (not amplitude). In addition, the root-mean-squared spectrum shows the power of 0.24-kHz frequency bands (based on the frequency spacing Δf). A more representative RMS could be calculated by integrating the area under the power

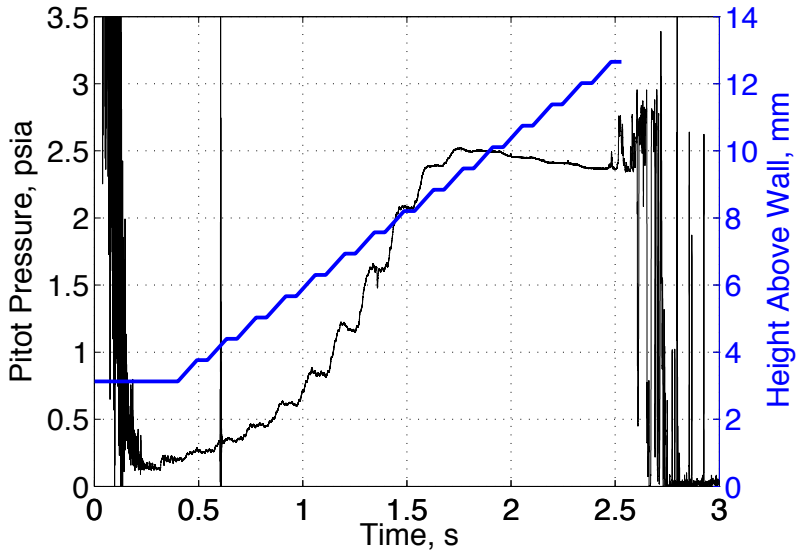

(a) $k = 0$ mm

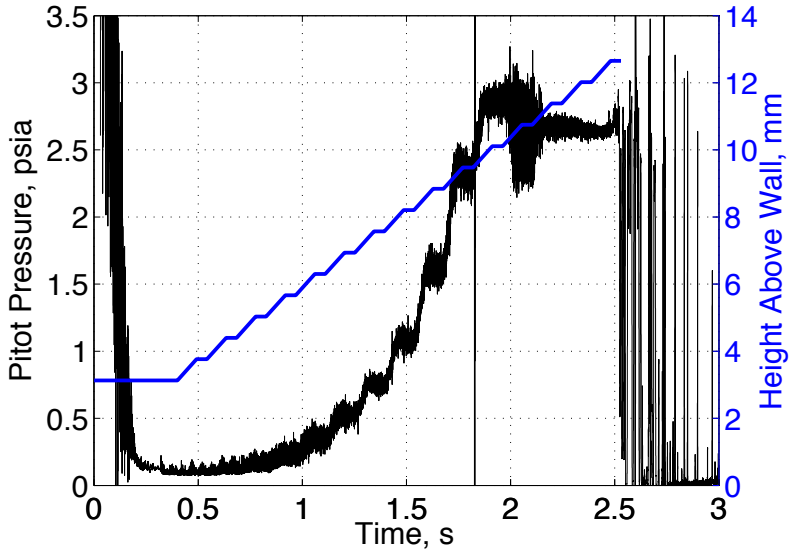

(b) $k = 10.2$ mm

Figure 7.1. Two runs at $p_{0,i} = 90$ psia with the probe moving in the wall-normal direction. The 21-kHz oscillation can be seen in the time trace when $k = 10.2$ mm. The probe was 1.2 diameters downstream from the roughness, measuring two diameters off the centerline.

spectrum from 19–23 kHz (see Appendix A). In addition to the 21-kHz peak, a peak near 42 kHz is visible in the pitot-probe spectra. This second peak may be a harmonic of the 21-kHz frequency, but is not visible in the hot-wire spectra. The uncalibrated hot-wire spectra has a peak at 40 kHz which is likely resonance of the wire due to poor tuning. This particular hot-wire was only tuned to a frequency of 40 kHz due to problems with the anemometer.

Figure 7.4 shows a comparison of pitot-pressure spectra from runs with and without the roughness element. The pressure fluctuations were again nondimensionalized by the theoretical freestream pitot pressure at Mach 6.0. The data are from the same runs that appear in Figure 7.2 and are from a height of 11 mm above the wall. This height is where the fluctuation levels were near their peak. For both runs, the probe was 1.2 diameters downstream from the roughness element location. In the absence of the roughness element, broadband fluctuation levels near 0.01–0.001% (per 0.24 kHz) can be seen, suggesting that the boundary-layer was laminar as expected. A small peak near 13 kHz was seen, which may or may not be a physical instability in the smooth-wall boundary layer. When the roughness height k was 10.2 mm, the fluctuation levels increased by nearly three orders of magnitude. A sharp peak at 21 kHz can be seen with an amplitude of 3% (per 0.24 kHz). Two harmonics are visible at 42 kHz and 63 kHz.

Table 7.1 shows the RMS pitot-pressure fluctuations from Figure 7.4, calculated by integrating the area under the power spectrum, and nondimensionalized by the freestream pitot pressure. The RMS of the signal (from 0–100 kHz to avoid resonance effects) increases from 0.05% to 5.1% when the roughness is present. The instability peak (19–23 kHz) has an RMS of 4.1% when the roughness is present.

The 21-kHz oscillations were seen on two different probe types at similar conditions, suggesting that the oscillation was not caused by the sensor and is a flow instability. However, both probes were used in a similar apparatus, so vibrations or shock/boundary-layer interactions from the angled probe support cannot be fully

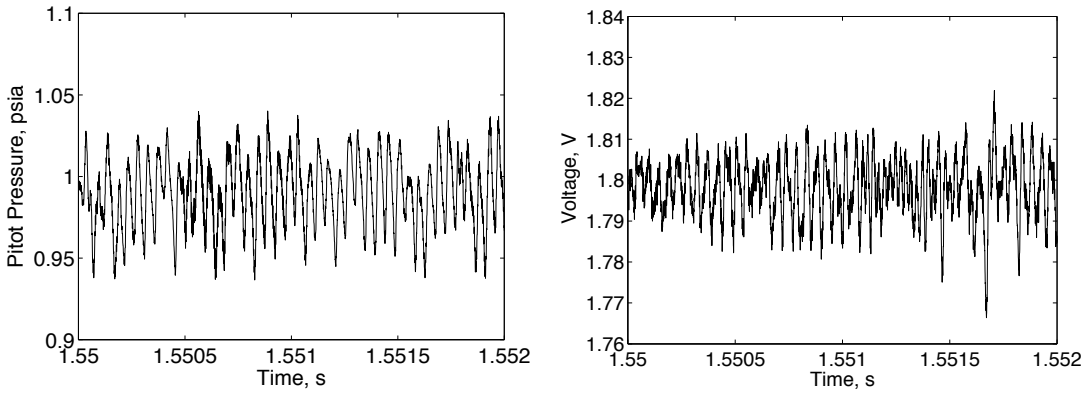

(a) Kulite (b) Hot Wire

Figure 7.2. Time trace of 21-kHz disturbance using two different sensors at similar conditions. Measuring two diameters off-center from roughness and 1.2 diameters downstream. $p_{0,i} = 90$ psia, $k = 10.2$ mm, and $y = 8.5$ mm.

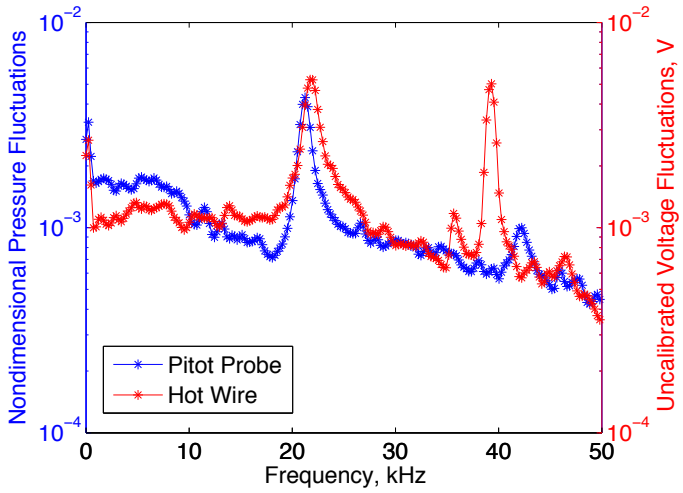

Figure 7.3. Spectra showing 21-kHz disturbance using two different sensors at similar conditions. Measuring two diameters off-center from roughness and 1.2 diameters downstream. $p_{0,i} = 90$ psia, $k = 10.2$ mm, and $y = 8.5$ mm. Pitot-pressure fluctuations nondimensionalized by freestream pitot pressure. Uncalibrated voltage fluctuations from the hot wire are shown.

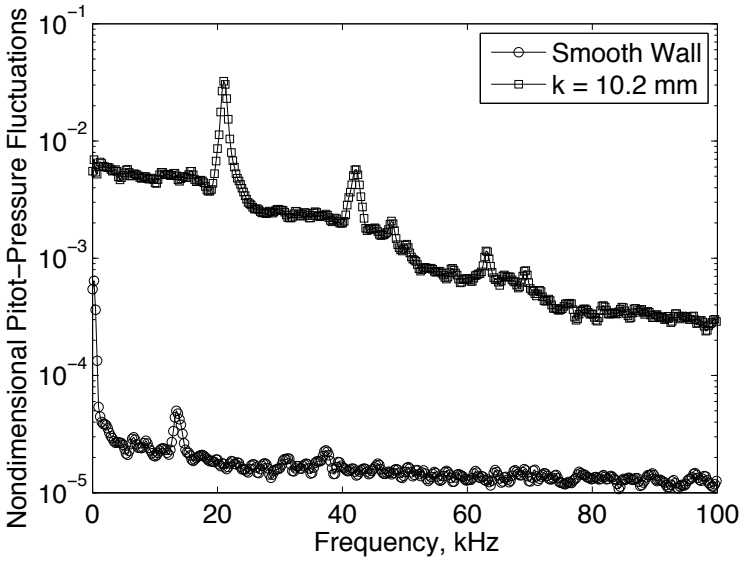

Figure 7.4. Comparison of spectra with and without the roughness at $p_{0,i} = 90$ psia. Spectra from data appearing in Figure 7.1 at a height of 11 mm above the wall. Pitot-pressure fluctuations nondimensionalized by freestream pitot pressure.

Table 7.1 RMS pitot-pressure fluctuations from Figure 7.4, nondimensionalized by the freestream pitot pressure. The RMS was calculated by integrating the area under the power spectrum.

	Smooth Wall	$k = 10.2$ mm
Total (0–100 kHz)	0.05%	5.1%
Peak (19–23 kHz)	–	4.1%

ruled out. When the roughness element is removed, the instability cannot be seen and the fluctuation levels in the flow decrease.

7.3 RMS of 21-kHz Instability Versus Height

An instability within the wake of the roughness element would be expected to disappear away from the wall in the freestream flow. At an initial stagnation pressure of 90 psia, the RMS of the 21-kHz instability was examined at 1.2 diameters downstream and two diameters off-center from the roughness. Three runs were performed with the pitot probe moving in the wall-normal direction. Each run began at a different initial height above the wall y_i and the probe was moved either towards or away from the wall. The power spectral density analysis was obtained at each data point using Welch's method (the MATLAB *pwelch* program). The data were sampled at 2.0 MHz for 0.05 s. Windows with 5,000 points were used with 50% overlap. The area under the 21-kHz peak was integrated from 19–23 kHz using trapezoidal integration to find the RMS of the frequency band (see Appendix A).

Figure 7.5 shows the root-mean-square pressure fluctuations of the 19–23 kHz frequency band at various heights above the wall. A red horizontal line denotes the roughness height of 10.2 mm. The 21-kHz instability increases away from the wall, peaking at a height near the roughness height. The peak fluctuations are around 2.5% of the freestream pitot pressure. At heights greater than 15 mm, the RMS fluctuation decreases to near zero in the freestream. This pattern suggests an instability is being detected.

7.4 Spectra at Various Heights and Streamwise Locations

At 1.3, 5, and 10 diameters downstream of the roughness, pressure-fluctuation spectra were plotted at different heights above the wall (Figures 7.6 through 7.8). The spectra were computed from several runs at each location, at various freestream Reynolds numbers, and the fluctuations were nondimensionalized by the theoretical

freestream pitot pressure. The measurements were taken two diameters off-center from the roughness. Nondimensional RMS at each height is reported in the legend and is defined as the RMS of the signal from 0–100 kHz divided by the mean pitot pressure.

Figure 7.6 shows the pitot-pressure spectra at 1.2 diameters downstream from the roughness. At several heights, the 21-kHz peak is visible and is largest at a height of 11.03 mm (consistent with Figure 7.5). Near the wall, broadband noise with an RMS of 10% can be seen which may be probe interference or noise from the tunnel startup. Higher peaks near 40–50 kHz can be seen at certain heights. It is unclear if these peaks are harmonics. Away from the wall, the spectra appear to decrease gradually to freestream levels.

At five diameters downstream from the roughness, the spectra appear to have higher fluctuation levels and are more broadband than at 1.2 diameters downstream (Figure 7.7). A 21-kHz peak can be seen at $y = 12.83$ mm, however at other heights is not visible. A large RMS of 20–25% near the wall could be probe interference, tunnel startup effects, turbulence, or a combination of the three.

Figure 7.8 shows spectra at ten diameters downstream. Here, the 21-kHz peak is visible at more heights than at five diameters downstream. The peak grows and is largest near 11 mm above the wall, then decays away from the wall. The broadband noise near the wall is very large, with an RMS above 30% of the mean. At 31 mm above the wall, the freestream RMS is 0.1%.

No clear trends are apparent in Figures 7.6 through 7.8, however the 21-kHz peak is often visible at various heights above the wall. It remains unclear why the 21-kHz peak is less visible five diameters downstream from the roughness, but more visible at ten diameters downstream. It is possible that the 21-kHz disturbance does not grow in a plane parallel to the roughness wake centerline. In addition, the variations in Reynolds numbers when measuring at each height could have significant effects on the spectra.

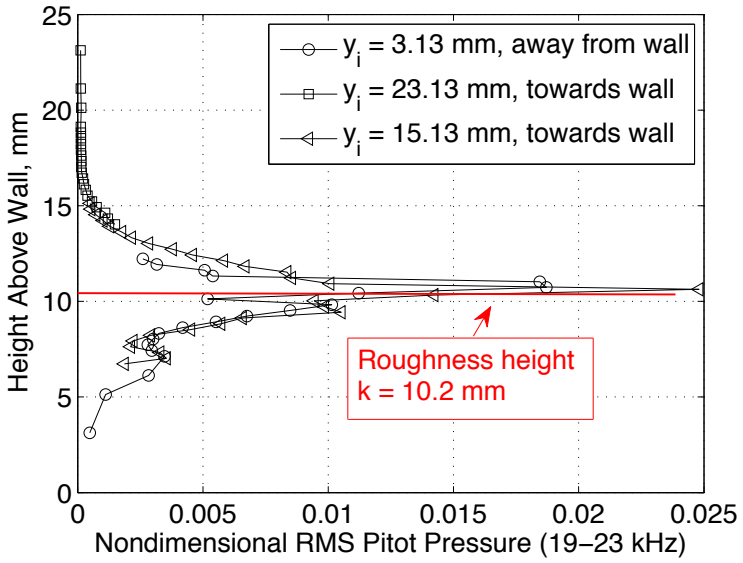

Figure 7.5. RMS pressure fluctuations in the 19–23 kHz frequency band, nondimensionalized by the theoretical freestream pitot pressure. Three runs. Probe was 1.2 diameters downstream of the roughness and two diameters off the centerline. Peak in RMS seen near roughness height of 10.2 mm.

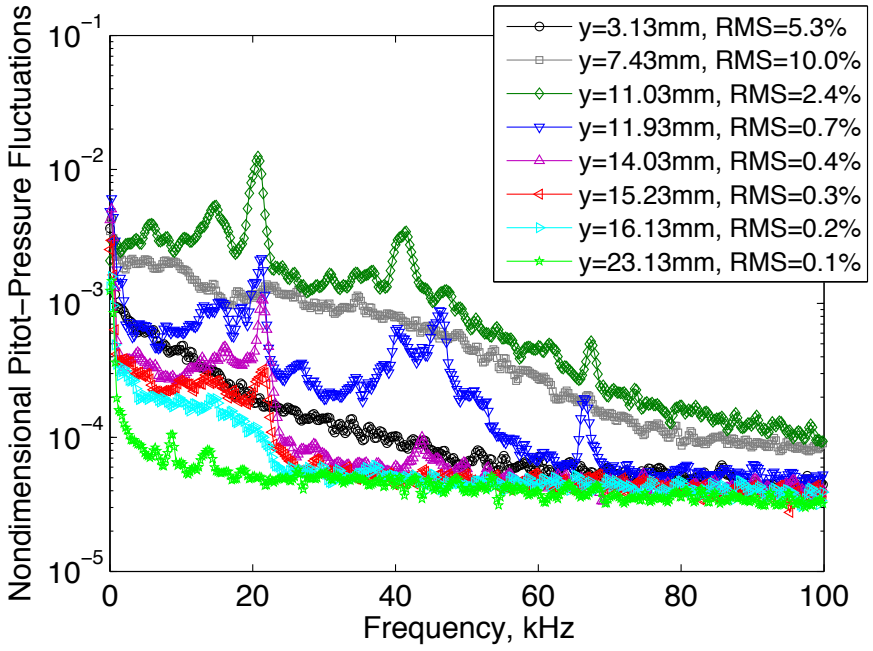

Figure 7.6. Spectra at 1.2 roughness diameters downstream. Pitot-pressure fluctuations nondimensionalized by freestream pitot pressure.

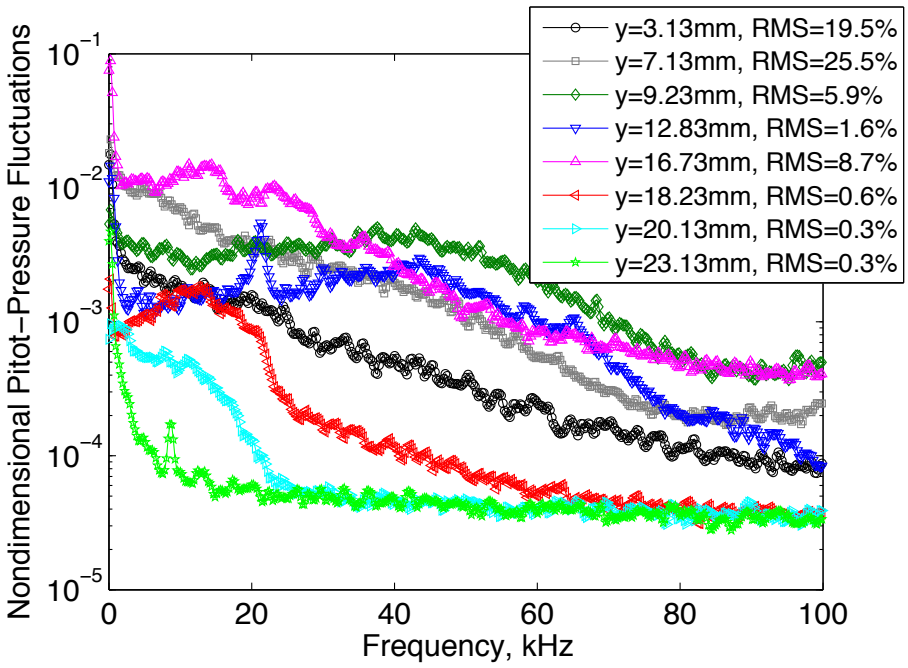

Figure 7.7. Spectra at five roughness diameters downstream. Pitot-pressure fluctuations nondimensionalized by freestream pitot pressure.

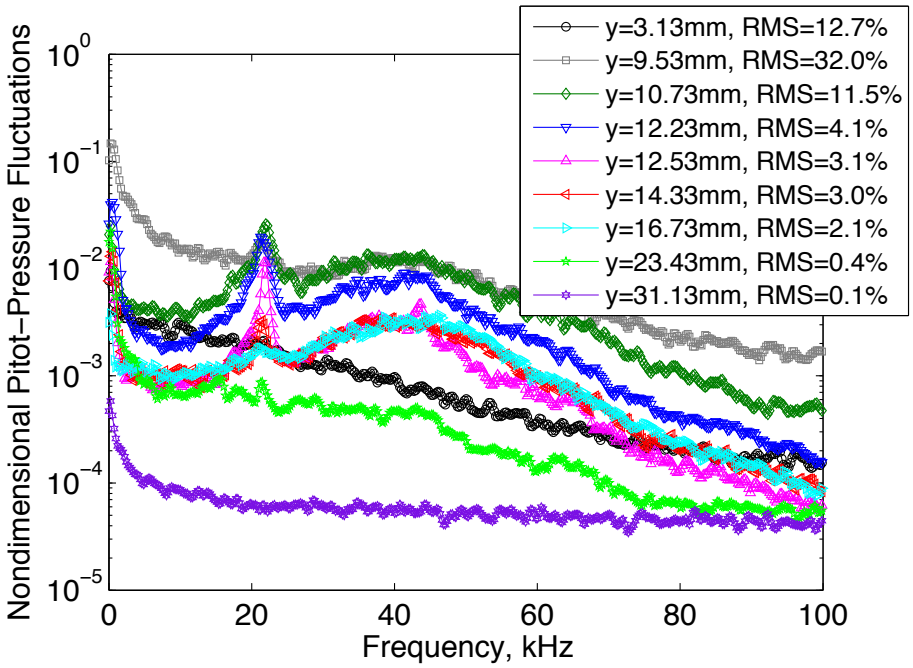

Figure 7.8. Spectra at ten roughness diameters downstream. Pitot-pressure fluctuations nondimensionalized by freestream pitot pressure.

7.5 Reynolds-Number Dependency

A test was performed to examine how the frequency of the instability depends on freestream Reynolds number. During a single run, the pitot probe was left stationary 1.2 diameters downstream and two diameters off-center from the roughness. The probe was at a height of 10.6 mm above the wall and the roughness height was 10.2 mm. In the BAM6QT, the decreasing stagnation pressure during the run causes the freestream Reynolds number to decrease. Spectra from the pressure signal were computed at several 0.05-s intervals during the run at different Reynolds numbers. The RMS from 0–100 kHz was computed as a percentage of mean pressure. Figure 7.9 shows four spectra from a run with an initial stagnation pressure of 90 psia. During the run, the instability peak frequency decreases from 22.5 kHz to 20.75 kHz. The instability frequency decreases by 8% as the Reynolds number decreases by 5%. The variation of frequency with Reynolds number suggests that the instability is real.

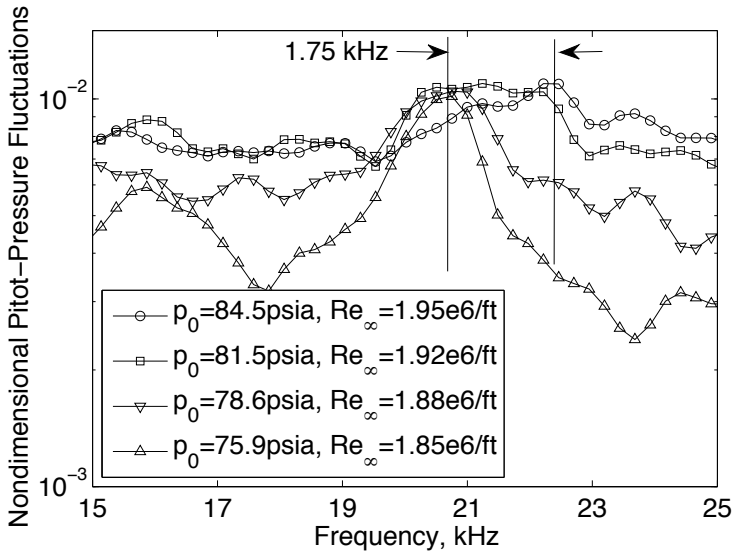

Figure 7.9. Frequency shifting of instability with Reynolds number. Measuring 1.2 diameters downstream, two diameters off-center from the roughness, and 10.6 mm above the wall. Pitot-pressure fluctuations nondimensionalized by freestream pitot pressure.

Figure 7.10 shows the same data, in addition to data from a second run with an initial stagnation pressure of 75 psia. The points in the spectra from the $p_{0,i} = 90$ psia run are denoted by circles while the point in the spectra from the $p_{0,i} = 75$ psia run are denoted by squares. At the beginning of the $p_{0,i} = 90$ psia run, the spectrum appears to be broadband, suggesting that the flow may be turbulent. At the beginning of the run, the boundary-layer height is smallest and the roughness would appear larger to the flow. As the run progresses, the 21-kHz peak becomes more pronounced and the baseline noise decreases, perhaps due to the increasing boundary-layer thickness. The RMS decreases from 6.0% to 2.8%.

During the run at $p_{0,i} = 75$ psia, the fluctuation levels decrease dramatically to a baseline level of 0.01%. At the beginning of the run, a broad peak is visible at 18–21 kHz which may be related to the 21-kHz instability. A second peak at 65 kHz also appears and is sharp with a width of 3–4 kHz. During the run as the stagnation pressure decreases, the broad 20-kHz peak disappears while the frequency of the second peak decreases. The second peak may be an additional instability within the roughness wake. No additional stagnation pressures were tested when using the Kulite pitot probe. In the future, additional runs should be performed at initial stagnation pressures between 70–100 psia, in an attempt to observe the possible second instability.

Additional experiments were performed with the calibrated hot wire. In these, a rapid decrease in the RMS mass flux was seen near $p_0 = 70$ psia. Figure 7.11 shows data from a run at $p_{0,i} = 80$ psia with the hot-wire probe positioned 10.2 mm above the wall. The measurements were taken 13 diameters downstream and two diameters off-center from the 10.2-mm roughness. The blue trace shows the contraction pressure dropping in a stairstep pattern near 69.5 psia. At $t = 2.00$ s, the mass flux RMS is 0.1% of the mean and a sharp 21-kHz peak can be seen from the instability. At $t = 2.15$ s, the RMS decreases suddenly and the 21-kHz instability decreases in amplitude. A new oscillation at 63 kHz appears, similar to that seen in the pitot-probe data in Figure 7.10. The higher-frequency oscillation observed by the pitot probe also

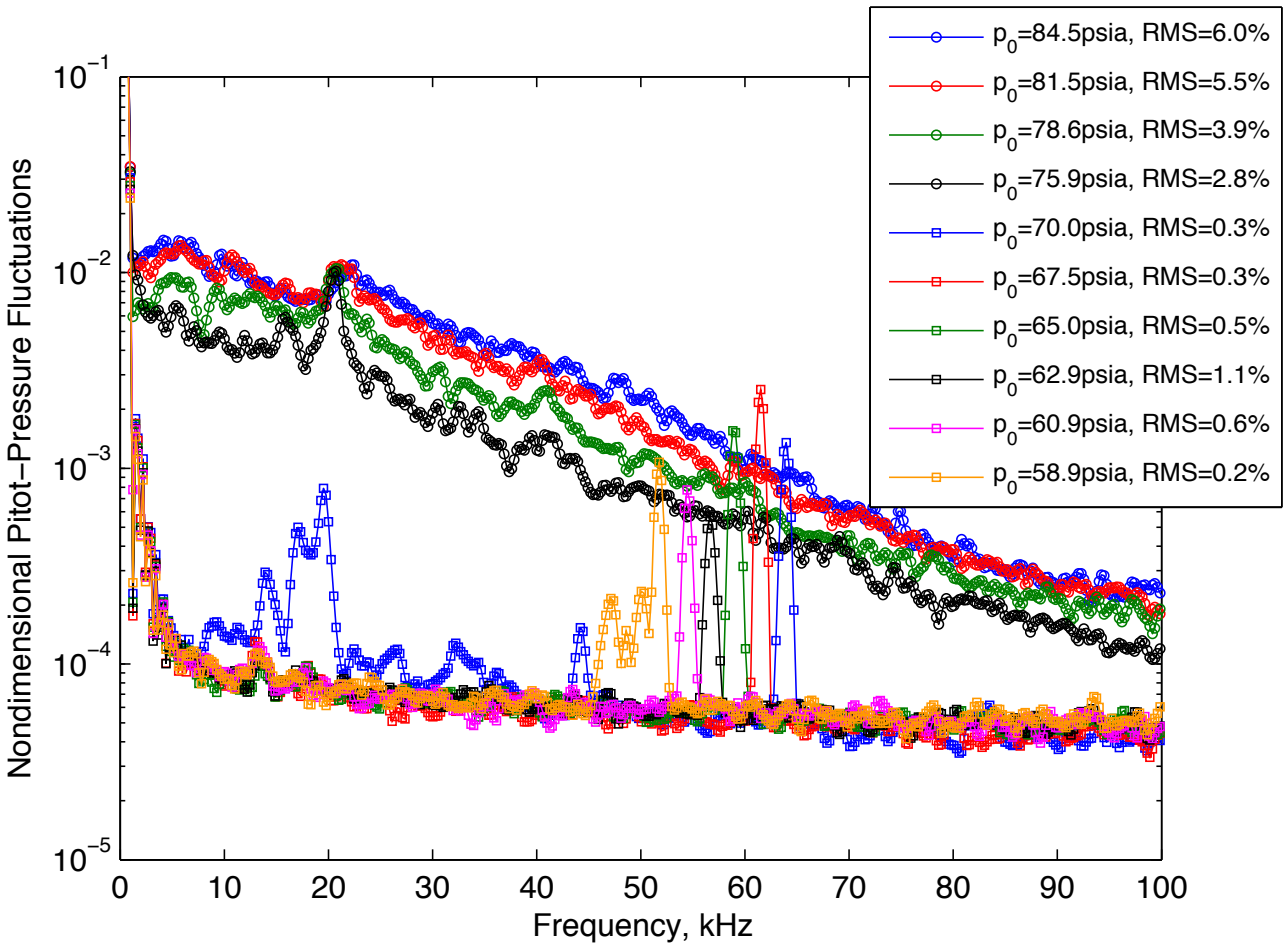

Figure 7.10. Rapid decrease in pressure fluctuations as stagnation pressure decreases. Pitot-pressure fluctuations nondimensionalized by freestream pitot pressure. Measuring 1.2 diameters downstream, two diameters off-center from the roughness, and 10.63 mm above the wall. Two separate runs. Run with $p_{0,i} = 90$ psia denoted by circles. Run with $p_{0,i} = 75$ psia denoted by squares.

appeared when the stagnation pressure dropped below 70 psia. It is possible that a small change in conditions from the dropping stagnation pressure causes a large change in the roughness wake flow. More experimentation is needed in order to draw any conclusions about a possible higher-frequency instability.

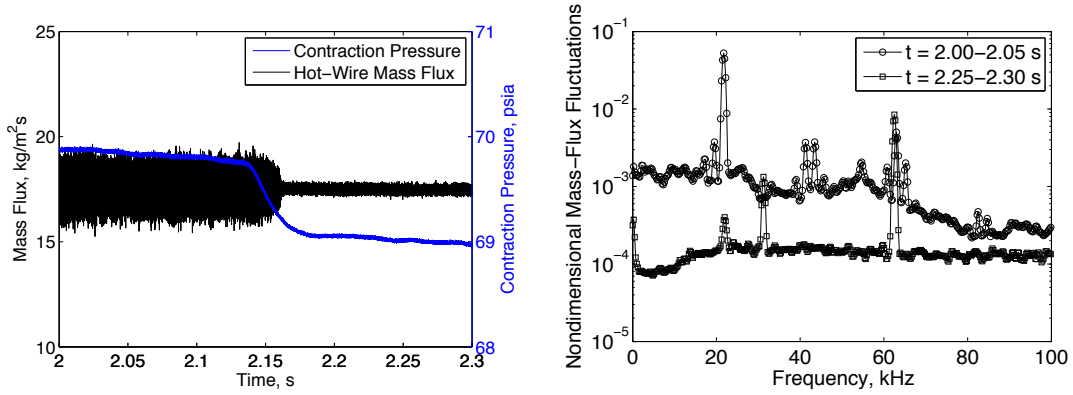

(a) Hot-wire mass flux and contraction pressure.

(b) Spectra from part (a).

Figure 7.11. Decrease in RMS and appearance of 60-kHz oscillation. Calibrated hot-wire measurements from a run with $p_{0,i} = 80$ psia, $k = 10.2$ mm, $y = 10.2$ mm, measuring 13 diameters downstream and two diameters off-center from roughness. Mass-flux fluctuations nondimensionalized by mean mass flux.

7.6 Strouhal-Number Approximation

A Strouhal-number analysis was performed and compared to the 21-kHz instability frequency in the roughness wake. The Strouhal number is a dimensionless number used to characterize vortex shedding, mainly at subsonic speeds. For high Reynolds-numbers at subsonic speeds, it can be approximated as 0.2 for a cylinder (based on the diameter). The data for vortex shedding at hypersonic speeds is limited, however the Strouhal-number analysis has been applied at high speeds [63]. Mach-number effects may significantly alter the characteristics of a blunt-body wake when compared to the

incompressible case. In this simple analysis, these effects were ignored and a Strouhal number of 0.2 was used. The equation for the Strouhal number in a cylinder wake is

$$\mathrm{St} = \frac{fD}{U_\infty} \tag{7.1}$$

where D is the cylinder diameter, f is the vortex-shedding frequency, and U_∞ is the freestream velocity. Using a Strouhal number of 0.2, the vortex-shedding frequency f was computed assuming that the cylindrical roughness was exposed only to freestream conditions. The roughness diameter $D = 0.235$ in. was used and the freestream velocity in the BAM6QT was calculated using the equation

$$U_\infty = M\sqrt{\gamma R_{\mathrm{gas}} T_\infty} \tag{7.2}$$

The resulting vortex-shedding frequency for a cylinder in Mach-6 flow was estimated at 29 kHz, suggesting that the 21-kHz instability may be vortices in the roughness wake. However, a simple Strouhal-number approximation is insufficient to classify the instability within a hypersonic boundary layer.

7.7 Downstream Growth of 21-kHz Instability

The pitot-probe data appearing in Figures 7.6–7.8 were analyzed for evidence of downstream growth of the 21-kHz instability. Several runs were performed at $p_{0,i} = 90$ psia with different initial probe heights and movement directions. The roughness height was 10.2 mm. Figure 7.12 shows the RMS from 19–23 kHz at three downstream locations using the integrated area under the power spectrum. The RMS was nondimensionalized by the freestream pitot pressure. The method used to calculate the RMS was the same as that described in Section 7.3. Two large peaks are visible more than 15 mm from the wall at five and ten diameters downstream. These peaks are near the location of the assumed shock in Figure 6.11. A shimmering shock may account for these fluctuations.

At ten diameters downstream of the roughness, the 21-kHz oscillations at $y = 10$ mm grow by a factor of two compared to 1.2 diameters downstream. However, the

RMS at five diameters downstream, near the 10.2-mm roughness height, is lower than at 1.2 diameters downstream. The instability RMS may depend on Reynolds number and the variation in Reynolds number in Figure 7.12 may prevent the observation of growth. In addition, the Kulite tended to resonate at 330 kHz with large amplitudes when measuring beyond a few diameters downstream of the roughness. Perhaps the Kulite resonance could interfere with accurate measurements of lower frequencies in the signal.

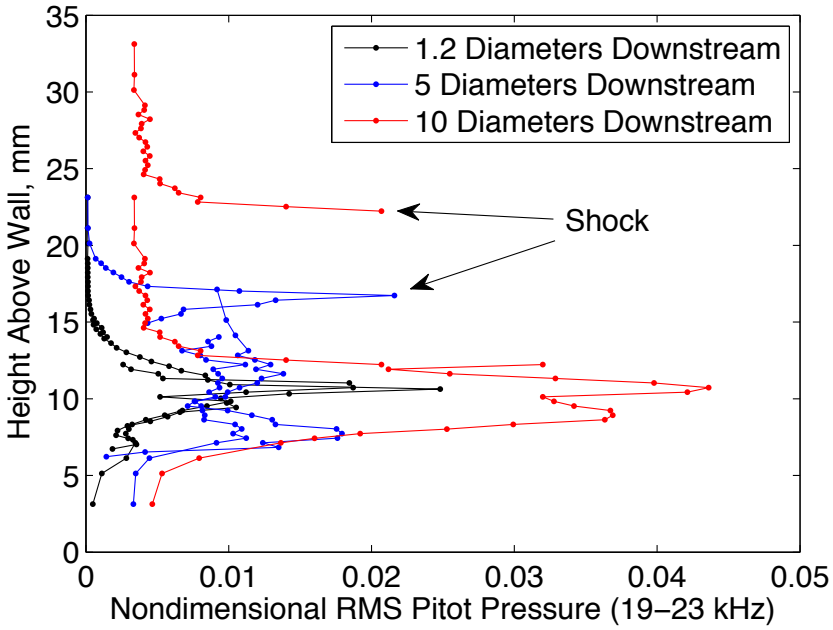

Figure 7.12. Root-mean-square pressure fluctuations in the 19–23 kHz frequency band, nondimensionalized by the theoretical freestream pitot pressure, for three downstream locations. Multiple runs with different initial heights with the probe moving in different directions, taken two diameters off the centerline.

Measurements in the wake of the $k = 10.2$ mm roughness were performed using a calibrated hot wire in an attempt to observe downstream growth of the 21-kHz instability at a constant Reynolds number. A hot-wire probe was used because the Kulite pitot probe tended to resonate with large amplitude when measuring far downstream from the roughness. In addition, the hot wire interferes less with the flow.

For the downstream measurements, runs were performed at either 90 psia or 80 psia initial stagnation pressure. The roughness was placed two diameters off-center from the hot-wire probe and set to a height of 10.2 mm. The hot wire probe was set to a height of $y = 10.2$ mm, near the peak location of the instability.

The hot wire was moved to several streamwise locations at a constant height above the wall to observe downstream growth. Several runs were performed at an initial stagnation pressure of 80 psia. Root-mean-square spectra were calculated from a similar time during the run ($t = 1.00$–1.05 s) so that the freestream conditions would be similar. The mass-flux fluctuations (per 0.24 kHz) were nondimensionalized by the mean mass flux. The 21-kHz instability was observed to grow downstream of the roughness. Figure 7.13 shows the results, with a typical pre-run background noise spectra shown for comparison. Each spectra downstream of the roughness shows a clear peak at 21 kHz. At 1.6 roughness diameters downstream, the RMS of the 21-kHz peak was 1% of the mean mass flux and the background levels were 0.1–1%. At 13 diameters downstream the RMS of the 21-kHz peak grew to 3% and the background noise levels grew higher. A peak at 65 kHz was observed at both 1.6 and 13 diameters downstream and could be a second instability. At 26.8 diameters downstream the 21-kHz peak had a RMS of 20% of the mean with higher background levels. When the probe was placed 7.6 diameters upstream of the roughness element, the spectra was similar to the pre-run values, as expected for a laminar boundary layer. There was no evidence of the 21-kHz disturbance upstream of the roughness element, suggesting that the disturbance is not likely to be vibration of the probe support.

Table 7.2 shows the RMS mass-flux fluctuations from Figure 7.13, calculated by integrating the area under the power spectrum, and nondimensionalized by the mean mass flux. When calculating the RMS using this method, the 21-kHz peak has an amplitude of 35.0% of the mean at 26.8 diameters downstream, while the total signal RMS is 43.0%.

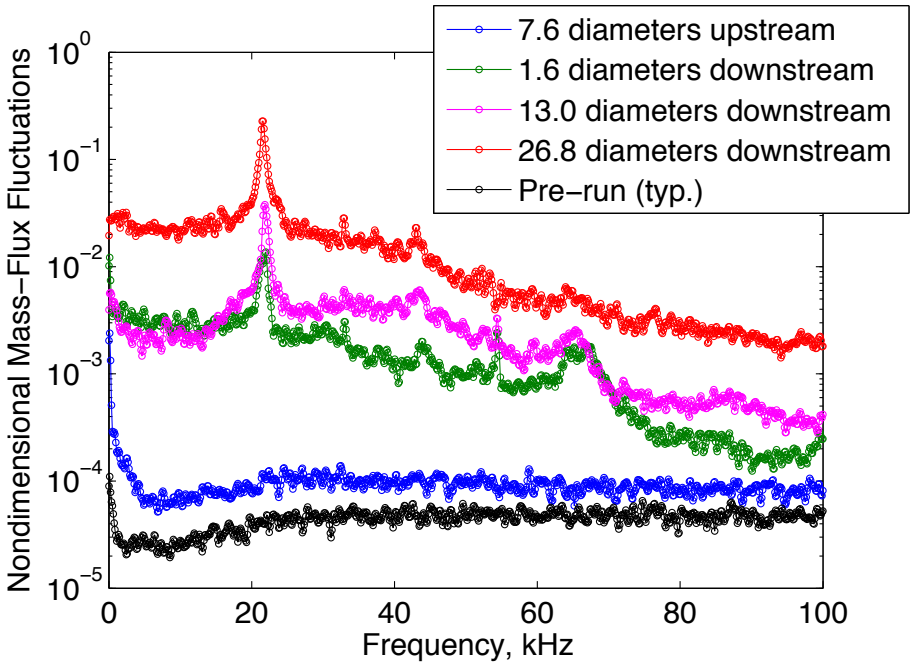

Figure 7.13. RMS spectra at a height of $y = 10.2$ mm above the wall, measuring two diameters off-center from the $k = 10.2$ mm roughness. Mass-flux fluctuations nondimensionalized by mean mass flux. All runs were at an initial stagnation pressure of 80 psia and the spectra are from $t = 1$ s during the run (p_0 =75 psia and $Re_\infty = 1.75\times10^6$/ft).

Table 7.2 RMS mass-flux fluctuations from Figure 7.13, nondimensionalized by the mean mass flux. The RMS was calculated by integrating the area under the power spectrum.

	7.6D upstream	1.6D downstream	13D	26.8D
Total (0–100 kHz)	0.2%	4.1%	7.3%	43.0%
Peak (19–23 kHz)	–	2.5%	5.4%	35.0%

7.8 Conclusions

The evidence suggests that a laminar instability has been measured in the wake of the roughness. The instability was observed using two different sensor types at similar conditions. Tests have shown that the instability is strongest off the centerline at a height near the roughness height, and disappears in the freestream. In addition, the frequency of the instability varies with Reynolds number. The instability was seen to grow to large amplitudes downstream of the roughness, with RMS values approaching 35% of the mean mass flux. Though stray effects such as shock/boundary-layer interactions have yet to be fully ruled out, this appears to be the first time that an instability has been detected in a roughness wake at hypersonic speeds.

Mean-flow and instability computations are being carried out for comparison to these experiments at UCLA and NASA Langley [64, 65]. If good agreement is obtained, both computation and experiment will be validated. The longer-term goal is to develop e^N-class methods for predicting transition in flight and in large wind tunnels, where measurements of the roughness wake and its instabilities do not appear feasible.

8. SUMMARY AND FUTURE WORK

A roughness element was installed on the nozzle wall of the Boeing/AFOSR Mach-6 Quiet Tunnel in order to make quantitative measurements of instabilities within the wake. These measurements will be used to support the development of computational methods for predicting roughness-induced transition.

Preliminary temperature-sensitive paints results were reported from the wake of the roughness on the nozzle wall. The images show that as the roughness height is increased in a laminar boundary layer, the wake region widens and several hot streaks become visible. These hot streaks may be vortices or other disturbances in the flow. The majority of the TSP images were taken at an initial tunnel stagnation pressure of 120 psia. A lower stagnation pressure was used for wake measurements to increase the hot-wire survival rate. Temperature-sensitive paint can be used to supplement future wake measurements.

The feasibility of using hot-wire and pitot probes within the wake of the roughness was explored. In order to measure closer to the roughness, a new angled probe support was constructed. The vibrational frequency of the probe support was tested and the results showed no vibrations at high frequencies that could interfere with instability measurements. It is possible that 20-Hz oscillations of the probe signal during runs at certain conditions could be a vibration. Difficulties in making wake measurements include separation of the nozzle-wall boundary layer induced by the probe support or sting-support section. However, several methods were used to reduce this separation.

Using the pitot probe and hot-wire probes, measurements of the mean flow and fluctuations within the wake of the roughness were performed while searching for instabilities. Mean-flow pitot-pressure profiles were collected for various roughness heights and can be used to compare to future computations. At a roughness height of 10.2 mm and tunnel stagnation pressures of 75–90 psia, a flow instability at 21 kHz

was discovered within the laminar boundary layer. The instability was observed using multiple sensors and the frequency was observed to vary with Reynolds number. When the roughness is removed or the probe is placed upstream of the roughness, the instability disappears. The instability is strongest off the centerline at a height near the roughness height, where a shear layer should be present, and was observed to grow downstream. Though stray effects such as vibration or shock/boundary-layer interactions have yet to be fully ruled out, the roughness-induced instability appears to be the first such instability measured at hypersonic speeds. Computations are in progress, and if agreement can be obtained the results will be validated.

Future work will include a study of the roughness-induced instability in greater detail. Measurements will be made in support of computations in order to develop a physics-based method for predicting hypersonic transition induced by an isolated roughness element.

LIST OF REFERENCES

LIST OF REFERENCES

[1] John D. Anderson, Jr. *Fundamentals of Aerodynamics*. McGraw-Hill Series in Aeronautical and Aerospace Engineering. McGraw-Hill, 3rd edition, 2001.

[2] Hermann Schlichting and Klauss Gersten. *Boundary Layer Theory*. Springer, 8th edition, 2000.

[3] Frank M. White. *Viscous Fluid Flow*. McGraw-Hill Series in Mechanical Engineering. McGraw-Hill College, 3rd edition, January 2005.

[4] T. C. Lin. Influence of Laminar Boundary-Layer Transition on Entry Vehicle Design. *Journal of Spacecraft and Rockets*, 45(2):165–175, March-April 2008.

[5] John D. Anderson, Jr. *Hypersonic and High-Temperature Gas Dynamics*. AIAA Education Series. American Institute of Aeronautics and Astronautics, Inc., 2nd edition, 2006.

[6] Steven P. Schneider. Flight Data for Boundary-Layer Transition at Hypersonic and Supersonic Speeds. *Journal of Spacecraft and Rockets*, 36(1):8–20, January-February 1999.

[7] R. Narasimha. The Laminar-Turbulent Transition Zone in the Boundary Layer. *Progress in Aerospace Sciences*, 22(1):29–80, 1985.

[8] Kenneth F. Stetson. On Predicting Hypersonic Bounday Layer Transition. Technical Report AFWAL-TM-87-160-FIMG, Flight Dynamics Laboratory, Air Force Wright Aeronautical Laboritories, Wright-Patterson Air Force Base, Ohio, March 1987.

[9] Eli Reshotko. Transition Issues for Atmospheric Entry. *Journal of Spacecraft and Rockets*, 45(2):161–164, March-April 2008.

[10] Steven P. Schneider. Effects of High-Speed Tunnel Noise on Laminar-Turbulent Transition. *Journal of Spacecraft and Rockets*, 38(3):323–333, May-June 2001.

[11] Steven P. Schneider. Development of Hypersonic Quiet Tunnels. *Journal of Spacecraft and Rockets*, 45(4):641–664, July-August 2008.

[12] Daniel C. Reda. Boundary-Layer Transition Experiments on Sharp, Slender Cones in Supersonic Free Flight. *AIAA Journal*, 17(8):803–810, August 1979.

[13] Thomas J. Juliano, Steven P. Schneider, Selin Aradag, and Doyle Knight. Quiet-Flow Ludwieg Tube for Hypersonic Transition Research. *AIAA Journal*, 46(7):1757–1763, July 2008.

[14] G. B. Schubauer and H. K. Skramstad. Laminar-Boundary-Layer Oscillations and Transition on a Flat Plate. NACA Report 909: 327-357, 1948.

[15] Leslie M. Mack. Linear Stability Theory and the Problem of Supersonic Boundary-Layer Transition. *AIAA Journal*, 13(3):278–289, March 1975.

[16] Kenneth F. Stetson and Roger L. Kimmel. On Hypersonic Boundary-Layer Stability. AIAA Paper 92-0737, January 1992.

[17] Heath B. Johnson and Graham V. Candler. Analysis of Laminar-Turbulent Transition in Hypersonic Flight Using PSE-Chem. AIAA Paper 2006-3057, June 2006.

[18] A. M. O. Smith and Nathalie Gamberoni. Transition, Pressure Gradient and Stability Theory. Douglas Aircraft Company Report No. ES 26388, August 1956.

[19] J.L. van Ingen. The e^N method for transition prediction. Historical review of work at TU Delft. AIAA Paper 2008-3830, June 2008.

[20] Heath B. Johnson, Chris R. Alba, Graham V. Candler, Matthew MacLean, Timothy Wadhams, and Michael Holden. Boundary-Layer Stability Analysis of the Hypersonic International Flight Research Transition Experiments. *Journal of Spacecraft and Rockets*, 45(2):228–236, March-April 2008.

[21] N. A. Jaffe, T. T. Okamura, and A. M. O. Smith. Determination of Spatial Amplification Factors and Their Application to Predicting Transition. *AIAA Journal*, 8(2):301–307, February 1970.

[22] Steven P. Schneider. Effects of Roughness on Hypersonic Boundary-Layer Transition. *Journal of Spacecraft and Rockets*, 45(2):193–209, March-April 2008.

[23] Scott A. Berry, Aaron H. Auslender, Arthur D. Dilley, and John F. Calleja. Hypersonic Boundary-Layer Trip Development for Hyper-X. *Journal of Spacecraft and Rockets*, 38(6):853–864, November-December 2001.

[24] Matthew P. Borg and Steven P. Schneider. Effect of Freestream Noise on Roughness-Induced Transition for the X-51A Forebody. *Journal of Spacecraft and Rockets*, 45(6):1106–1116, November-December 2008.

[25] Scott A. Berry and Thomas J. Horvath. Discrete-Roughness Transition for Hypersonic Flight Vehicles. *Journal of Spacecraft and Rockets*, 45(2):216–227, March-April 2008.

[26] Daniel C. Reda. Review and Synthesis of Roughness-Dominated Transition Review and Synthesis of Roughness-Dominated Transition Correlations for Reentry Applications. *Journal of Spacecraft and Rockets*, 39(2):161–167, March-April 2002.

[27] National Aeronautics and Space Administration. *Photo ISS011-E-11074, Cropped*, July 2005 (accessed August 13, 2009). `http://spaceflight.nasa.gov/gallery/images/station/crew-11/html/iss011e11074.html`.

[28] National Aeronautics and Space Administration. *Photo S114-E-6215, Cropped*, July 2005 (Accessed September 14, 2009). `http://spaceflight.nasa.gov/gallery/images/shuttle/sts-114/html/s114e6215.html`.

[29] Katya M. Casper, Brad M. Wheaton, Heath B. Johnson, and Steven P. Schneider. Effect of Freestream Noise on Roughness-Induced Transition at Mach 6. AIAA Paper 2008-4291, June 2008.

[30] E. R. Van Driest and W. D. McCauley. The Effect of Controlled Three-Dimensional Roughness on Boundary-Layer Transition at Supersonic Speeds. *Journal of the Aerospace Sciences*, 27(4):261–271,303, April 1960.

[31] H. Harris Hamilton, II, Daniel R. Millman, and Robert B. Greendyke. Finite-Difference Solution for Laminar or Turbulent Boundary Layer Flow over Axisymmetric Bodies with Ideal Gas, CF4, or Equilibrium Air Chemistry. NASA Technical Paper 3271, December 1992.

[32] M. S. Acarlar and C. R. Smith. A Study of Hairpin Vortices in a Laminar Boundary Layer. Part 1. Hairpin Vortices Generated by a Hemisphere Protuberance. *Journal of Fluid Mechanics*, 175:1–41, 1987.

[33] Allen H. Whitehead. Flow Field and Drag Characteristics of Several Boundary-Layer Tripping Elements in Hypersonic Flow. Technical Report TN D-5454, NASA Langley Research Center, October 1969.

[34] Paul M. Danehy, Brett Bathel, Christopher Ivey, Jennifer A. Inman, and Stephen B. Jones. NO PLIF Study of Hypersonic Transition over a Discrete Hemispherical Roughness Element. AIAA Paper 2009-394, January 2009.

[35] P. S. Klebanoff, W. G. Cleveland, and K. D. Tidstrom. On the Evolution of a Turbulent Boundary Layer Induced by a Three-Dimensional Roughness Element. *Journal of Fluid Mechanics*, 237:101–187, 1992.

[36] Meelan Choudhari, Fei Li, and Jack Edwards. Stability Analysis of Roughness Array Wake in a High-Speed Boundary Layer. AIAA Paper 2009-0170, January 2009.

[37] F. Gokhan Ergin and Edward B. White. Unsteady and Transitional Flows Behind Roughness Elements. *AIAA Journal*, 44(11):2504–2514, November 2006.

[38] Chau-Lyan Chang and Meelan M. Choudhari. Hypersonic Viscous Flow over Large Roughness Elements. AIAA Paper 2009-0173, January 2009.

[39] Steven P. Schneider and Thomas J. Juliano. Laminar-Turbulent Transition Measurements in the Boeing/AFOSR Mach-6 Quiet Tunnel. AIAA Paper 2007-4489, June 2007.

[40] Brad M. Wheaton, Thomas J. Juliano, Dennis C. Berridge, Amanda Chou, Peter L. Gilbert, Katya M. Casper, Laura E. Steen, Steven P. Schneider, and Heath B. Johnson. Instability and Transition in the Mach-6 Quiet Tunnel. AIAA Paper 2009-3559, June 2009.

[41] Erick O. Swanson. *Boundary-Layer Transition on Cones at Angle of Attack in a Mach-6 Quiet Tunnel*. PhD thesis, Purdue University School of Aeronautics & Astronautics, West Lafayette, IN, August 2008.

[42] Craig R. Skoch. Final Assembly and Initial Testing of the Purdue Mach-6 Quiet-Flow Ludwieg Tube. Master's thesis, Purdue University School of Aeronautics & Astronautics, West Lafayette, IN, August 2001.

[43] Michael J. Hannon, Jr. Evaluation of Diffuser Modifications for the Boeing/AFOSR Mach-6 Quiet Tunnel. Master's thesis, Purdue University School of Aeronautics & Astronautics, West Lafayette, IN, August 2008.

[44] Steven P. Schneider. Design of a Mach-6 Quiet-flow Wind Tunnel Nozzle using the e**N Method for Transition Estimation. AIAA Paper 1998-0547, January 1998.

[45] Erick O. Swanson. Mean Flow Measurements and Cone Flow Visualization at Mach 6. Master's thesis, Purdue University School of Aeronautics & Astronautics, West Lafayette, IN, December 2002.

[46] Thomas J. Juliano, Rodrigo Segura, Matthew P. Borg, Katya Casper, Michael J. Hannon, Jr., Brad M. Wheaton, and Steven P. Schneider. Starting Issues and Forward-Facing Cavity Resonance in a Hypersonic Quiet Tunnel. AIAA Paper 2008-3735, June 2008.

[47] Steven P. Schneider. Initial Shakedown of the Purdue Mach-6 Quiet-Flow Ludwieg Tube. AIAA Paper 2000-2592, June 2000.

[48] T. Liu and J.P. Sullivan. *Pressure and Temperature Sensitive Paints*. Springer, 2005.

[49] Jimmy Wayne Crafton. *The Impingement of Sonic and Sub-Sonic Jets onto a Flat Plate at Inclined Angles*. PhD thesis, Purdue University School of Aeronautics & Astronautics, West Lafayette, IN, December 2004.

[50] B.T. Campbell, T. Liu, and J.P. Sullivan. Temperature Sensitive Fluorescent Paint Systems. AIAA Paper 94-2483, June 1994.

[51] Tianshu Liu, Zemin Cai, Jianhuang Lai, Justin Rubal, and John P. Sullivan. Analytical Methods for Determination of Heat Transfer Fields from Temperature Sensitive Paint Measurements in Hypersonic Tunnels. AIAA Paper 2009-736, January 2009.

[52] E. F. Spina and C. B. McGinley. Constant Temperature Anemometry in Hypersonic Flow: Critical Issues and Sample Results. *Experiments in Fluids*, 17(6):365–374, 1994.

[53] Virgil A. Sandborn. *Resistance Temperature Transducers*. Metrology Press, 1972.

[54] Mark V. Morkovin. *Fluctuations and Hot-Wire Anemometry in Compressible Flows*. Number 24 in AGARDograph. North Atlantic Treaty Organization, Advisory Group for Aeronautical Research and Development, November 1956.

[55] Shann J. Rufer and Steven P. Schneider. Hot-Wire Measurements of Instability Waves on a Blunt Cone at Mach-6. AIAA Paper 2005-5137, June 2005.

[56] Shann J. Rufer. *Hot-Wire Measurements of Instability Waves on Sharp and Blunt Cones at Mach 6*. PhD thesis, Purdue University School of Aeronautics & Astronautics, West Lafayette, IN, December 2005.

[57] Craig R. Skoch, Steven P. Schneider, and Matthew P. Borg. Disturbances from Shock/Boundary Layer Interactions Affecting Upstream Hypersonic Flow. AIAA Paper 2005-4897, June 2005.

[58] Thomas J. Juliano, Erick O. Swanson, and Steven P. Schneider. Transition Research and Improved Performance in the Boeing/AFOSR Mach-6 Quiet Tunnel. AIAA Paper 2007-0535, January 2007.

[59] Craig R. Skoch. *Disturbances from Shock/Boundary Layer Interactions Affecting Upstream Hypersonic Flow*. PhD thesis, Purdue University School of Aeronautics & Astronautics, West Lafayette, IN, December 2005.

[60] I. Beckwith, F. Chen, S. Wilkinson, M. Malik, and D. Tuttle. Design and Operational Features of Low-Disturbance Wind Tunnels at NASA Langley for Mach Numbers from 3.5 to 18. AIAA Paper 90-1391, June 1990.

[61] M. V. Morkovin and W. S. Bradfield. Probe Interference in Measurements in Supersonic Laminar Boundary Layers. *Journal of the Aeronautical Sciences*, 21:785–787, November 1954.

[62] James M. Kendall, Jr. An Experimental Investigation of Leading-Edge Shock-Wave-Boundary-Layer Interaction at Mach 5.8. *Journal of the Aeronautical Sciences*, 24:47–56, January 1957.

[63] J. A. Fay and A. Goldburg. Unsteady Hypersonic Wake behind Blunt Bodies. *AIAA Journal*, 1(10):2264–2272, October 1963.

[64] Patrick T. Greene, Jeff D. Eldredge, Xiaolin Zhong, and John Kim. A Numerical Study of Purdue's Mach 6 Tunnel with a Roughness Element. AIAA Paper 2009-174, January 2009.

[65] Chau-Lyan Chang, Meelan M. Choudhari, and Fei Li. Numerical Computations of Hypersonic Boundary-Layer over Surface Irregularities. AIAA Paper 2010-1572, submitted for publication, 48th AIAA Aerospace Science Meeting, January 2010.

APPENDICES

A. Signal Acquisition and Processing Methods

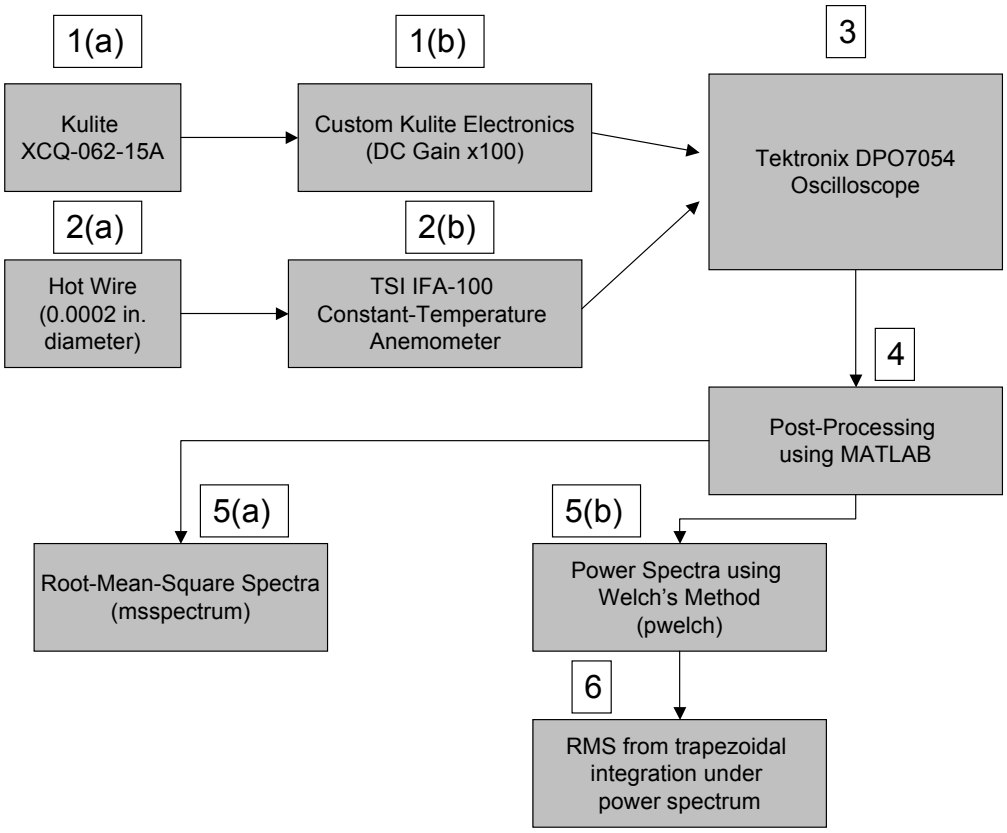

Figure A.1. Diagram showing signal processing methods.

A diagram showing the signal processing methods used in this project appears in Figure A.1. The diagram shows both probe types: the Kulite pitot probe (1) and the hot-wire probe (2), though the probes were not used simultaneously. A summary of the methods used for signal acquisition and processing appears below:

1. Kulite Pitot Probe
   - (a) Kulite XCQ-062-15A Sensor. This sensor was mounted in the pitot probe and inserted into the flow. It has a range of 0–15 psia.

- (b) Custom Kulite electronics. Custom electronics are used to power the Kulite sensors. For this project, the DC voltage output was used. The DC voltage amplifies the Kulite signal with a gain of 100 using a Burr-Brown INA103 amplifier chip. A BNC cable was then used to connect the signal to the oscilloscope.

2. Hot Wire

   - (a) Hot Wire. The wire in all cases had a 0.0002-in. diameter.
   - (b) TSI IFA-100 Constant-Temperature Anemometer. The hot wire was connected to the anemometer and the 1:1 bridge was used. A control resistor was used to "set" the wire temperature, and the resistance ratio between the control resister and probe resistance was chosen to be 1.7–1.9, as recommended by Rufer [56]. To record data, the output voltage of the anemometer was connected via a BNC cable to the oscilloscope.

3. Tektronix DPO7054 Oscilloscope. Data were sampled at 2.0 MHz in Hi-Res mode. Hi-Res mode is a method of digital filtering in which the scope samples at its maximum sampling frequency of 500 MHz and digitally averages on the fly to the desired sampling frequency of 2.0 MHz (averaging 250 points per data point). This mode effectively acts as a low-pass filter to eliminate signal aliasing. In addition, Hi-Res mode decreases noise and increases the number of vertical bits of resolution (from 8 to roughly 12–13). Assuming 12 bits of vertical resolution, the resolution of the Kulite for the typical vertical resolution setting of 200 mV/div was 0.00086 psia, or 0.003% of the freestream pitot pressure at $p_0 = 90$ psia. When the vertical resolution was increased to a maximum of 2.0 V/div due to sensor resonance, the Kulite resolution was 0.0086 psia, or 0.032% of the freestream pitot pressure at $p_0 = 90$ psia.

4. MATLAB Post-Processing. MATLAB was used for all post-processing of data. The Tektronix waveform files were converted to MATLAB variables using *tekread.m*. See `http://cobweb.ecn.purdue.edu/~aae520/tekread_primer.pdf` for more

details. A calibration was then applied. The probe data were separated into 0.05-s samples of 100,000 points each. The 0.05-s sample time was the time during which the probe was stationary when using the traverse system. Mean pitot pressures and hot-wire mass fluxes were calculated from the mean of the 100,000-point samples.

5. Spectral Analyses. Prior to performing a spectral analysis, the signal mean value was subtracted from the 100,000-point sample.

   - (a) Root-Mean-Square Spectra. All plotted spectra in this project were root-mean-square spectra in order to provide a quantitative amplitude on the vertical axis. Each spectrum was computed from the 0.05-s sample (see Appendix B.4 for the MATLAB code). Blackman windows with 5,000 points and 50% overlap were used, resulting in a total of 30 windows from the 100,000-point sample. The spectral amplitudes represent the RMS of the signal over the frequency bands, and thus the amplitudes vary depending on the frequency spacing Δf. All spectra were computed to achieve a frequency spacing Δf of 0.24 kHz. A more representative RMS was obtained by integrating the area under the power spectrum of the signal (see 6).
   - (b) Power Spectra. The power spectral density was computed from the 100,000-point sample using Welch's method (the MATLAB *pwelch* program). Again, windows with 5,000 points were used with 50% overlap, resulting in 30 total windows. The frequency spacing was 0.24 kHz. The units of amplitude for the power spectra were psia^2/Hz or $(\text{kg/s-m}^2)^2/\text{Hz}$.

6. RMS calculated from the Power Spectra. The RMS was calculated by numerically integrating the area under the power spectrum. The area under the spectrum for frequency bands of interest was integrated using trapezoidal integration (the MATLAB *trapz* function). The integration resulted in the power of the frequency band in psia^2 or $(\text{kg/s-m}^2)^2$. The square root of that number gave the RMS of the frequency band.

B. MATLAB Codes

B.1 Temperature-Sensitive Paint Analysis

B.1.1 TSP Main Code

```
% Close all figures and clear all variables
clc;
close all;
clear all;
% Add directory to path
run=2;
image=7;
directory=['D:\_DATA\Roughness\2008_2\Seattle Paper\Run',num2str(run)];
addpath(directory);

% load images:
file = ['onoff',num2str(image),'.tif'];
% find coefficients cp1 and cp2
[cp1 cp2] = tiffread(file);
% load ISSI tif file (unt16 format)
ratio = imread(file);
% Switch to double precision
ratio = double(ratio);
% Convert using coefficients from ISSI tif file:
ratio = (ratio-cp1)./cp2;
%ratio = 1./ratio; % If using OMS Lite!
% apply temperature calibration:
coef = [-0.0859 0.0118 1.0746];
ratio = coef(1).*ratio.^2 + coef(2).*ratio + coef(3);
ratio = ratio*Tref;
% set color scale:
```

```
a=[300 301.8];
% plot results:
imagesc(ratio((40:420),(1:740)),a)
colormap(jet(256))
c = colorbar('fontsize', 10, 'location', 'EastOutside');
ylabel(c,'Temperature (K)', 'Rotation',270.0, 'VerticalAlignment',
    'bottom')
axis('image')
xlabel('Distance Downstream from Roughness (in)');
ylabel('Distance from Centerline (in)');
set(gca,'XTick',[103, 213, 324, 433, 544,
    654],'XTickLabel',['21.3';'19.3';'17.3';'15.3';'13.3';'11.3']) ;
set(gca,'YTick',[35, 118, 198, 278,
    361],'YTickLabel',['3.0';'1.5';'0.0';'1.5';'3.0']) ;
set(gca,'XDir','reverse','TickDir','in')
grid on;
set(gca,'gridlinestyle','-');

%
% Make line plots of temperature at four streamwise locations:
%
ratio = ratio((40:420),:);
% Correlate pixels to inches:
xcorr = polyfit([103, 213, 324, 433, 544, 654],[21.3 19.3 17.3 15.3 13.3
     11.3],1);
ycorr = polyfit(fliplr([35, 118, 198, 278, 361]),[3 1.5 0 -1.5 -3],1);
for i = 1:381
    centerlinedistance(i)=polyval(ycorr,i);
end

figure;
% Pixel values to plot:
xvalues = [694  490  268  49];
for i = 1:length(xvalues)
        x = xvalues(i);
```

```
        average=zeros(1,381);
        for j = 2:380
            average(j) = mean(mean(ratio((j-1):(j+1),(x-15):(x+15))));
        end
        if i == 1
            plot(centerlinedistance,average,'-ok');
        elseif i == 2
            plot(centerlinedistance,average,'-sr');
        elseif i == 3
            plot(centerlinedistance,average,'-db');
        elseif i == 4
            plot(centerlinedistance,average,'-^g');
        end
        hold on;
end
d=polyval(xcorr,xvalues)
axis([-3 3 299.9 302.5]);
legend([num2str(d(1),'%2.1f') ' in.'],[num2str(d(2),'%2.1f') '
   in.'],[num2str(d(3),'%2.1f') ' in.'],[num2str(d(4),'%2.1f') '
   in.'],'location','northwest');
xlabel('Distance from Centerline, in.','fontsize',14);
ylabel('Temperature, K','fontsize',14);
set(gca,'fontsize',14);
grid on;
%Remove directory from path
rmpath(directory);
```

B.1.2 Function tiffread.m

```
% tiffread.m
% Brad Wheaton
% 5/29/2008
% Function to read the coefficients cp1 and cp2 from the ISSI tiff
   files.
% Input the ISSI TIFF file. The function will read the image
% information as a string, for example 'f=filename.tif m=0 a=0 b=0
% cp1=-37890.5 cp2=52517.2' and extract the coefficients.
%
% Use the coefficients to convert the uint16 TIFF file to double with
% the following code:
%
%     % load ISSI tif file (unt16 format)
%     ratio = imread(file);
%     % Switch to double precision
%     ratio = double(ratio);
%     % Convert using coefficients from ISSI tif file:
%     ratio = (ratio-cp1)./cp2;
%     ratio = 1./ratio; % If using OMS Lite!

function [cp1 cp2] = tiffread(filename)
imageinfo = imfinfo(filename); % get image information
imgdesc = imageinfo.ImageDescription; % read image description from
   structure
% read text from image header, ignore all strings, return just cp1 and
   cp2
% as floating point data:
C = textscan(imgdesc,'%*s %*s %*s %*s %4*s %f %4*s %f');
cp1 = C{1,1}; % get cp1 from cell array
cp2 = C{1,2}; % get cp2 from cell array
```

B.2 Probe Position Estimation

The following codes were used to calculate the streamwise position and height above the wall of the Kulite pitot probe and hot-wire probes. The codes call a function "tunnelradius.m" which outputs the radius of the nozzle for a given streamwise position.

B.2.1 Kulite Pitot Probe

```
clear all;
clc;
close all;
% probeheight_kulite.m
% Modified 2/12/09
% Program to compute the z-location of the probe as well as the height
% above the wall of the probe when referenced using a jo block.

% inputs:
rulerreading = 163; % traverse ruler position in mm
joblockheight = 0.111; % in in.
joblockwidth = .359; % in in.

% z location in inches:
rulerreading = rulerreading*0.0393700787; % convert to in.
% angled probe support with Kulite: 155mm on ruler = 0.27in behind
   roughness back = 0.27+0.235/2in from roughness centerline
zfromroughnesscenter = 0.27 +.235/2 + rulerreading - 6.1023622
zfromroughnessback = 0.27 + rulerreading - 6.1023622
zfromroughnessback_diameter = zfromroughnessback/0.235
zprobe = zfromroughnesscenter + 75.749

% Kulite probe height when heel is contacting center of jo block:
zprobeheel = zprobe+0.642*sin(4.58*pi/180); % z-location of heel
rprobeheel = tunnelradius(zprobeheel);
```

```
% now find height between tunnel wall and jo block bottom using that
    radius:
theta = asin(joblockwidth/2/rprobeheel); % angle between center of block
     and edge of block
yjoblockbottom = rprobeheel-rprobeheel*cos(theta);
% height of jo block top:
yjoblocktop = yjoblockbottom + joblockheight;
% height of probe when heel contacting
yprobe_inch = yjoblocktop + tunnelradius(zprobe)- rprobeheel + 0.11356
    % tunnel radius differences, height of jo block, and 0.11356 to
    account for height of sensor above heel
yprobe_mm = yprobe_inch*25.4
```

B.2.2 Hot-Wire Probe

```
clear all;
clc;
close all;
% probeheight_hotwire.m
% Modified 5/5/09
% Program to compute the z-location of the probe as well as the height
% above the wall of the probe when referenced using a jo block.

% inputs:
rulerreading = 155; % traverse ruler position in mm
joblockheight = 0.105; % in in.
joblockwidth = 0.350; % in in.

% z location in inches:
rulerreading = rulerreading*0.0393700787; % convert to in.
% angled probe support with hot wire: 152mm on ruler = 0.27in behind
    roughness back = 0.27+0.235/2in from roughness centerline
zfromroughnesscenter = 0.27 + .235/2 + rulerreading - 152*0.0393700787;
zfromroughnessback = 0.27 + rulerreading - 152*0.0393700787;
```

```
zfromroughnessback_diameter = zfromroughnessback/0.235
zprobe = zfromroughnesscenter + 75.749

% Hot wire probe height when heel is contacting center of jo block:
zprobeheel = zprobe+0.690; % z-location of heel, 0.690 in. downstream
   from wire
rprobeheel = tunnelradius(zprobeheel);
% now find height between tunnel wall and jo block bottom using that
   radius:
theta = asin(joblockwidth/2/rprobeheel); % angle between center of block
    and edge of block
yjoblockbottom = rprobeheel-rprobeheel*cos(theta);
% height of jo block top:
yjoblocktop = yjoblockbottom + joblockheight;
% height of probe when heel contacting jo block:
yprobe_inch = yjoblocktop + tunnelradius(zprobe)- rprobeheel - 0.024 %
   tunnel radius differences, height of jo block, and -0.024 to account
    for height of sensor above heel
yprobe_mm = yprobe_inch*25.4
```

B.3 Traverse Motion Profile Analysis

```
% Traverse Profile Code
% Brad Wheaton
% Modified 2/10/09
% Generates t2use and y2use, where "t" represents the ending time
% of the hold at each step
clc;
clear all;
close all;
% inputs:
runendtime = 2.9; % shutdown time as indicated on hot films
% traverse settings (5 mm/rev):
delay = 0.4; % delay time for traverse movement in seconds
```

```
v=60; % rev/s (maximum speed 50rev/s)
a=60; % rev/s (assumes acceleration and deceleration are same)
stepsizevalues=[.3*ones(1,25)]; % step size in mm
holdtime=0.05; % hold time in seconds
% hot wire initial position:
y_i = 12+3.127; % initial hot wire position in mm
movedirection = -1; % 1 for up, -1 for down
%
% CALCULATE TIME AND DISTANCE... DO NOT MODIFY
%
% convert to mm/s:
v=v*5;
a=a*5;
% Calculate movement time, determining if full speed is actually
    reached:
% check time it takes to accelerate to full speed (v = v0 + a*t):
time_accel = v/a;
% now calculate distance moved during that time
% (x = x0 + v0*t + 0.5*a*t^2):
distance_accel = .5*a*time_accel^2;
% this value should not be greater than half of the step size if
    velocity is to be used calculate time and distance at each segment
    (time will be the end of the hold):
y = y_i; % initial y position
t = delay; % initial time delay
for i = 1:length(stepsizevalues)
    stepsize=stepsizevalues(i);
    if distance_accel >= stepsize/2
        velocity_reached = 0; % max velocity IS NOT reached
        movetime = 2*sqrt((stepsize/2)/(0.5*a));
        % t = sqrt((x-x0)/(0.5*a))
    else
        velocity_reached = 1; % max velocity IS reached
        distance_atmaxvelocity = stepsize - 2*distance_accel;
```

```
        % distance moved at max velocity, not counting acceleration and
           deceleration
        time_atmaxvelocity = distance_atmaxvelocity/v;
        % time spent at max velocity
        movetime = time_atmaxvelocity + 2*time_accel;
    end
    t = t + movetime + holdtime; % current time
    y = y + movedirection*stepsize; % current position
    t2use(i) = t; % record current time
    y2use(i) = y; % record current position
    % make sure data is only during run:
    if t < runendtime
        istop=i;
    end
end
t2use = [delay t2use(1:istop)]; % cut off time to only during run
y2use = [y_i y2use(1:istop)]; % cut off position to only during run

%%
% PLOT position vs time
for i = 2:2:2*length(t2use)
    y2usenew(i-1) = y2use(i/2);
    y2usenew(i) = y2use(i/2);
    t2usenew(i-1) = t2use(i/2)-holdtime;
    t2usenew(i) = t2use(i/2);
end
y2usenew = [y2usenew(1) y2usenew];
t2usenew = [t2usenew(1)-delay t2usenew];
figure(3);
grid on;
hold on;
plot(t2usenew,y2usenew,'-');
ylabel('Position (mm)');
xlabel('Time (seconds)');
grid on;
```

B.4 Mean-Squared Spectrum Function

```
% BRAD WHEATON, 1/30/09
function [pmss fmss] = fft_mss(x, window, percentoverlap, nfft, Fs)
% Function using the msspectrum command to give RMS of a signal vs.
    frequency. The msspectrum command returns units^2 for power. This
    function takes the square root of that.
% INPUTS:
% x is the signal
% window is the number of points to include in each segment for the
    FFT's
% percentoverlap is the percentage overlap of each window
% nfft is the number of points in the FFT.
% Fs is the sampling frequency
% OUTPUTS:
% p is the RMS in units^1 (psia) or (V).
% f is the vector of frequencies

hp = spectrum.welch('Blackman',window,percentoverlap);
% H = SPECTRUM.WELCH(WINNAME,SEGMENTLENGTH,OVERLAPPERCENT)
%  Creates a handle used to pass a welch estimator to the msspectrum
    function, using a Blackman window

hpopts = psdopts(hp,x); % Create PSD object
set(hpopts,'Fs',Fs,'nfft',nfft); % sets sampling frequency and number of
     FFT points in PSD options

hmss = msspectrum(hp,x,hpopts); % Returns a DSP data object (dspdata) in
     Hmss that contains the mean-square (power) estimate of the
    discrete-time signal vector X estimated using the MSS estimator
    specified in the handle hp. The mean-square spectrum contained in
    the object Hmss is the distribution of power over frequency. For
    real signals, MSSPECTRUM returns the one-sided mean-square spectrum
    by default; Note that a one-sided mean-square spectrum contains the
    total power of the input signal. The mean-squared spectrum is
```

```
    intended for discrete spectra. Unlike the power spectral density
    (PSD), the peaks in the mean-square spectrum reflect the power in
    the signal at a given frequency.

pmss = hmss.Data; % Extract the RMS vector from the data object
    (units^2)
fmss = hmss.Frequencies; % Extract the frequencies vector from the data
    object
pmss = sqrt(pmss); % Take the square root such that the units are
    units^1
```

B.5 Reynolds Number Calculation

```
function [Re_ft T0] = re_ft(p0, p0_init, M)
% p0, p0_init in psia
% M is Mach number, 6 for quiet flow and 5.8 for noisy flow

g = 1.4; % ratio of specific heats
R = 287; % J / kg K
T0_init = 433; % K

p0 = p0 .* 101325 ./ 14.7; % Pa
p0_init = p0_init .* 101325 ./ 14.7; % Pa
T0 = T0_init*(p0/p0_init)^((g-1)/g);  % K
p = p0 ./ (1+(g-1)/2*M.^2).^(g/(g-1)); % Pa
T = T0 ./ (1+(g-1)/2*M.^2); % K
mu = 0.00001716 .* (T./273).^(3/2) .* (384./(T+111)); % Sutherland's law

Re_m = p .* M ./ mu .* sqrt(g ./ (R.*T)); % per meter
Re_ft = Re_m*.3048; % per foot
```

C. Equipment Information

C.1 Roughness Height Tables

The micrometer-head settings for various roughness heights are summarized in Table C.1. The settings were determined by adjusting the micrometer head to minimize the step when $k = 0$ in. The "left" and "right" positions are the defined with the roughness installed on the lower wall of the tunnel, looking from upstream to downstream.

Table C.1: Roughness micrometer-head settings

k (in)	Center Position (in)	Left Position (in)	Right Position (in)
0	0.957	0.955	0.967
0.02	0.937	0.935	0.947
0.04	0.917	0.915	0.927
0.06	0.897	0.895	0.907
0.08	0.877	0.875	0.887
0.1	0.857	0.855	0.867
0.12	0.837	0.835	0.847
0.14	0.817	0.815	0.827
0.16	0.797	0.795	0.807
0.18	0.777	0.775	0.787
0.2	0.757	0.755	0.767
0.22	0.737	0.735	0.747
0.24	0.717	0.715	0.727
0.26	0.697	0.695	0.707
0.28	0.677	0.675	0.687
0.3	0.657	0.655	0.667
0.32	0.637	0.635	0.647
0.34	0.617	0.615	0.627
0.36	0.597	0.595	0.607
0.38	0.577	0.575	0.587
0.4	0.557	0.555	0.567
0.42	0.537	0.535	0.547
0.44	0.517	0.515	0.527
0.46	0.497	0.495	0.507

Continued on next page

k (in)	Center Position (in)	Left Position (in)	Right Position (in)
0.48	0.477	0.475	0.487
0.5	0.457	0.455	0.467
0.52	0.437	0.435	0.447
0.54	0.417	0.415	0.427
0.56	0.397	0.395	0.407
0.58	0.377	0.375	0.387
0.6	0.357	0.355	0.367
0.62	0.337	0.335	0.347
0.64	0.317	0.315	0.327
0.66	0.297	0.295	0.307
0.68	0.277	0.275	0.287
0.7	0.257	0.255	0.267
0.72	0.237	0.235	0.247
0.74	0.217	0.215	0.227
0.76	0.197	0.195	0.207
0.78	0.177	0.175	0.187
0.8	0.157	0.155	0.167
0.82	0.137	0.135	0.147
0.84	0.117	0.115	0.127
0.86	0.097	0.095	0.107
0.88	0.077	0.075	0.087
0.9	0.057	0.055	0.067
0.92	0.037	0.035	0.047
0.94	0.017	0.015	0.027

C.2 Part Drawings

Drawings of the angled probe support and roughness insert appear in Figures C.1 and C.2, respectively.

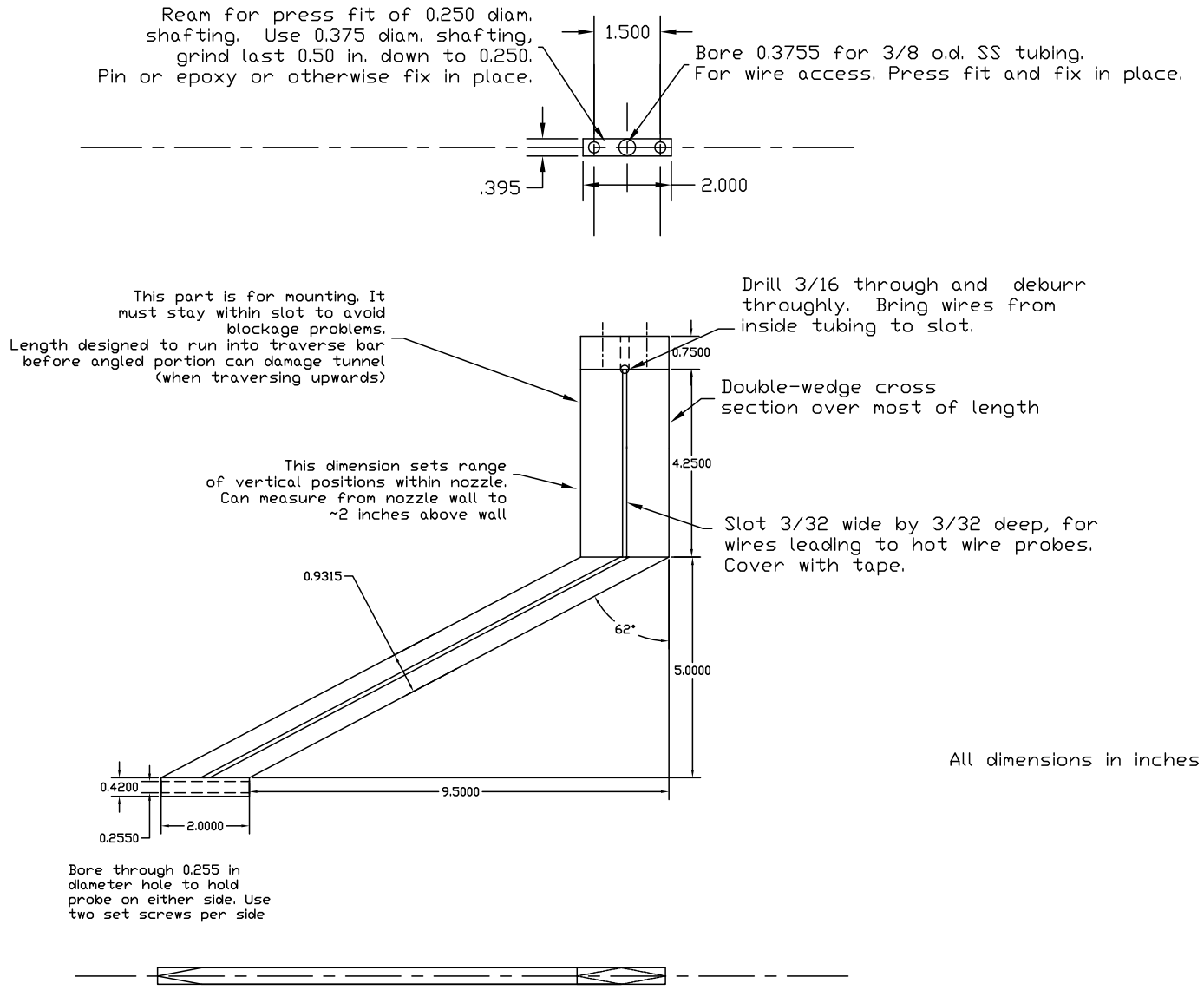

Figure C.1. Angled probe support drawing.

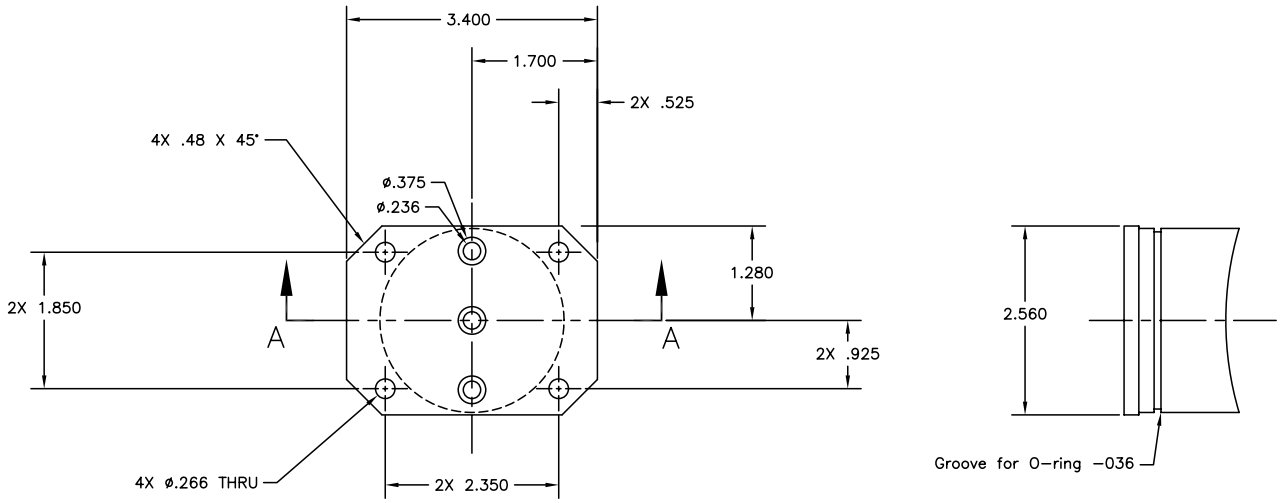

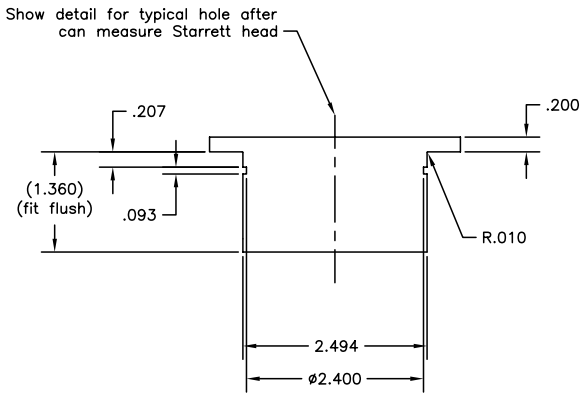

SECTION A–A

Isolated Roughness Insert for Metrolaser Small Window Insert. S.P. Schneider, Rev. 2, 10 August 2007. Half scale.
Material: 15–5PH H1100 Stainless steel. Modified from DEI drawing 922–62 and drawing for pressure–tap blank. Must fit to 3x10–in. window insert, DEI drawing 922–61, with inner surface flush to 0.001 in. or so. The 3x10 insert was built ca. 2002 and is available for fit checks.

Contour inner surface per nozzle coordinates. Radius varies with distance from left to right. See printout. Radius at window center about 4.664 in.

Notes:
1) Use Starrett micrometer head, model 263L–38TN, to form the roughness element and adjust the vertical position. Seal with o–ring around roughness element. Generates a 0.235–in–dia. roughness element. Micrometer head protrudes from the outside of the tunnel. Each 2.5–in. insert to have several holes for varying the spanwise location of the roughness element. Several inserts can provide a range of holes.

Micrometer head threaded 3/8–40, 0.375 in. o.d. Tap outer part of hole in sleeve with same size. Ream clearance on 0.235 through. O–ring between rod and clearance hole to seal. Space holes 0.500 spanwise. Holes must be perpendicular to inner radius, so hole spacing on outside is larger than hole spacing on inside, can only put 3 holes in each (see Robin's sketch of 9 Aug. 07). Maximum distance of hole from symmetry plane is 0.522 at inner diameter per Robin's computations).
2) Need plugs for each of the holes that aren't used. To clear the head in use, need to have the plugs made individually to fit, to thread into the hole and fit flush on the inside. Insert plug before final machining of i.d. contour.
3) Insert 1 has a hole on centerline, plus 0.470 above and below, 3 holes. Insert 2 has holes 0.235 above and below centerline, 2 holes. Insert 3 has holes 0.118 above, 0.353 below. Insert 4 has holes 0.353 above, 0.118 below. See if we can afford all 4 plus plugs, maybe not all in year 1. Inserts CANNOT be rotated 180 deg. to reverse, as nozzle radius expands slightly downstream. Set gives ability to vary spanwise in increments of 1/2 of roughness diameter, up to 2 diam. Make more later if necessary.

Figure C.2. Roughness insert drawing.

D. Test Conditions

Table D.1: Test conditions. Vacuum pressure at the beginning of the run is represented by p_{vac}. Smooth-wall data are denoted by the symbol "-".

Figure	Year	Month	Run	p_0 (psia)	T_0 (°C)	p_{vac} (torr)	k (in.)	Quiet/Noisy
3.7	2009	May	9	90.9	161	1.53	-	Quiet
	2009	May	10	41.0	158	1.32	-	Quiet
	2009	May	11	20.7	156	0.95	-	Quiet
4.1	2008	Feb	6	121.6	161	1.72	0.10	Noisy
	2008	Feb	16	119.4	160	2.39	0.10	Quiet
4.2	2008	Feb	19	119.9	160	2.35	0.18	Quiet
4.4	2008	Feb	3	123.1	160	1.60	0.26	Quiet
4.6	2008	Feb	20	119.6	161	2.14	0.32	Quiet
4.8	2008	Feb	17	120.1	161	1.98	0.40	Quiet
4.10	2008	Feb	2	120.4	160	2.01	0.76	Quiet
4.12	2008	Feb	17	120.1	161	1.98	0.40	Quiet
	2008	Feb	13	89.4	160	2.22	0.50	Quiet
5.5	2009	Jan	14	95.0	160	2.97	0.26	Quiet
5.6	2008	Nov	6	90.2	160	2.17	-	Quiet
5.7	2009	Jan	6	89.8	160	3.19	-	Quiet
5.8	2009	Jan	16	90.4	160	1.94	0.40	Quiet
6.1	2009	Jan	20	90.5	161	1.06	-	Quiet
6.2	2009	Jan	20	90.5	161	1.06	-	Quiet
6.3	2009	Jan	1	90.7	159	1.18	-	Quiet
	2009	Jan	2	89.7	159	2.47	-	Quiet
	2009	Jan	3	90.5	160	1.91	-	Quiet
	2009	Jan	4	90.1	160	3.03	-	Quiet
6.4	2009	Jan	20	90.5	161	1.06	-	Quiet
	2009	Jan	26	89.7	161	2.34	0.10	Quiet
	2009	Jan	21	90.0	161	3.42	0.18	Quiet
	2009	Jan	22	89.9	160	2.46	0.26	Quiet
	2009	Jan	23	89.5	160	3.71	0.30	Quiet
	2009	Jan	25	89.9	160	2.37	0.34	Quiet
	2009	Jan	24	90.1	160	2.39	0.40	Quiet
6.5	2009	Jan	1	90.7	159	1.18	-	Quiet
	2009	Jan	7	92.3	160	2.58	0.26	Quiet
	2009	Jan	9	89.9	161	2.36	0.30	Quiet
	2009	Jan	10	90.0	159	2.30	0.34	Quiet
	2009	Jan	11	89.2	160	2.60	0.40	Quiet
6.6	2009	Jan	20	90.5	161	1.06	-	Quiet
	2009	Jan	27	90.2	161	2.59	0.26	Quiet
	2009	Jan	28	90.4	161	1.31	0.40	Quiet
6.7	2009	Jan	1	90.7	159	1.18	-	Quiet
	2009	Jan	15	89.9	160	2.39	0.26	Quiet
	2009	Jan	19	89.6	162	3.12	0.30	Quiet
	2009	Jan	17	89.6	160	2.66	0.34	Quiet
	2009	Jan	16	90.4	160	1.94	0.40	Quiet
6.8	2009	Jan	20	90.5	161	1.06	-	Quiet
	2009	Jan	22	89.9	160	2.46	0.26	Quiet
	2009	Jan	24	90.1	160	2.39	0.40	Quiet
	2009	Jan	27	90.2	161	2.59	0.26	Quiet
	2009	Jan	28	90.4	161	1.31	0.40	Quiet
6.9	2009	Jan	1	90.7	159	1.18	-	Quiet
	2009	Jan	7	92.3	160	2.58	0.26	Quiet
	2009	Jan	10	90.0	159	2.30	0.34	Quiet
	2009	Jan	11	89.2	160	2.60	0.40	Quiet

Continued on next page

Figure	Year	Month	Run	p_0 (psia)	T_0 (°C)	p_{vac} (torr)	k (in.)	Quiet/Noisy
	2009	Jan	15	89.9	160	2.39	0.26	Quiet
	2009	Jan	17	89.6	160	2.66	0.34	Quiet
	2009	Jan	16	90.4	160	1.94	0.40	Quiet
6.10	2009	Jan	20	90.5	161	1.06	-	Quiet
	2009	Feb	18	90.4	161	0.80	0.40	Quiet
and	2009	Feb	19	90.4	159	2.16	0.40	Quiet
	2009	Feb	5	91.0	158	2.02	0.40	Quiet
6.11	2009	Feb	6	90.2	159	2.13	0.40	Quiet
	2009	Feb	7	90.2	159	0.96	0.40	Quiet
	2009	Feb	8	90.0	159	1.77	0.40	Quiet
	2009	Feb	9	91.3	159	3.86	0.40	Quiet
	2009	Feb	10	90.8	159	1.73	0.40	Quiet
	2009	Feb	11	89.9	159	2.24	0.40	Quiet
	2009	Feb	12	90.6	158	1.34	0.40	Quiet
7.1	2009	Jan	20	90.5	161	1.06	-	Quiet
	2009	Jan	28	90.4	161	1.31	0.40	Quiet
7.2	2009	Jan	29	90.2	161	2.21	0.40	Quiet
	2009	Jan	34	90.5	160	1.32	0.40	Quiet
7.3	2009	Jan	29	90.2	161	2.21	0.40	Quiet
	2009	Jan	34	90.5	160	1.32	0.40	Quiet
7.4	2009	Jan	20	90.5	161	1.06	-	Quiet
	2009	Jan	28	90.4	161	1.31	0.40	Quiet
7.5	2009	Feb	13	90.7	158	1.10	0.40	Quiet
	2009	Feb	14	90.6	159	1.76	0.40	Quiet
	2009	Feb	15	90.8	159	2.21	0.40	Quiet
7.6	2009	Feb	13	90.7	158	1.10	0.40	Quiet
	2009	Feb	14	90.6	159	1.76	0.40	Quiet
	2009	Feb	15	90.8	159	2.21	0.40	Quiet
7.7	2009	Feb	7	90.2	159	0.96	0.40	Quiet
	2009	Feb	8	90.0	159	1.77	0.40	Quiet
	2009	Feb	9	91.3	159	3.86	0.40	Quiet
7.8	2009	Feb	10	90.8	159	1.73	0.40	Quiet
	2009	Feb	11	89.9	159	2.24	0.40	Quiet
	2009	Feb	12	90.6	158	1.34	0.40	Quiet
7.9	2009	Feb	16	90.4	159	0.86	0.40	Quiet
	2009	Feb	17	74.9	159	1.69	0.40	Quiet
7.10	2009	Feb	16	90.4	159	0.86	0.40	Quiet
	2009	Feb	17	74.9	159	1.69	0.40	Quiet
7.11	2009	May	13	80.3	159	1.54	0.40	Quiet
7.12	2009	Feb	13	90.7	158	1.10	0.40	Quiet
	2009	Feb	14	90.6	159	1.76	0.40	Quiet
	2009	Feb	15	90.8	159	2.21	0.40	Quiet
	2009	Feb	7	90.2	159	0.96	0.40	Quiet
	2009	Feb	8	90.0	159	1.77	0.40	Quiet
	2009	Feb	9	91.3	159	3.86	0.40	Quiet
	2009	Feb	10	90.8	159	1.73	0.40	Quiet
	2009	Feb	11	89.9	159	2.24	0.40	Quiet
	2009	Feb	12	90.6	158	1.34	0.40	Quiet
7.13	2009	May	15	80.7	159	1.76	0.40	Quiet
	2009	May	12	81.0	159	1.88	0.40	Quiet
	2009	May	13	80.3	159	1.54	0.40	Quiet
	2009	May	14	79.9	159	1.27	0.40	Quiet